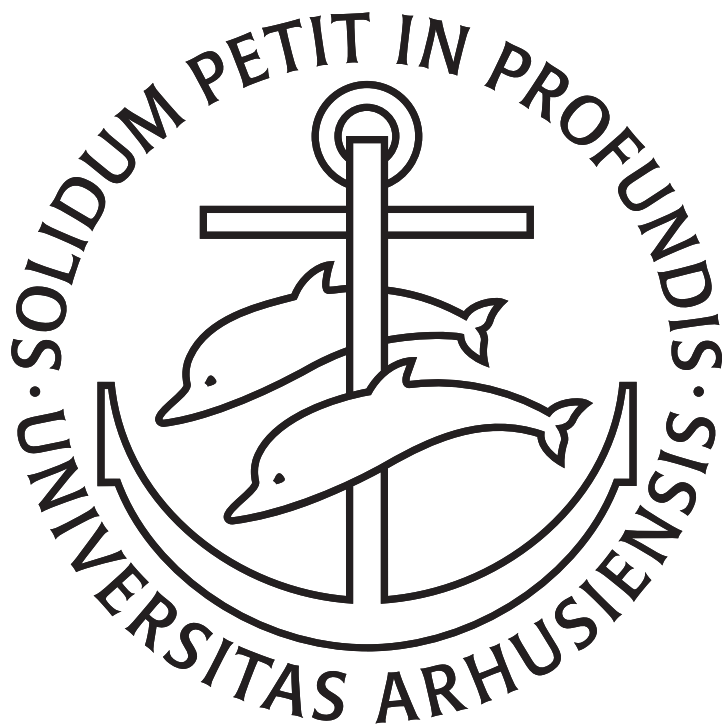


TESTS OF FUNDAMENTAL
SYMMETRIES WITH
TRAPPED ANTIHYDROGEN



PHD THESIS
CHRIS ØRUM RASMUSSEN

SUPERVISOR: JEFFREY S. HANGST

JULY 2016

DEPARTMENT OF PHYSICS AND ASTRONOMY
AARHUS UNIVERSITY

Abstract

Antihydrogen is the simplest pure antimatter atomic system, and it allows for direct tests of CPT symmetry as well as the weak equivalence principle. Furthermore the study of antihydrogen may provide clues to the matter-antimatter asymmetry observed in the universe - one of the major unanswered questions in modern physics. Since 2010, it has been possible to perform such tests on magnetically trapped antihydrogen, and this work reports on several recent studies.

Analysing the temporal and spatial distribution of annihilations as antihydrogen atoms are released from the magnetic trap, we set limits on the gravitational acceleration of antihydrogen, ruling out a gravitational mass, M_g greater than 110 times the inertial mass, M , as well as $M_g < -65M$. An improved limit on the charge neutrality of the antihydrogen atom is also presented. Stochastic electric potentials are used to empty the trap of any putatively charged antihydrogen atoms. From the lack of response to these potentials, we can set a limit for the charge of antihydrogen at $|Q| < 7.1 \times 10^{-10} e$. From this measurement, the limit on the positron charge anomaly can also be improved.

As the main focus of this work, we consider the measurement of the 1S-2S transition frequency in antihydrogen. The necessary theoretical framework for an initial measurement is developed and used to identify a feasible detection method for the excited 2S atoms. Recorded data from a series of trials is then analysed by comparison to a detailed simulation of the experiment. While the two are in excellent agreement, the data collected is not compellingly different from a pure background sample.

Resumé

Antibrint er det simpleste atomare system af ren antistof, og det tillader direkte tests af både CPT symmetri og det svage ækvivalensprincip. Ydermere kan studiet af antibrint give ledetråde til spørgsmålet om den store asymmetri vi observerer mellem stof og antistof i universet - et af de største ubesvarede spørgsmål i moderne fysik. Siden 2010 har det været muligt at studere antibrint fanget i en magnetisk fælde, og den nærværende tekst omhandler nogle af de seneste sådanne studier.

Ved at analysere de tidslige og rumlige fordelinger af annihilationer når antibrintatomer frigives fra den magnetiske fælde, sætter vi en grænse for tyngdeaccelerationen af antibrint, og kan udelukke en gravitationel masse, M_g , større end 110 gange den inertielle masse, M , og ligeledes for $M_g < -65M$. Vi præsenterer også en forbedret grænse for den elektriske ladning af antibrint. Ved at anvende stokastiske elektriske potentialer, kan vi tømme fælden for atomer med en antaget elektrisk ladning. Baseret på fraværet af en respons til disse potentialer, kan vi sætte en grænse for antibrints elektriske ladning på $|Q| < 7,1 \times 10^{-10} e$. Ud fra denne måling kan grænsen for positronens ladnings afvigelse fra elementarladningen også forbedres.

Det primære fokus i denne afhandling omhandler en måling af 1S-2S overgangsfrekvensen i antibrint. Den nødvendige teoretiske baggrund udarbejdes og bruges til at identificere en sandsynlig metode til at identificerede exciterede 2S atomer. Data fra en række af forsøg analyseres derefter gennem sammenligning med en detaljeret simulation af eksperimentet. Selvom vi finder god overensstemmelse mellem de to, er de optagne data ikke utvetydigt skelnelige fra ren baggrund.

Contents

Abstract	i
Resumé	iii
Acknowledgements	vii
List of Figures	viii
List of Tables	x
Publications	xiii
1 Antimatter	1
1.1 Motivations for Antihydrogen Research	2
1.2 Antihydrogen in the Laboratory	5
2 Experimental Setup	9
2.1 The ALPHA-2 Apparatus	9
2.2 Antihydrogen Synthesis and Confinement	14
2.3 Laser System and Metrology	16
2.4 Enhancement Cavity	21
3 Gravitational Free-fall of Antihydrogen	27
3.1 Data and Analysis	28
3.2 Future Improvements	32
4 Charge Neutrality of Antihydrogen	35
4.1 Experimental Procedure	36
4.2 Data and Analysis	36
5 Atomic Theory of Antihydrogen	43

5.1	Energy Levels of Antihydrogen	43
5.2	1S-2S Excitation	50
5.3	Shifts and Broadening Effects	56
5.4	Numerical Simulation	59
6	2S Detection Schemes	67
6.1	Lyman- α Photons	67
6.2	Spin-flip Ejection	68
6.3	Microwave Transition	69
6.4	Photo-ionisation	71
6.5	Disappearance Detection	74
7	1S-2S Spectroscopy Runs	75
7.1	Experimental Procedure	75
7.2	Data and Analysis	78
7.3	Conclusion	81
8	Conclusions and Outlook	83
A	Table of Acronyms	85
	Bibliography	87

Acknowledgements

I would like to express my thanks to the people who have generously taken the time to share with me their knowledge and wisdom. Too many people to list them all have helped me on my way, but a special mention must be given to my supervisor Prof. Jeff Hangst, Prof. Niels Madsen, Dr. Will Bertsche, Prof. Francis Robicheaux, Prof. Joel Fajans, Dr. Stefan Eriksson, and Prof. Claudio Cesar.

I am grateful to my colleagues and friends on the ALPHA experiment, with whom I have shared the long nights, the frustration, the excitement and the victories.

I would also like to acknowledge the financial support of the European Research Council (ERC).

List of Figures

1.1	A track left by a positron in the bubble chamber of Carl Anderson . . .	2
2.1	Cutaway diagram of the ALPHA apparatus showing the relative locations of the Penning trap electrodes, windings of the octupole and the outer mirror coils, as well as the annihilation detector. . .	10
2.2	Normalized transverse fields of ideal multipole magnets as functions of radius.	11
2.3	Magnetic field on axis resulting from different current configurations in the mirror coils	12
2.4	Event displays of a typical annihilation event and a typical cosmic event.	13
2.5	Nested well potential and antiproton bounce frequencies for autoresonant injection.	15
2.6	Comparison of candidate energy distributions for trapped antihydrogen atoms.	16
2.7	Simulations of antihydrogen atoms as well as bare antiprotons escaping from the trap with comparison to data.	17
2.8	Frequency shifts needed for addressing both the c-c and d-d transitions.	19
2.9	Schematic of the laser and frequency metrology and control system.	21
2.10	Measured laser frequencies and Allan deviation	22
2.11	Support structures for the US and DS internal cavity mirrors, respectively	23
2.12	Diagram of internal enhancement cavity mirrors	24
2.13	Downstream external cavity mirror assembly.	26

3.1	Time and vertical (y) position of the measured antihydrogen atoms as well as of a sample of 10,000 simulated atoms with $F = 100$. . .	29
3.2	Reverse, cumulative averages of the annihilation positions for the measured antihydrogen compared with simulations of different gravitational to inertial mass ratios, F	31
3.3	P-value as a function of simulated F assuming different systematics	33
3.4	Reverse, cumulative averages for simulated antihydrogen atoms with $F = -1, 0, 1$, cooled to different temperatures	34
4.1	Applied electric potential at various radii as a function of z	37
4.2	Time history of applied stochastic potentials as measured on the electrodes	38
4.3	Simulated survival probability s of charged atoms in applied stochastic fields	41
5.1	The Breit-Rabi diagram for the 1S states in (anti)hydrogen	45
5.2	Fine structure of the $n = 2$ manifold	47
5.3	Ratio of spin-flip-inducing single photon 2S as function of the magnetic field	50
5.4	Single pass excitation probabilities for the perturbative as well as the non-perturbative calculation	55
5.5	Fractional populations in the simulated end states as a function of the total illumination time	62
5.6	Fractional populations as functions the laser detuning using a flattened magnetic field	64
5.7	Fractional populations as functions the laser detuning using a bucked magnetic field	65
5.8	Fraction of atoms remaining trapped after the full illumination time in different magnetic fields	66
6.1	Microwave transition rates out of the low field seeking 2S states, calculated for two different frequencies as functions of magnetic field.	70
6.2	Ionisation positions in z and r compared to the region detectable by the MCP assembly in its current setup.	72
7.1	Simulated lineshapes in different detection channels for the parameters used in spectroscopy runs of 2015	79

List of Tables

2.1	Comparison of cavity parameters for the internal and external cavity designs	25
3.1	Trap depth and potential energies for free-falling atoms	28
4.1	Recorded events in the stochastic and null trials.	40
5.1	Representative laser parameters in 1S-2S spectroscopic measurements in hydrogen.	56
5.2	Broadening effects and shifts for the 1S-2S excitation	60
7.1	Expected and observed counts in the disappearance mode of detection	80
7.2	Expected and observed counts in the appearance mode of detection	81

Notation and Units

The equations in this work are generally kept in accord with the international system of units (SI), although some scalings of SI units are used (like cm and kHz) when convenient. It has become customary in atom trapping to denote the energy of trapped atoms in units of Kelvin (K). This should always be interpreted as Boltzmann's constant (k_B) times the number given in Kelvins. Listed below are some natural constants used throughout as well as typical usages of symbols.

Natural Constants

Speed of light in vacuum	$c = 299\,792\,458$ m/s (exact)
Vacuum permeability	$\mu_0 = 4\pi \times 10^{-7}$ (exact)
Vacuum permittivity	$\epsilon_0 = (\mu_0 c^2)^{-1}$ (exact)
Planck's constant	$h = 6.626\,070\,040(81) \times 10^{-34}$ Js
Planck's reduced constant	$\hbar = \frac{h}{2\pi}$
Bohr radius	$a_0 = 0.529\,177\,210\,67(12) \times 10^{-10}$ m
Boltzmann constant	$k_B = 1.380\,648\,52(79) \times 10^{-23}$ J/K
Elementary charge	$e = 1.602\,176\,6208(98) \times 10^{-19}$ C

Symbols

Quantity	Symbol	Unit
Electric field	E	V/m
Magnetic field	B	T
Energy	\mathcal{E}	J
Intensity	I	W/m ²
Angular frequency	Ω, ω	Rad/s
Frequency	f	Hz
Rate (usually decay rate)	Γ	s ⁻¹

Publications

- M. Ahmadi, M. Baquero-Ruiz, W. Bertsche, E. Butler, A. Capra, C. Carruth, C. L. Cesar, M. Charlton, A. E. Charman, S. Eriksson, L. T. Evans, N. Evetts, J. Fajans, T. Friesen, M. C. Fujiwara, D. R. Gill, A. Gutierrez, J. S. Hangst, W. N. Hardy, M. E. Hayden, C. A. Isaac, A. Ishida, S. A. Jones, S. Jonsell, L. Kurchaninov, N. Madsen, D. Maxwell, J. T. K. McKenna, S. Menary, J. M. Michan, T. Momose, J. J. Munich, P. Nolan, K. Olchanski, A. Olin, A. Povilus, P. Pusa, **C. Ø. Rasmussen**, F. Robicheaux, R. L. Sacramento, M. Sameed, E. Sarid, D. M. Silveira, C. So, T. D. Tharp, R. I. Thompson, D. P. van der Werf, J. S. Wurtele, and A. I. Zhmoginov. “An improved limit on the charge of antihydrogen from stochastic acceleration”. *Nature*, 529(7586):373–376, 01 2016.
- C. Amole, G. B. Andresen, M. D. Ashkezari, M. Baquero-Ruiz, W. Bertsche, C. Burrows, E. Butler, A. Capra, C. L. Cesar, S. Chapman, M. Charlton, A. Deller, S. Eriksson, J. Fajans, T. Friesen, M. C. Fujiwara, D. R. Gill, A. Gutierrez, J. S. Hangst, W. N. Hardy, M. E. Hayden, A. J. Humphries, C. A. Isaac, S. Jonsell, L. Kurchaninov, A. Little, N. Madsen, J. T. K. McKenna, S. Menary, S. C. Napoli, P. Nolan, K. Olchanski, A. Olin, A. Povilus, P. Pusa, **C. Ø. Rasmussen**, F. Robicheaux, R. L. Sacramento, S. Stracka, J. A. Sampson, E. Sarid, D. Seddon, D. M. Silveira, C. So, R. I. Thompson, T. Tharp, J. Thornhill, M. P. Tooley, D. P. van der Werf, and D. Wells. “Silicon vertex detector upgrade in the ALPHA experiment”. *Nuclear Instruments and Methods in Physics Research Section A: Accelerators, Spectrometers, Detectors and Associated Equipment*, 732(0):134 – 136, 2013. Vienna Conference on Instrumentation 2013.
- C. Amole, M. D. Ashkezari, M. Baquero-Ruiz, W. Bertsche, P. D. Bowe, E. Butler, A. Capra, C. L. Cesar, M. Charlton, A. Deller, A. Deller, E. Donnan P. H., Eriksson, J. Fajans, T. Friesen, M. C. Fujiwara, D. R. Gill, A. Gutierrez, J. S.

- Hangst, W. N. Hardy, M. E. Hayden, A. J. Humphries, C. A. Isaac, S. Jonsell, L. Kurchaninov, A. Little, N. Madsen, J. T. K. McKenna, S. Menary, S. C. Napoli, P. Nolan, K. Olchanski, A. Olin, P. Pusa, **C. Ø. Rasmussen**, F. Robicheaux, E. Sarid, C. R. Shields, D. M. Silveira, S. Stracka, C. So, I. Thompson, D. P. van der Werf, and J.S. Wurtele. “Resonant quantum transitions in trapped antihydrogen atoms”. *Nature*, 483(7390):439–443, 2012.
- C. Amole, M. D. Ashkezari, M. Baquero-Ruiz, W. Bertsche, E. Butler, A. Capra, C. L. Cesar, S. Chapman, M. Charlton, S. Eriksson, J. Fajans, T. Friesen, M. C. Fujiwara, D. R. Gill, A. Gutierrez, J. S. Hangst, W. N. Hardy, M. E. Hayden, C. A. Isaac, S. Jonsell, L. Kurchaninov, A. Little, N. Madsen, J. T. K. McKenna, S. Menary, S. C. Napoli, P. Nolan, K. Olchanski, A. Olin, A. Povilus, P. Pusa, **C. Ø. Rasmussen**, F. Robicheaux, E. Sarid, D. M. Silveira, S. Stracka, C. So, R. I. Thompson, M. Turner, D. P. van der Werf, J. S. Wurtele, A. Zhmoginov, and ALPHA Collaboration. “Autoresonant-spectrometric determination of the residual gas composition in the ALPHA experiment apparatus”. *Review of Scientific Instruments*, 84(6):–, 2013.
 - C. Amole, M. D. Ashkezari, M. Baquero-Ruiz, W. Bertsche, E. Butler, A. Capra, C. L. Cesar, M. Charlton, A. Deller, S. Eriksson, J. Fajans, T. Friesen, M. C. Fujiwara, D. R. Gill, A. Gutierrez, J. S. Hangst, W. N. Hardy, M. E. Hayden, C. A. Isaac, S. Jonsell, L. Kurchaninov, A. Little, N. Madsen, J. T. K. McKenna, S. Menary, S. C. Napoli, K. Olchanski, A. Olin, P. Pusa, **C. Ø. Rasmussen**, F. Robicheaux, E. Sarid, C. R. Shields, D. M. Silveira, C. So, S. Stracka, R. I. Thompson, D. P. van der Werf, J. S. Wurtele, A. Zhmoginov, (ALPHA collaboration), and L. Friedland. “Experimental and computational study of the injection of antiprotons into a positron plasma for antihydrogen production”. *Physics of Plasmas (1994-present)*, 20(4):–, 2013.
 - C. Amole, M. D. Ashkezari, M. Baquero-Ruiz, W. Bertsche, E. Butler, A. Capra, C. L. Cesar, M. Charlton, A. Deller, N. Evetts, S. Eriksson, J. Fajans, T. Friesen, M. C. Fujiwara, D. R. Gill, A. Gutierrez, J. S. Hangst, W. N. Hardy, M. E. Hayden, C. A. Isaac, S. Jonsell, L. Kurchaninov, A. Little, N. Madsen, J. T. K. McKenna, S. Menary, S. C. Napoli, K. Olchanski, A. Olin, P. Pusa, **C. Ø. Rasmussen**, F. Robicheaux, E. Sarid, D. M. Silveira, C. So, S. Stracka, T. Tharp, R. I. Thompson, D. P. van der Werf, and J. S. Wurtele. “In situ electromagnetic field diagnostics with an electron plasma in a Penning-Malmberg trap”. *New Journal of Physics*, 16(1):013037, 2014.

- C. Amole, M. D. Ashkezari, M. Baquero-Ruiz, W. Bertsche, E. Butler, A. Capra, C. L. Cesar, M. Charlton, S. Eriksson, J. Fajans, T. Friesen, M. C. Fujiwara, D. R. Gill, A. Gutierrez, J. S. Hangst, W. N. Hardy, M. E. Hayden, C. A. Isaac, S. Jonsell, L. Kurchaninov, A. Little, N. Madsen, J. T. K. McKenna, S. Menary, S. C. Napoli, P. Nolan, A. Olin, P. Pusa, **C. Ø. Rasmussen**, F. Robicheaux, E. Sarid, D. M. Silveira, C. So, R. I. Thompson, D. P. van der Werf, J. S. Wurtele, A. Zhmoginov, and A. E. Charman. “Description and first application of a new technique to measure the gravitational mass of antihydrogen”. *Nat Commun*, 4:1785, Apr 2013. Article.
- C. Amole, M. D. Ashkezari, M. Baquero-Ruiz, W. Bertsche, E. Butler, A. Capra, C. L. Cesar, M. Charlton, S. Eriksson, J. Fajans, T. Friesen, M. C. Fujiwara, D. R. Gill, A. Gutierrez, J. S. Hangst, W. N. Hardy, M. E. Hayden, C. A. Isaac, S. Jonsell, L. Kurchaninov, A. Little, N. Madsen, J. T. K. McKenna, S. Menary, S. C. Napoli, P. Nolan, K. Olchanski, A. Olin, A. Povilus, P. Pusa, **C. Ø. Rasmussen**, F. Robicheaux, E. Sarid, D. M. Silveira, C. So, T. D. Tharp, R. I. Thompson, D. P. van der Werf, Z. Vendeiro, J. S. Wurtele, A. I. Zhmoginov, and A. E. Charman. “An experimental limit on the charge of antihydrogen”. *Nat Commun*, 5, 06 2014.
- G. B. Andresen, M. D. Ashkezari, M. Baquero-Ruiz, W. Bertsche, P. D. Bowe, E. Butler, C. L. Cesar, M. Charlton, A. Deller, S. Eriksson, J. Fajans, T. Friesen, M. C. Fujiwara, D. R. Gill, A. Gutierrez, J. S. Hangst, W. N. Hardy, R. S. Hayano, M. E. Hayden, A. J. Humphries, R. Hydromako, S. Jonsell, S. L. Kemp, L. Kurchaninov, N. Madsen, S. Menary, P. Nolan, K. Olchanski, A. Olin, P. Pusa, **C. Ø. Rasmussen**, F. Robicheaux, E. Sarid, D. M. Silveira, C. So, J. W. Storey, R. I. Thompson, D. P. van der Werf, J. S. Wurtele, and Y. Yamazaki. “Confinement of antihydrogen for 1,000 seconds”. *Nat Phys*, 7:558–564, Jul 2011. 10.1038/nphys2025.
- E. Butler, G. B. Andresen, M. D. Ashkezari, M. Baquero-Ruiz, W. Bertsche, P. D. Bowe, C. L. Cesar, S. Chapman, M. Charlton, A. Deller, S. Eriksson, J. Fajans, T. Friesen, M. C. Fujiwara, D. R. Gill, A. Gutierrez, J. S. Hangst, W. N. Hardy, M. E. Hayden, A. J. Humphries, R. Hydromako, M. J. Jenkins, S. Jonsell, L. V. Jørgensen, S. L. Kemp, L. Kurchaninov, N. Madsen, S. Menary, P. Nolan, K. Olchanski, A. Olin, A. Povilus, P. Pusa, **C. Ø. Rasmussen**, F. Robicheaux, E. Sarid, S. Seif el Nasr, D. M. Silveira, C. So, J. W. Storey, R. I.

Thompson, D. P. Werf, J. S. Wurtele, and Y. Yamazaki. "Trapped antihydrogen". *Hyperfine Interactions*, 212(1-3):15–29, 2012.

- N. Madsen, C. Ø. Rasmussen, and F. Robicheaux. "Aspects of 1S-2S spectroscopy of single trapped antihydrogen atoms". In preparation.

Outline

Chapter 1 gives an overview of the motivations for investigating antimatter and summarizes the experimental progress in studying the antihydrogen atom in particular. Chapter 2 describes the experimental apparatus and sums up the key upgrades made recently in the transition from the original ALPHA machine to ALPHA-2. The spectroscopic laser system for 1S-2S excitation is also described in this chapter, although the following chapters concern themselves with other measurements.

In Chapter 3, a technique for measuring the gravitational free-fall of antihydrogen is described and the first application of this technique in the form of a retrospective analysis of recorded annihilation locations and times in ALPHA is presented. In Chapter 4 we turn to the first new measurement to come out of the upgraded ALPHA-2 apparatus, which uses stochastic acceleration to improve the experimental limit on the charge neutrality of antihydrogen. From this measurement and the assumption of charge superposition, an improved limit on the positron charge anomaly is also deduced.

Chapter 5 returns to the subject of 1S-2S spectroscopy and considers the atomic theory needed to describe such an experiment in antihydrogen, including both the excitation dynamics in the magnetic minimum trap of ALPHA as well as de-excitation effects which limit the lifetime of the excited 2S state in the trap. Chapter 6 discusses schemes for detecting successful excitations in a 1S-2S experiment in the specific context making such a detection feasible with only single atoms trapped at a time in an apparatus like ALPHA-2. Finally, Chapter 7 reports on a series of 1S-2S spectroscopic trials conducted in late 2015 and searches for evidence that the transition was driven.

Personal Contribution

Most aspects of the ALPHA experiment are subject to wide collaboration and I have been involved at least to some degree with nearly all of them. I have been involved with the ALPHA-2 machine from the design phase, through construction, commissioning, and the production of new results. Areas in which I have contributed more heavily are in the installation and commissioning of the laser and frequency control system for the 1S-2S experiments, as well as of the enhancement cavity, described in Chapter 2. I have done most of the calculations in Chapter 5, with one notable exception being the derivation of the 1S- and 2S- coefficients, (5.21) and (5.22). While most of the simulation code described in Section 5.4 is written by Prof. Francis Robicheaux, I have maintained and expanded on this code as well as compiled all the results presented here.

On many occasions in this work, I use the narrating "we", rather than an "I", underlining that in particular the experimental results are a collaborative effort, which cannot be claimed by any single person, but to which I am proud to have contributed.

Chapter 1

Antimatter

For every type of particle in nature, there exists a corresponding antiparticle, which has a lifetime and mass equal to its matter counterpart and equal magnitude, but opposite sign, of electric charge and spin. The antiparticle of the electron is the positively charged positron, for the proton there is the negative antiproton, and so on. A select few particles, including the photon, are their own antiparticle. A particle and its antiparticle partner have the distinctive property that they can annihilate upon colliding, and thereby release an amount of energy described by Einstein's famous equation:

$$\mathcal{E} = mc^2$$

It is traditional to denote antiparticles with either a bar over the letter describing the matter particle or by reversing the sign indicating the charge. For example, we use \bar{p} for an antiproton and e^+ for the positron.

Antimatter was first predicted by Paul Dirac, who in 1931 postulated the existence of an "antielectron" [1]. As he was developing his relativistic equation of motion for the electron (now known as the Dirac equation), he found that aside from the two solutions with positive energy, corresponding to the two spin states of the electron, the equation had two solutions of negative energy. Dirac interpreted these solutions to imply the existence of a partner particle to the electron with equal mass but opposite charge.

This prediction was confirmed in 1932 when Carl Anderson discovered the positron [2]. Anderson was using a bubble chamber to study cosmic particles, and had a clever way of distinguishing the charges of the particles he saw. From just the curved track of a charged particle moving in a mag-

netic field, one cannot tell whether the track was produced by a negatively charged particle moving in one direction or by a positively charged particle moving in the opposite direction. By placing a sheet of lead in the middle of the bubble chamber, however, particles moving through the lead would lose energy and display a smaller radius of curvature after passing the lead. Thus the direction and thereby the charge of the particle could be inferred.

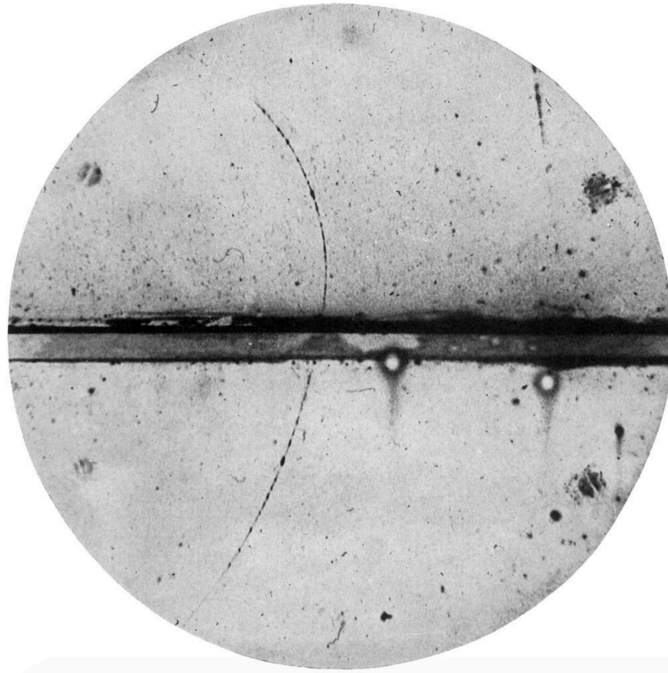


Figure 1.1: A track left by a positron passing from the bottom of the picture, through the lead sheet in the center and through to the top in Anderson's bubble chamber. Picture from [2].

1.1 Motivations for Antihydrogen Research

The study of antimatter is of great interest due to sensitivity of comparisons to ordinary matter to fundamental symmetries, allowing the experimental testing of what is often simply assumed in physical theories. Antihydrogen, the bound state of a positron and an antiproton, is a particularly attractive platform for these tests, as it is the antimatter counterpart of one of the most well studied physical systems. It is also the simplest pure antimatter

atomic system, and the only such antiatom that it has yet been possible to create in the laboratory.

CPT Symmetry

According to our current (and past) theories of antimatter, it should obey all the same physical theories that apply to ordinary matter. This perhaps somewhat vague statement can be made more formally in terms of symmetries, and in modern physics it equates to the validity of CPT symmetry. CPT is the combination of Charge conjugation (C), which is the changing of the sign of all internal quantum numbers of the particles, often simplistically referred to as the exchange of all particles with their antiparticles, Parity inversion (P), which is the changing of the sign on all spatial coordinates, i.e. a reflection of space about the origin, and Time reversal (T), letting time run backwards.

A process or a theory is then said to conserve CPT symmetry if the laws governing the process stay unchanged under the simultaneous application of these three (C, P and T) operations.

It was originally thought that each of the C, P and T symmetries were conserved by all physical processes, and indeed all of classical mechanics and Maxwell's laws do conserve each of these symmetries individually. However, in 1956, Wu and coworkers discovered by studying the beta decays of polarized ^{60}Co , that the weak force breaks both the C and the P symmetry [3]. These beta decays did not break the combined CP symmetry though, and it was thought for a while that CP symmetry is universally conserved. Once again, though, nature did not oblige, and the weak force was found to also break CP symmetry, initially only in decays of kaons [4], but later also in B mesons [5].

In order to symmetrize even these CP violating decays, Time reversal can be added, and no physical process has yet been observed to break CPT symmetry. Furthermore, it has been proven [6], that any Lorentz invariant, local, quantum field theory which has a Hermitian Hamiltonian - conditions which are often taken axiomatically - conserves CPT symmetry. Aside from requiring the mass, lifetime, magnitude of charge and so on to be identical for particles and their antiparticles, CPT symmetry also requires bound systems of

antiparticles to have identical internal energy states to their matter counterparts. It is this prediction that many of the experiments at the AD aim to test with high precision.

Baryon Asymmetry

One of the big outstanding questions in modern physics concerns the apparent absence of antimatter in the universe. According to our supposed knowledge of the physical processes that governed the creating of matter and antimatter in the early universe, the two should have been produced in equal amounts. As the universe evolved, we would then expect either the annihilation of both matter and antimatter, leaving no particles to form stars and planets, or perhaps the separation of the two into large bubbles that are either matter- or antimatter- dominated.

Both of these are contrary to observations, which indicate an entirely matter dominated universe. Mechanisms for generating such an asymmetry in the overall baryon number of the universe, which involve the non-conservation of CP symmetry as discussed above, do exist. However, the amount of this CP symmetry violation observed in experiments is far from large enough to explain the universe we have ended up with. Another solution for solving this problem is through some as-yet undiscovered asymmetry between the properties of matter and antimatter, in which case the careful study of antimatter is an obvious way forward.

Antimatter Gravity

In accordance with general relativity, the weak equivalence principle states, that the gravitational acceleration of a body is independent of its composition. One consequence of this is that objects with different masses fall with the same acceleration, as was neatly demonstrated by Commander David Scott in the absence of air resistance on the moon. The weak equivalence principle in theory extends to antimatter, but no direct experimental test has been performed.

Two of the experiments at the AD [7, 8] aim to perform such a direct measurement of the gravitational acceleration of antihydrogen at a precision of about 1%, with rather different methods for achieving this. We will return in Chapter 3 to present a measurement in ALPHA of the gravitational acceleration of antihydrogen atoms as they are released from our magnetic

trap, which however does not with the existing data come close to the above precision.

1S-2S Spectroscopy

As already mentioned, the hydrogen atom is one of the accurately measured and well-understood physical systems. The 1S-2S transition in particular has been measured to the impressive precision of around 4 parts in 10^{15} [9]. The accurate measurement of this transition in hydrogen is important because of its sensitivity to the proton charge radius and the Lamb shift, and is one of the main measurements against which Quantum ElectroDynamics (QED) has been tested. Our interest in the present context is of course in the comparison to antihydrogen and the thereby obtained precise test of CPT invariance.

There are theoretical models which introduce explicit and parameterized breaking of CPT symmetry in quantum field theory [10]. The amount of CPT symmetry breaking in these models is constrained by existing measurements that are sensitive to this symmetry in various ways, and the models can therefore be used to set limits on how different the atomic spectra of hydrogen and antihydrogen can be. Currently, the limits on the 1S-2S transition frequency found in this way are significantly below even the small uncertainty reached in the hydrogen measurement, however this is of course a model dependent limit, which investigates a particular set of ways in which to break CPT symmetry.

The aim of comparing the 1S-2S transition frequency in antihydrogen to that of hydrogen has been one of the main driving forces in the field of antihydrogen research since before the first such atoms had been created [11], and the field is now mature for its realisation.

1.2 Antihydrogen in the Laboratory

Antihydrogen was first created at relativistic kinetic energies at the Low Energy Antiproton Ring (LEAR) at CERN [12]. By passing the beam of antiprotons, circulating in the storage ring, through a (xenon) gas target, electron-positron pair formation would occur in interactions between the antipro-

tons and the xenon nuclei. On rare occasions, the positron produced would emerge velocity matched and bound to the antiproton. The low rate of production and high kinetic energy ($\beta \approx 0.9$) made the antihydrogen atoms produced in this way hard to study.

A crucial step in creating antihydrogen at low energies turned out to be the confinement of antiprotons in Penning traps. This work was pioneered by Gabrielse and coworkers, also at the LEAR facility [13].

With the reconfiguration of the antiproton facility at CERN, and the commissioning of the Antiproton Decelerator [14] (AD) in 1999, the efforts to create and study cold antihydrogen were accelerated greatly. In 2002, antihydrogen was first created from cold plasmas of positrons and antiprotons by the ATHENA collaboration [15] and by the ATRAP collaboration [16]. While valuable lessons were learned about the formation processes of antihydrogen under these circumstances, the atoms produced either annihilated or were ionised by electric fields on a time scale too short for spectroscopic measurements aimed for by both collaborations.

Confining antihydrogen in a magnetic minimum trap was first achieved in 2010 by ALPHA [17], a feat also reported by ATRAP in 2011 [18]. This opened the door for a series of first measurements on the antihydrogen atom, with the first resonantly drive quantum transitions performed already in 2011 [19].

Progress is also being made on antihydrogen experiments that do not rely on confining the $\bar{\text{H}}$. In 2013, the ASACUSA collaboration successfully sent a beam of spin-polarized antihydrogen atoms into a region with very little residual magnetic field [20]. The atoms are pushed out of the production region and focused by the magnetic field gradients in a so-called cusp trap, and the aim of this effort is to enable in-flight measurements of transitions that are heavily shifted by the magnetic field and therefore ill-suited for measurements in a magnetic trap. In particular the ground state hyperfine transition, which has been measured to a precision of a few parts in 10^{13} in hydrogen [21], is suited for this type of measurement.

A slightly differently produced beam of antihydrogen is proposed by the AEGIS collaboration to measure the deflection of the atoms in Earth's gravitational field [7]. Also intending to measure the gravitational acceleration of anti-

hydrogen, the GBAR experiment [8] has been approved to join the existing experiments at the AD, and is about to start construction of the experiment at CERN. The goal is to produce a positive antihydrogen ion, $\bar{\text{H}}^+$, which can be sympathetically cooled in a Paul trap to reach low enough energies that the gravitational acceleration dominates the motion upon release from the trap. They are also interested in in-flight spectroscopic measurements on the fast moving antihydrogen atoms that are part of the scheme for loading the Paul trap [22].

While this brief overview focused on the progress made towards experiments on antihydrogen in particular, the availability of slow antiprotons at the AD has facilitated many other interesting antimatter experiments. Of particular note are the precise spectroscopic measurements of antiprotonic helium by the ASACUSA collaboration [23] and recent improvements by the BASE experiment in the comparison of the proton and antiproton charge-to-mass ratios [24]. A more comprehensive review of physics taking place at the AD facility can be found in [25].

Chapter 2

Experimental Setup

2.1 The ALPHA-2 Apparatus

ALPHA-2 is built to produce, trap, and interrogate antihydrogen. It is the successor to the ALPHA machine, which has been described thoroughly in the literature [26], and which saw the first trapped antihydrogen and measured the first resonantly driven quantum transitions [17, 19]. ALPHA-2 preserves many of the successful design elements that made these landmarks possible: it consists of a central Penning-Malmberg trap, which performs all the charged particle manipulations necessary for forming cold antihydrogen. Superimposed on the antihydrogen production region is a magnetic minimum trap to confine the neutral antihydrogen atoms produced. Surrounding both of these is a silicon vertex detector, which detects annihilation products from the antiprotons and reconstructs the time and position of annihilating antiprotons. The arrangement of these key components is illustrated in Figure 2.1

Magnetic minimum trap

Like the original ALPHA apparatus, the confinement of neutral atoms is provided by a particular variation on the Ioffe-Pritchard trap, which uses an octupole magnet for the radial confinement, instead of a quadrupole. The choice of an octupole is made to reduce the perturbative effect of the radial magnetic fields on the non-neutral plasmas in the Penning-Malmberg trap: The field inside an infinite cylindrical multipole magnet increases as r^{s-1} ,

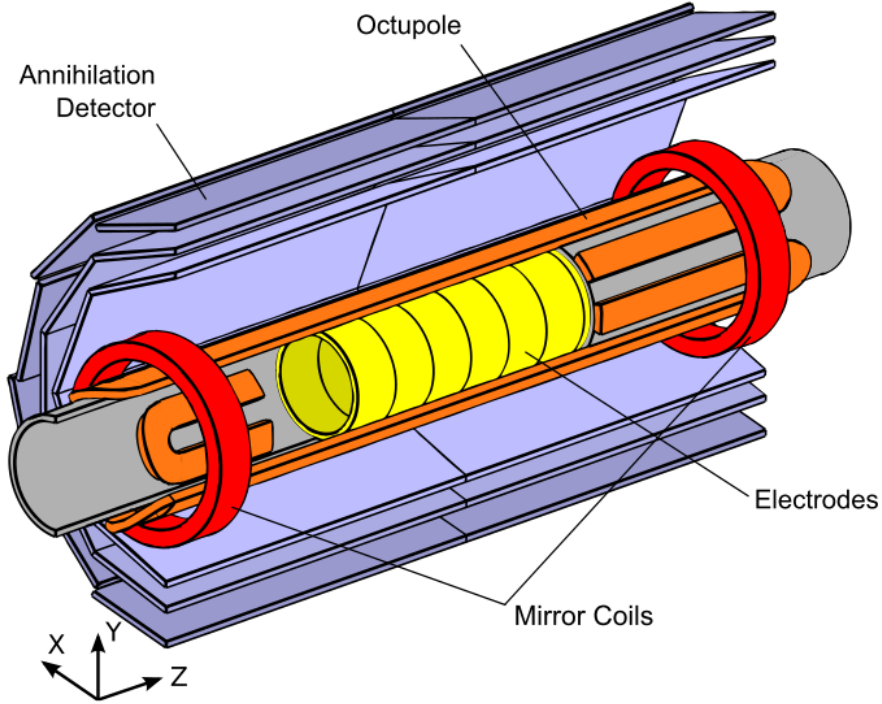


Figure 2.1: Cutaway diagram of the ALPHA apparatus showing the relative locations of the Penning trap electrodes, windings of the octupole and the outer mirror coils, as well as the annihilation detector. An external solenoid (not shown) surrounds all of the illustrated parts. The components are not drawn to scale.

where s is the multipole order, and r is the distance from the symmetry axis, so $s = 2$ for a quadrupole, $s = 3$ for a sextupole and so on. Thus, the higher order multipole, the smaller the field close to the axis is, given equal maximum field strengths. The trade-off for this benefit is in added complexity in manufacturing and difficulty in achieving a large magnetic well depth [27].

The depth of the magnetic trap is directly proportional to the difference in absolute magnetic field strength between the center of the trap and radius of the wall, r_W where the \bar{H} can annihilate. Since the fields generated by the octupole magnet is almost entirely in the radial direction at the wall radius, and thus perpendicular to the solenoidal field of the Penning trap, this magnetic field difference can be written as:

$$\Delta B = \sqrt{B_{\text{oct}}(r_W)^2 + B_z^2} - B_z \quad (2.1)$$

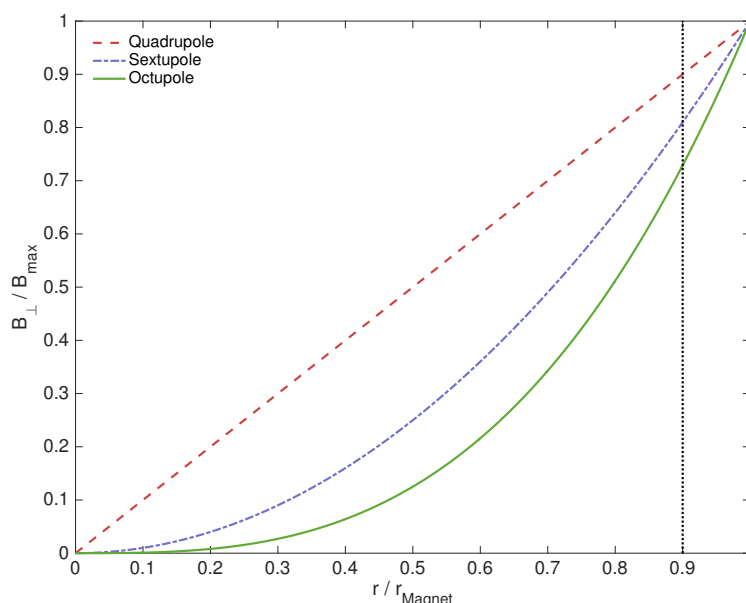


Figure 2.2: Normalized transverse fields of ideal multipole magnets as functions of radius. The dotted vertical line illustrates why a higher order multipole leads to a smaller well depth.

, where B_z is the field from the external solenoid. Note that for a given strength of octupole magnet, the well depth decreases as B_z is increased. On the other hand lowering B_z decreases the cyclotron cooling rate of plasmas in the Penning trap, making the cold plasmas needed for antihydrogen production more difficult to achieve. In ALPHA, internal booster solenoids are used to temporarily increase the axial field to 3 T and provide strong cyclotron cooling for positron- and electron- plasmas, before being turned off for the production and trapping of antihydrogen, which happens at $B_z \approx 1$ T.

In the traditional Ioffe-Pritchard trap, the axial confinement is provided by two short solenoidal windings or "mirror coils" at each end of the multipole magnet. ALPHA-2 is built with a total of 5 such mirror coils, evenly distributed along the length of the octupole magnet. This provides us with flexibility in what the shape of the produced magnetic minimum is: The magnetic field of our original machine can be reproduced simply by only energizing the outermost mirror coils. As will be pointed out in chapter 5 though, it is desirable for spectroscopic experiments to make the central region of the trap as uniform as possible. Figure 2.3 on the following page shows how the

5 mirror coils can be used to make the central trapping region much more uniform than in the original ALPHA case.

Flattening the magnetic field is not the only reason to want to customize the trapping field shape. As can be seen from either Figure 2.3 or Equation (2.1), the central mirror coils can also be used to increase the well depth of the neutral atom trap, by essentially subtracting from the background 1T field. One special usage case for the additional mirror coils is producing the field labeled "Bucked". In this case, neutral atoms are confined between mirror coils A and D, while the final mirror coil (E) is used to completely cancel the background solenoidal field. This serves the function of driving the field lines into the wall underneath mirror coil E. Thus, charged particles that are pushed towards this field-cancelling coil from within the magnetic minimum trap, will be guided into the wall. In Chapter 6 on page 67 we will describe how this can be a useful configuration for measuring 1S-2S excitations.

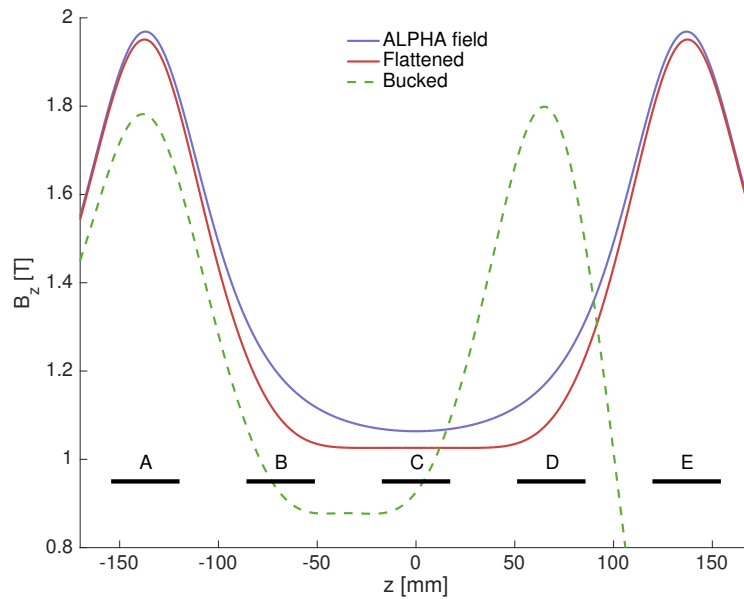


Figure 2.3: Magnetic field on axis resulting from different current configurations in the mirror coils. Positions of the mirror coil windings along the axis are indicated in black along with their identifying letter. The fields from the mirror coils add to the constant 1T background field of the external solenoid.

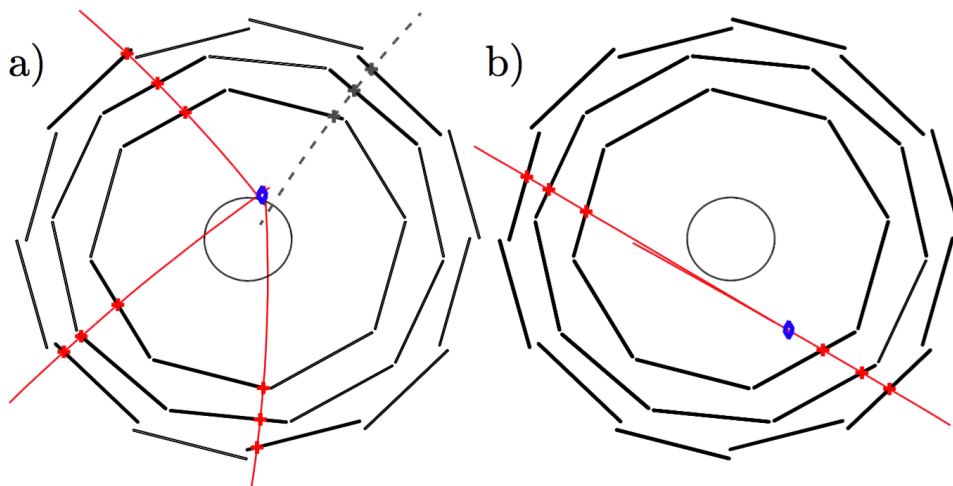


Figure 2.4: End-on event display of a) an event passing all our selection criteria for annihilation events. b) an event failing the selection criteria. The crosses represent the hits in the detector, from which the tracks are reconstructed. The red lines are tracks used to determine the location of the vertex (blue diamond) while the gray dashed line is an example of a track which was excluded by the vertex reconstruction algorithm. The central circle in the center marks the location of the surface that antihydrogen atoms annihilate on when released from the trap. Reproduced from [28].

Silicon Vertex Detector

An antiproton annihilating on a solid matter target like the inside wall of our vacuum chamber can result in a number of different annihilation products. The overwhelming majority of such annihilations include several charged pions, which can be detected and have their trajectories reconstructed by the Silicon vertex detector in ALPHA. The detector in its current form consists of 72 double-sided silicon microstrip modules arranged into 3 layers, surrounding the magnetic minimum trap. Unlike the impression that Figure 2.1 might give, the detector extends some distance beyond the outer mirror coils in order to provide a good solid angle coverage throughout the magnetic trap. A software algorithm reconstructs tracks from hits in each layer of the detector and in the case of an intersection between two or more of these tracks within the detector, a vertex is reported which estimates the position and time of an antiproton annihilation.

The main background of events not stemming from antiproton annihilations

originate from cosmic particles. A typical example of a cosmic particle event is in panel b) of Figure 2.4 on the preceding page. This is likely a single high rigidity muon, traversing the detector with little deflection in the 1T field. It been has reconstructed with two approximately collinear tracks and a vertex somewhere along this line. Events like this are distinguished from typical annihilation events like that in panel a) of Figure 2.4 by their different topologies: Using variables like track multiplicity, track rigidity, vertex location, opening angles between tracks, cosmic events are strongly suppressed. In our typical operation, around 99.5% of cosmic events are rejected, leaving a rate of cosmic events misinterpreted as antiproton annihilations of 47 ± 2 mHz. This algorithm, which is a simple set of cuts on the above mentioned variables, maintains an efficiency for detecting a single antiproton annihilation of around 60% [28].

Of course the algorithm for rejecting cosmic events can be tuned and optimized for different purposes. In [19], we look for annihilations in a much longer time window than we are usually concerned with, and therefore want to suppress cosmic events more aggressively. This was achieved with a MultiVariate Analysis (MVA), considering even more variables than the above mentioned. With this, the rate of misidentified background events was reduced to 1.7 ± 0.3 mHz at the cost of also reducing acceptance rate of real annihilation events by 25%. Since we can collect samples of annihilation events and cosmic events independently, these selection algorithms can be tuned on data- and background- samples with essentially no contamination.

2.2 Antihydrogen Synthesis and Confinement

The methods by which antihydrogen is produced and confined in ALPHA have been described in detail elsewhere [26, 17, 29, 30, 31], and will only be outlined here. A plasma of typically 2×10^6 positrons with a radius of about 1 mm and a temperature of ~ 40 K is prepared in the center of the trap. Next to it, in a potential like that shown in Figure 2.5 on the next page, we place an antiproton plasma with typically 10^4 particles at 100 K temperature and 0.5 mm radius. The antiprotons, being at low temperature and in an anharmonic well, can be made to resonantly follow a chirped drive applied to them through one of the Penning trap electrodes, a phenomenon known as autoresonance [32]. Once the antiprotons are phaselocked to the drive, the frequency and therefore amplitude of their axial motion can be controlled

by changing the drive frequency. Driving the antiprotons close to the potential of the positron plasma (see Figure 2.5), causes a large fraction of the antiprotons to be injected into the positrons with minimal relative energy, allowing for cold antihydrogen to be formed through a three-body formation process. From an injection like this, $\sim 10^4$ antihydrogen atoms are formed and on average one of them remains trapped with an energy less than $\sim 0.5\text{K}$. Here, we use Kelvin as a unit of energy. The conversion to Joule is obtained by multiplication with Boltzmann's constant, k_B .

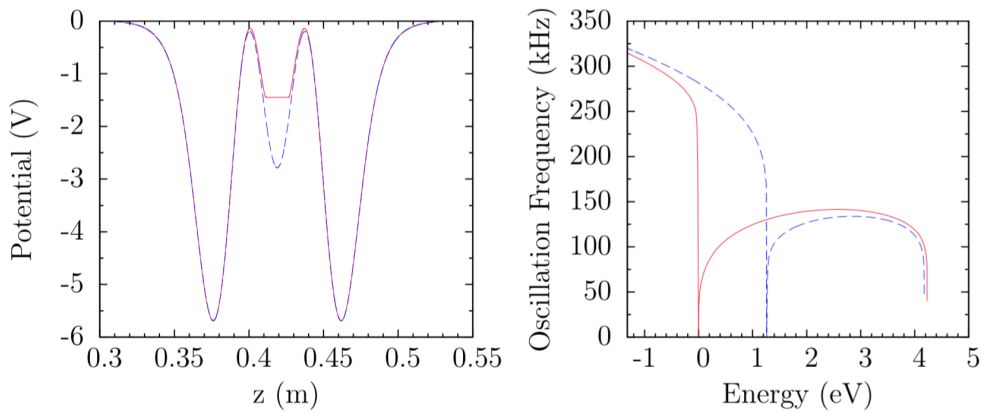


Figure 2.5: left: a typical on-axis nested potential for mixing antiprotons and positrons. The dashed blue line gives the potential produced by the electrodes alone, while the red solid line takes into account the space charge of the positrons. Right: the motion along the axis of the Penning trap of a confined particle is periodic with a frequency, which we call the axial bounce frequency. Plotted here is the calculated axial bounce frequency for an antiproton as a function of its energy in the left side-well of the nested potential. The energy scale is chosen such that an antiproton that can just barely pass through the positrons and reach the right side-well is assigned zero energy. Reproduced from [29].

Once any remaining charged particles have been forced out of the trap using electric fields, the neutral antihydrogen atoms left in the trap can be destructively detected by rapidly turning off the magnetic minimum trap. Our magnets are designed to allow the shutdown to happen with a time constant of 9 ms [34]. In Figure 2.6 on the following page, the results of simulating the trajectories of atoms from 3 different energy distributions are compared with recorded annihilation events during the magnetic shutdown [33]. It is clear from panel b) that out of the three considered, only the Maxwellian energy

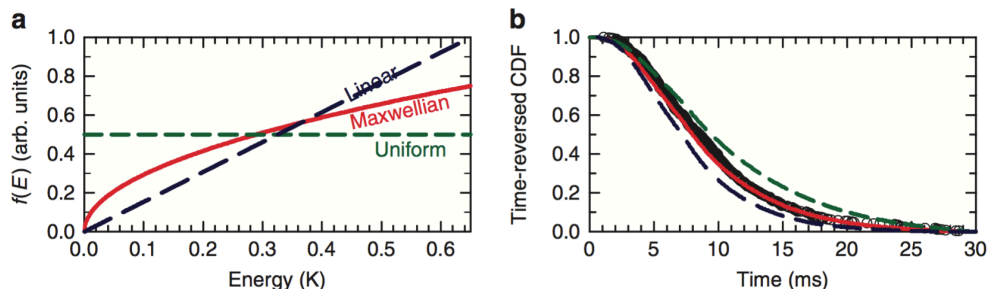


Figure 2.6: Comparison of (a) 3 different candidate energy distributions for trapped antihydrogen and (b) temporal distributions of simulated annihilation events from these distributions. In (b) is also plotted with black circles the measured distribution of 434 trapped atoms in ALPHA. These appear mostly as a band behind the Maxwellian distribution. Reproduced from [33].

distribution is consistent with data. This is in agreement with a model where antihydrogen is formed at the temperature of the positron plasma ($\sim 40\text{K}$) while only the extreme low-energy tail of this distribution ($< 0.5\text{K}$) can be trapped.

In order to verify that the annihilation signal recorded when the magnetic trap is turned off is indeed due to antihydrogen atoms, and not antiprotons that somehow failed to be expelled, we apply an electric field across the length of the trap while the magnetic trap is turning off. With this field in place, the annihilation positions and times of antihydrogen atoms are very different from those of bare antiprotons. Simulated distributions for both antiprotons and antihydrogen are shown in Figure 2.7 on the next page and compared to the initial 38 trapped antihydrogen events recorded in ALPHA [34, 17].

2.3 Laser System and Metrology

The $1S$ - $2S$ transition in (anti)hydrogen can be excited by 2 photons of equal wavelength near 243nm . The spectroscopy laser needs to have a) a narrow linewidth, b) accurate frequency control, c) a significant output power in order for a precision measurement to be feasible under current experimental conditions, and d) be easily tunable by more than 300MHz such that all the hyperfine states of the trapped antihydrogen atoms can be addressed. This section is dedicated to describing the 243nm laser system used in ALPHA, which in its current setup produces $\sim 100\text{mW}$ of 243nm light with a

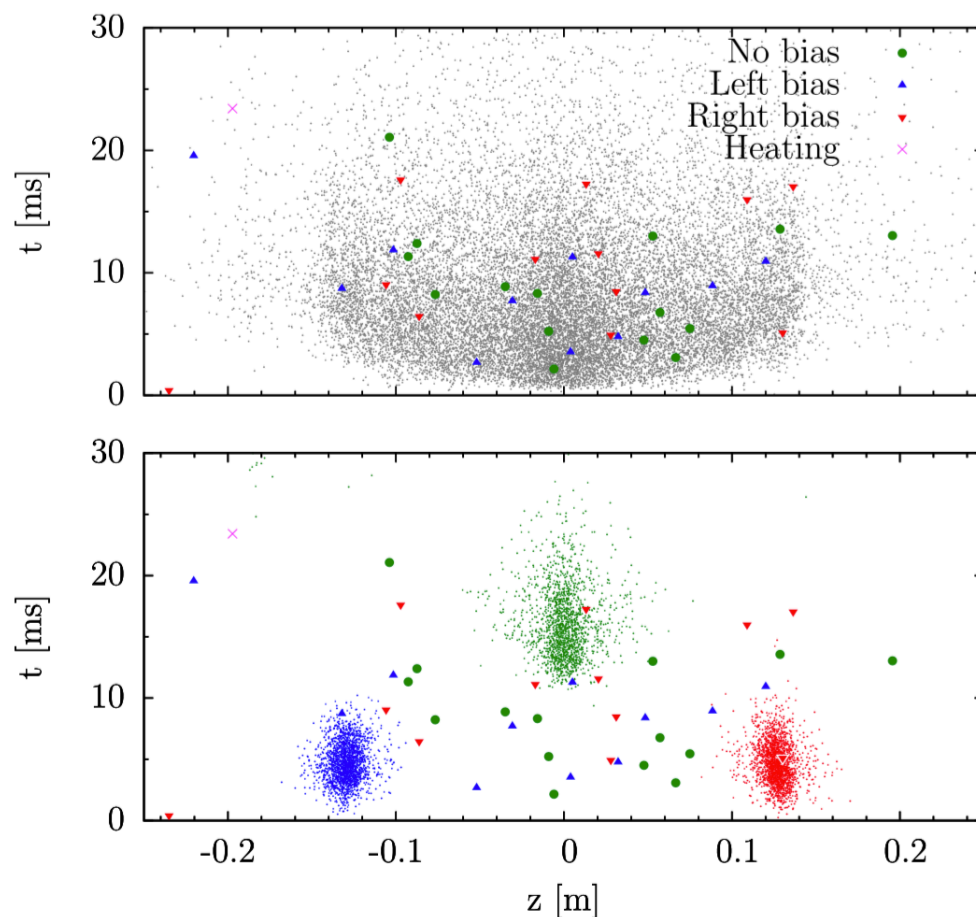


Figure 2.7: Top: simulated antihydrogen annihilation locations and times (gray dots) compared to data. Bottom: simulated antiproton annihilations with 3 different electric fields during the magnetic shutdown. Blue dots have the electric field pushing antiprotons to the left in this graph (negative z), red dots have the electric field pushing them right, and green dots are simulated with no electric field. The recorded annihilation points are color coded similarly for which electric field was applied during the magnetic shutdown. There is a single event from trials where the positron plasma was heated up in order to suppress the trapped antihydrogen signal, marked with a violet X. Adapted from [17].

long term frequency stability of < 1 kHz. This frequency is controlled through phase coherent referencing to a quartz oscillator, which is regulated using GPS clocks. We dedicate a subsection below to a more detailed description of this frequency control system.

The heart of the laser system is a commercially available, amplified and frequency quadrupled solid state laser. The master oscillator is a diode laser cavity in Littrow configuration, operating at 972 nm. This light is then amplified and frequency doubled twice in resonant doubling cavities in a bow tie layout, so as to reach 243 nm.

In order to reduce the linewidth, the master oscillator is actively stabilized to an ultra-stable reference cavity, which is a very high finesse cavity made from a single piece of Ultra Low Expansion (ULE) glass. The cavity is passively isolated from the outside world acoustically and thermally, and it is further actively temperature stabilized and acoustically and vibrationally stabilized.

Since the reference cavity is designed to not be tunable, we need to shift the frequency of part of the laser light such that we can simultaneously maintain resonance in the reference cavity as well as tune the spectroscopic laser beam to whichever frequency we want to probe. This is achieved with a double pass, Acousto-Optic Modulator (AOM), shifting the light going to the reference cavity. Operating the AOM in the double pass configuration mainly serves two significant purposes in our setup: Firstly, we fiber couple the output light from the AOM before it is injected into the reference cavity. This requires accurate alignment, which in a single pass AOM would cause a very narrow tuning bandwidth because of the frequency dependence of the Bragg angle. In a double pass setup however, this frequency dependence in the first pass can be cancelled by the second pass, giving a very good pointing stability of the output beam and effectively increasing the bandwidth quite drastically.

Secondly, passing the AOM twice gives a total frequency shift of twice the drive frequency. This can also extend the range of frequency shifts available, and can allow shifts outside the driving range of the AOM itself. For our particular setup, we shift by close to 500 MHz to get to the nearest resonance of the ultra-stable cavity, and ramp by ~ 75 MHz to address both the relevant transitions, to be described in chapter 5. With the double pass setup, this means that the AOM is driven at around 250 MHz, and needs a bandwidth of a little more than $75/2$ MHz in order to also account for the slowly changing resonant frequency of the ULE cavity.

The 243 nm light needs to be transported into the antihydrogen trapping apparatus from the laser laboratory situated in an adjacent room. The total

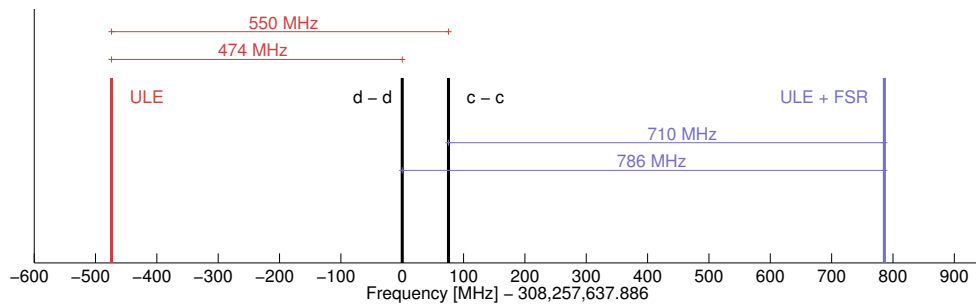


Figure 2.8: Relevant frequency shifts for addressing both the d-d and c-c transitions. This naming of the transitions will be explained in more detail in Chapter 5 on page 43. The black vertical lines indicate the frequencies of spectroscopic lines to be investigated, while the colored vertical lines are the nearest resonances in the reference cavity. The exact resonant frequencies in the ULE cavity is not controlled during manufacturing, so any given atomic line of interest can only be guaranteed to be within half of one Free Spectral Range (FSR) from a resonance in the reference cavity.

beam path is around 7 m, so to compensate for instabilities introduced in the transport, we actively stabilize the beam using matched sets of beam position detectors and piezo-actuated mirrors. This not only increases the pointing stability, but also allows for fine tuning of the alignment to be done remotely. Since radiation from the antiproton beam disallows operators from being near the antihydrogen trapping apparatus while the beam is on, this capacity is big operational advantage.

Frequency Control System

Precise spectroscopic measurements require accurate knowledge and control over the laser frequency. Figure 2.9 on page 21 provides an overview of how this is achieved in ALPHA. The master oscillator of the laser is locked to a ULE cavity through the AOM, which means that changing the AOM drive frequency, moves the frequency of the light going to the experiment, while the 972 nm light shifted by the AOM stays on resonance in the ULE cavity. A commercially available optical frequency comb [35] measures the frequency of the light going into the ULE cavity. Knowing the drive frequency of the AOM, this gives us knowledge of the frequency of the 972 nm seed, which eventually probes the antihydrogen atoms, to the same relative precision as that of the reference clock [36], in this case a GPS disciplined quartz oscilla-

tor.

Using this measurement, we continuously update the drive frequency of the AOM to keep the 243 nm at the desired frequency. The inherent drift of the ULE cavity, which is currently around 60 MHz/s, as well as environmental factors which might affect the ULE cavity are trivially corrected for in this scheme. An example of the measurement performed by the frequency comb, long enough to show the drift of the ULE cavity is given in Figure 2.10 on page 22.

In order to ensure accurate and consistent timing between the laser system and the antihydrogen production and trapping operations, these are all controlled by the same master sequencer. Thus, the laser frequency, the shutters allowing or disallowing the laser light from reaching the atom trapping volume, and even fine tuning of the beam alignment into the enhancement cavity are all controlled remotely with no operators needed in the laser laboratory. During a period of data taking like the one described in Chapter 7 on page 75, the laser and frequency control system would be prepared immediately before the beginning of a typically 8-hour beam period, and typically no further intervention on the laser system would be required for those 8 hours of data taking.

Allan Deviation

We have already given some numbers relating to frequency stability, and it is appropriate that we define more accurately what we mean before moving on. Atomic clocks and crystal oscillators generally contain noise components that require the usage of appropriate statistical tools. In particular, frequency modulating flicker noise ($1/f$ FM noise) as well random walk FM noise cause the standard deviation to be non-convergent. The Allan deviation is a measure of frequency instability that does converge with these types of noise present and coincides with the standard deviation for a dataset containing just uncorrelated white noise. There are several versions of the Allan deviation with different strengths. In the present text we use only the un-modified, non-overlapping kind, defined as [37]:

$$\sigma_{\text{Allan}}(\tau) = \sqrt{\frac{1}{2} \langle (\bar{y}_{n+1} - \bar{y}_n)^2 \rangle} \quad (2.2)$$

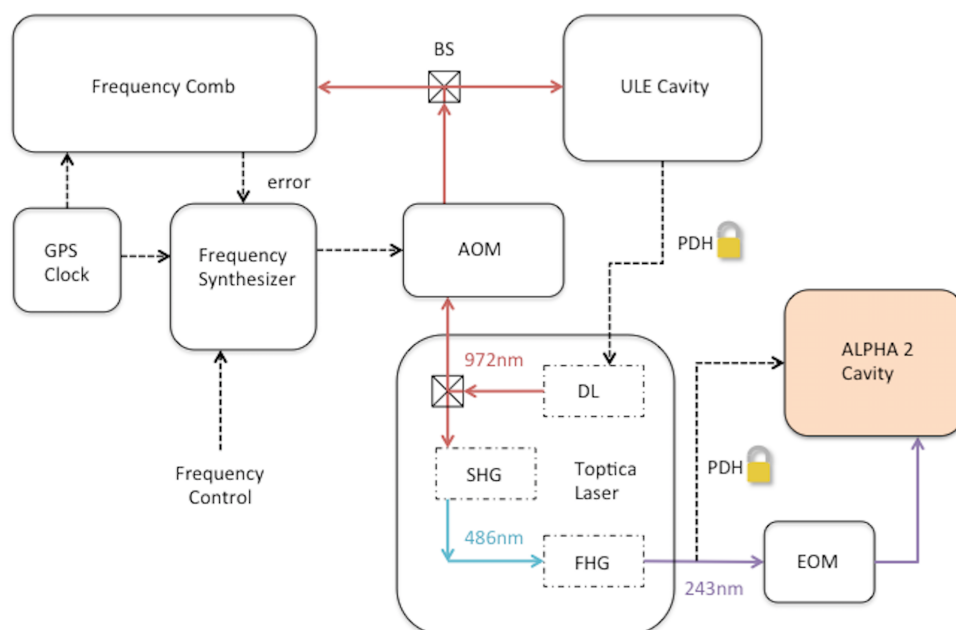


Figure 2.9: Schematic of the laser system. The dashed arrows symbolize signal flow, while the colored solid lines are laser beams. The laser seed is locked to the ULE cavity through the AOM, which provides the capacity for frequency tuning. The enhancement cavity for spectroscopy is in turn locked to the frequency of the 243 nm light.

\bar{y}_n is the average fractional frequency over the n th continuous interval of length τ , i.e. the average fractional deviation from the nominal frequency over the time interval τ . Note that this version of the Allan deviation is only appropriate for continuous datasets taken with dead time free, π -type counters, which provide an equal weighting of the signal obtained over the gate time. Our estimate of the frequency stability of the 243nm laser light is then this Allan deviation measured with an appropriate gate time at 972nm, and multiplied by 2 for each of the frequency doubling stages. Choosing for example a gate time of 100s, we arrive at an uncertainty of 343Hz for the 243nm light.

2.4 Enhancement Cavity

By exciting a 2-photon transition of interest with two counter-propagating photons, the first order Doppler shift can be cancelled. If the two counter-

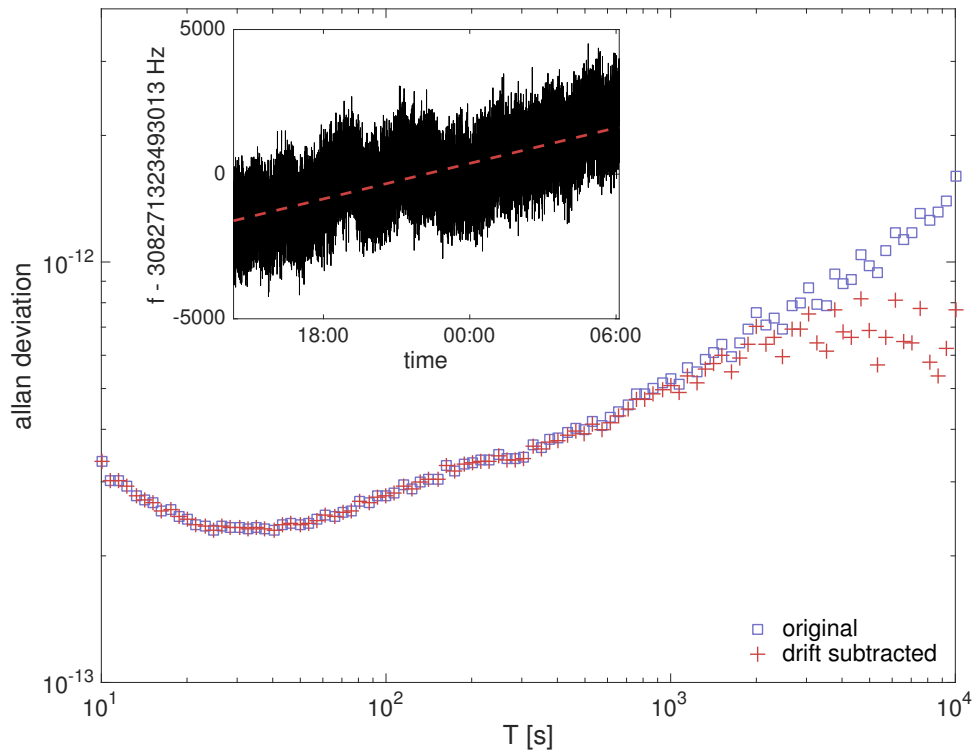


Figure 2.10: Allan deviation of the laser frequency at 972nm for a continuous ~ 16 hour measurement period. To illustrate the significance of the linear drift of the ULE cavity, we plot both the allan deviation before subtracting the linear drift and after. The inset shows the frequency measurements themselves, which are derived from measuring the beat note between the laser and one "tine" of the frequency comb. The measurements are shown with the 1 s inherent gate time of the RF counter, which measures this beat note. The detailed working principles of optical frequency combs can be found in [36].

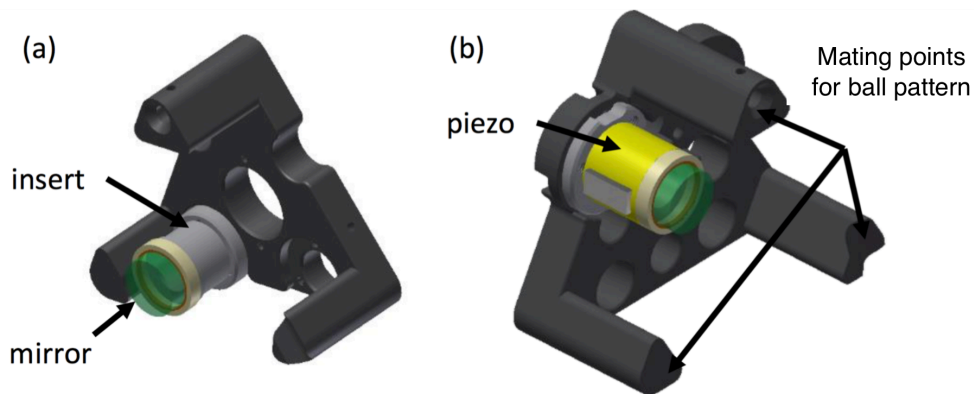


Figure 2.11: Support structures for the internal cavity mirrors. a) is on the upstream (US) side of the penning trap electrodes as seen by the antiproton beam, b) is on the downstream (DS) side. A piezo on the downstream end mirror is used to lock the cavity length to the laser frequency.

propagating beams are provided by a build-up cavity, the laser intensity available for driving the transition can be greatly increased. ALPHA-2 is designed with such a cavity encompassing the neutral atom trap, some of the design parameters are given in Table 2.1 on page 25, and a diagram, placing the mirrors with respect to the other key components of ALPHA is in Figure 2.12 on the following page. The cavity is near-confocal with a Radius Of Curvature (ROC) for both mirrors of 1 m and a mirror separation of 90 cm, giving a waist in the center of the neutral atom trap of $196 \mu\text{m}$. The cavity mirrors as well as the structures between them are cooled to cryogenic temperatures by a liquid helium bath. Under normal operating conditions the temperatures of structures supporting the cavity mirrors fluctuate by no more than 0.1 K.

In Figure 2.11 is shown the cavity mirrors in their triangular mounting structures. These structures each mate to a triangular pattern of 3 balls within the cryostat, which are precisely referenced to each other, such that the alignment of the cavity can be achieved through the precise machining of these mirror support structures. This alignment is furthermore reproduced any time the support structure and mirrors are inserted into the cryostat and mate on the ball pattern.

Placing cavity mirrors inside the UHV chamber is necessary to achieve a high finesse at this wavelength, but obviously limits the materials that can be used. Cooling the mirrors to liquid helium temperatures furthermore re-

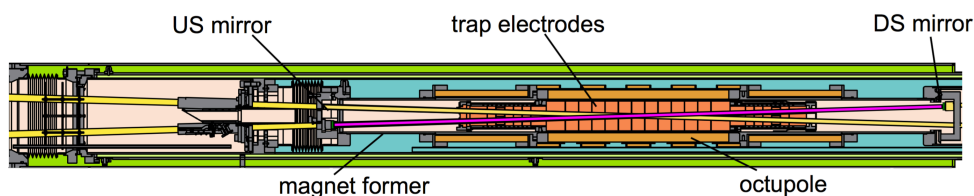


Figure 2.12: Diagram showing the positions of the internal cavity mirrors with respect to the Penning trap electrodes (orange), the superconducting magnet windings (brown), and the vacuum chamber. The blue volume is filled with liquid helium, cooling the superconducting magnets, while green denotes the Outer Vacuum Chamber (OVC), needed to thermally isolate the liquid helium from the outside world.

quires careful consideration of the differential contractions. In ALPHA-2, the fused silica mirror is suspended in a mirror cell, comprised of a titanium ring, large enough to surround the mirror whilst leaving a gap, and a cryogenic- and UHV-compatible epoxy glue, filling that gap. If the bonding material filling the gap has an expansion coefficient between those of the central substrate and the outer ring, the size of the gap can be tuned such that the differential contractions approximately cancel, leaving almost no stress on the cold mirror. This approach is inspired by, but simplified from that of [38].

External Cavity

While it is the original and current intention of ALPHA to perform a 1S-2S measurement in the cavity described above, a failure during the beam season of 2015, which was later identified as a broken glue-joint, had us considering other options. At the time of the failure, the inaccessibility of the cryogenic parts in the UHV chamber would have made any intervention to fix this broken joint very time consuming, and almost certainly would have occupied the remainder of the beam season. The decision was therefore made to instead build an additional cavity, mounting mirrors in the room temperature parts of the vacuum in a much less invasive operation, thus maintaining a chance of measurement in the same beam season. While both cavity mirrors were still inside the UHV chamber, we refer to this setup as an external cavity because of the decoupling of the cavity mirrors from the cryogenic parts of the apparatus.

The design Finesse of the external cavity was lowered compared to the internal cavity so as to not make the cavity too difficult to keep locked, since

this cavity would be much longer than the internal one, and not have the advantage of the very thermally stable environment of a liquid helium bath. The ROC of the mirrors also had to be increased to make a stable cavity of nearly 3m, which lead to a larger beamwaist, which in turn further limits the maximum intensity produced in the cavity. Since the symmetric placement of mirrors around the magnetic trap could not be conserved, the beam size seen by the atoms is larger than w_0 , averaging to $277\ \mu\text{m}$ over the length that trapped atoms can explore.

Figure 2.13 on the following page shows the mounting of the external cavity mirrors. To allow for online angular adjustment of the mirror, it is placed between two flexible bellows. At the far end of this assembly, the vacuum window is fixed at a distance from the main vacuum chamber, preventing the complete compression of the bellows holding the cavity mirror by the vacuum forces.

This cavity was kept locked to the frequency of the laser at an average

Table 2.1: Design parameters for the internal and external enhancement cavities. We use R_1 for the reflectivity of the input coupler, and R_2 for that of the output coupler. The listed enhancement factor, b , is affected by loss in the input coupler and the number given here is calculated using our own measurements of the transmission of these mirrors as well as the reflectivities quoted by the manufacturer, as $b = I_c/I_0 = T_1/(1-\sqrt{R_1 R_2})^2$. This assumes ideal mode matching and 100%.

Type	Length	R_1	R_2	Finesse	w_0	Linewidth	b
Internal	90 cm	0.99	0.995	417	$196\ \mu\text{m}$	400 kHz	135
External	270 cm	0.985	0.985	207	$265\ \mu\text{m}$	270 kHz	63

efficiency of $\sim 90\%$ for the experiments described in Chapter 7 on page 75. The locking electronics were set up such that the cavity would automatically re-lock whenever the lock was lost. This eliminates the need for operator intervention during data taking runs, as the cavity locks as soon as the laser light is allowed into it by the shutters.

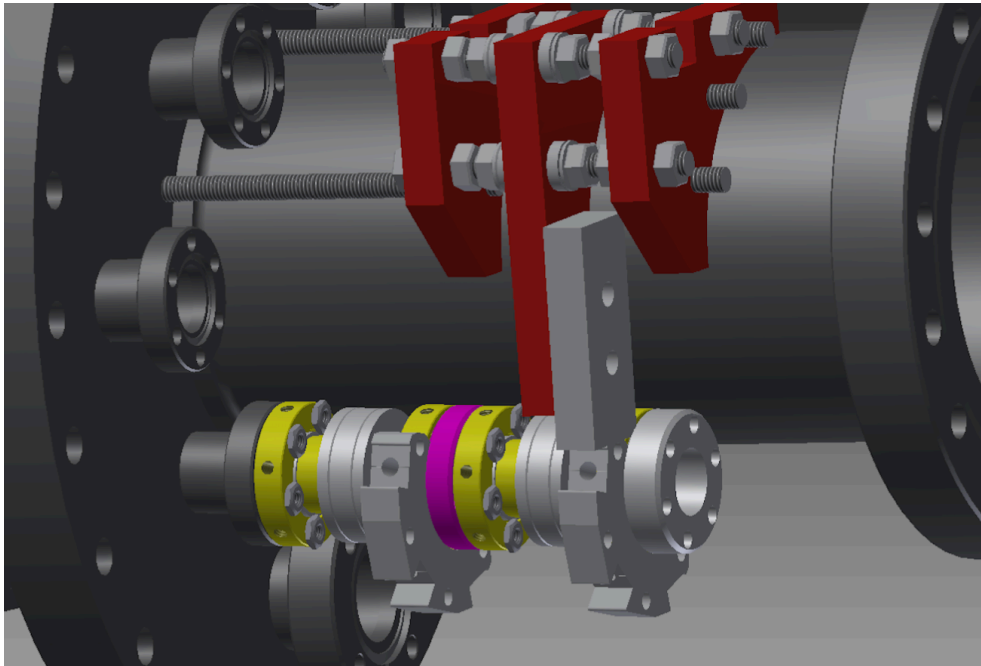


Figure 2.13: External cavity mirror assembly mounted on the downstream vacuum chamber. The mirror is mounted in the central (magenta) part and allowed angular adjustment due to the flexible bellows, which are symbolised by the two gray cylinders between yellow flanges in this rendering. The center of the trapping volume for antihydrogen is about 1.6m to the left of the frame.

Chapter 3

Gravitational Free-fall of Antihydrogen

ALPHA detects with good spatial and temporal resolution the annihilation positions of antihydrogen atoms released from a magnetic minimum trap. These positions carry information of the total force acting on the atoms, which includes a small component from the interaction with Earth's gravitational field. Measuring directly the gravitational force on antimatter is of great interest as it tests the weak equivalence principle in an as of yet unexplored domain and may provide clues to the matter/antimatter asymmetry as well as CPT symmetry [39].

While there are good arguments why the gravitational mass of antimatter cannot be different from that of ordinary matter, a select few are argued in [40, 41, 42, 43], these arguments are either model dependent, assuming a particular way a theory of gravity must be constructed, or rely on postulates like perfect CPT invariance. Thus, these arguments are not universally found compelling [39, 44, 45], and both the AEGIS (currently active) and GBAR (under construction) experiments at the AD facility at CERN are designed for measuring the gravitational acceleration of antihydrogen. Both experiments aim to achieve an accuracy of 1% on this measurement.

This chapter reports on a retrospective analysis [33] of the annihilation positions of 434 trapped antihydrogen atoms in ALPHA recorded during the data taking seasons of 2010 and 2011, looking for a preference for the annihilation positions to be on either the top or the bottom of the trap. From this analysis, we rule out at the $P = 0.05$ level, both that the size of the gravita-

tional mass of antihydrogen is larger than 110 times the inertial mass, and that it is smaller than -65 times the inertial mass, assuming for both limits the worst case systematic errors.

3.1 Data and Analysis

Antihydrogen is produced and trapped as described in Section 2.2 on page 14. Before releasing them, they are all held for 400ms or longer, ensuring that more than 99.5% of the atoms have decayed to the ground state [30]. Because the magnetic minimum trap in ALPHA is superimposed on a Penning-Malmberg trap with the same symmetry axis, the axial fields of the mirror coils add linearly to the solenoid field, while the radial fields produced by the octupole magnet add in quadrature. This means that as current in the trapping magnet is turned down, the radial confinement is weakened faster than the axial confinement. Because of this, most trapped atoms will escape radially and annihilate in the region between the mirror coils, on a timescale dominated by the near exponential decay of the octupole field. In Table 3.1 is listed the trap depth of the magnetic trap at various times after the fast shutdown has been initiated, along with relevant potential energies of the trapped atoms.

The equation of motion for the atoms, including the gravitational interac-

Table 3.1: The magnetic trap depth at various times, gravitational potential energy difference between the top and bottom of the trap, and potential energies from electric fields in the trap. The "Gap" electric potential energy is typical for an atom approaching the gap between two electrodes, while the corresponding "Patch" value is for an atom approaching a patch region on the electrodes.

	Energy [mK]	Condition
Minimum-B trap depth	540	0ms
(without gravitational effects)	100	10ms
	11	20ms
	1.2	30ms
Gravitational potential energy	0.053	$F = 1$
	5.3	$F = 100$
Polarizational potential energy	2.7×10^{-7}	Gap 10V/mm
	2.7×10^{-9}	Patch 1V/mm

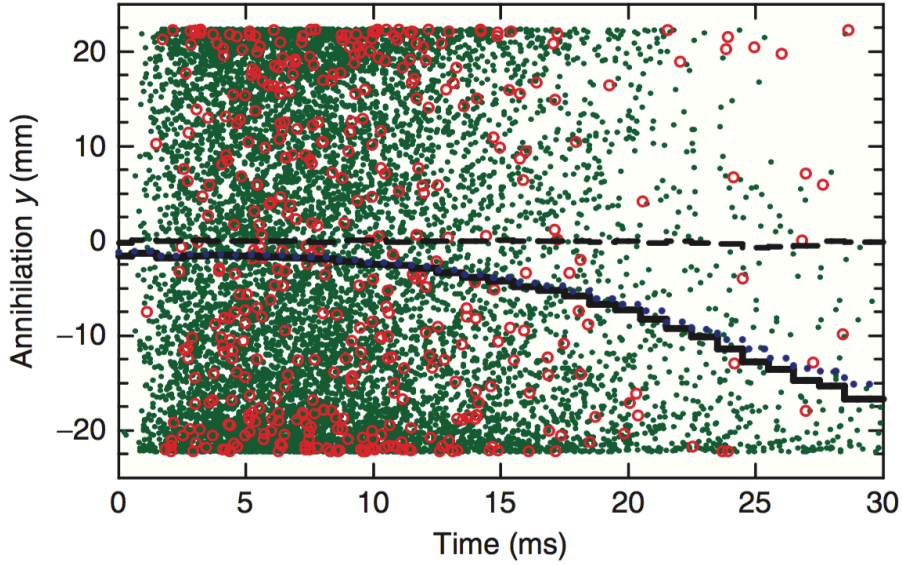


Figure 3.1: Time and vertical (y) position of the measured antihydrogen atoms (red circles) as well as of a sample of 10,000 simulated atoms with $F = 100$ (green dots). The solid black line shows the average position in each time bin for $\sim 9 \times 10^5$ simulated atoms with $F = 100$, The blue dotted line consider these same atoms, but takes into account the finite azimuthal resolution of the detector. The dashed black line shows the average position of a similar number of simulated atoms with $F = 1$. Reproduced from [33].

tion is:

$$M \frac{d^2 \vec{r}}{dt^2} = \nabla (\vec{\mu} \cdot \vec{B}(\vec{r}, t)) - M_g g \hat{y} \quad (3.1)$$

We simulate atom trajectories through the shut down of the magnetic trap using this equation and compare the simulated annihilation locations to the measured ones. We can do this for different ratios of the gravitational to inertial mass,

$$F \equiv \frac{M_g}{M} \quad (3.2)$$

We can then set limits on the possible values of F that are compatible with our dataset.

Reverse, Cumulative Average Analysis

As can be seen in Figure 3.1, the atoms that escape the trap at late times are more sensitive to gravity. These are the coldest atoms, so the small gravi-

tational potential difference across the trap has a relatively larger effect. Unfortunately, a Maxwellian energy distribution of atoms, as we have seen best describes our trapped sample, does not contain very many of these cold atoms that escape at late times, so looking only at very late times is not an advantageous strategy. A useful way to visualise this kind of data is through the reverse cumulative averages of the annihilation distributions, which place a higher emphasis on the later events, while not throwing away the information at earlier times. The reverse cumulative average at a given escape time t is the average position of all events at later times than t . In other words, it is the cumulative average obtained by starting at $t = \infty$ and moving backwards in time.

Figure 3.2 on the next page presents the reverse cumulative averages of the measured annihilation positions along with those of simulated atoms for three different strengths the gravitational interaction. For $|F| < 60$, our data is visually compatible with either sign of gravitational interaction, while for $|F| = 150$, our data looks incompatible with both an upwards- and a downwards-pointing force.

Monte Carlo Analysis

In order to set more quantitative limits on F than what can be qualitatively done by eye from Figure 3.2, we employ a method, which we will merely outline here. A detailed description can be found in [33]. It is based on calculating a test statistic, which quantises how incompatible a set of annihilation points (y, t) is with a given distribution. This test statistic is calculated for each F , comparing our 434 events to a distribution of a large number of simulated events with that F . Then, an additional large number of simulated events is generated and subdivided into N sets of 434, and the test statistic is calculated for each of these N sets in order to estimate the sampling distribution for our test statistic. We can then derive a P-value from the number, $N_>$, of simulated sets of events that give a larger (less compatible) value of the test statistic, $P = N_>/N$.

Systematic Effects

The P-value as calculated above does not take into account any systematic effects in the experiment. In order to correct for this, we model the two main possible sources of systematic errors. Firstly, the detector axis may be dis-

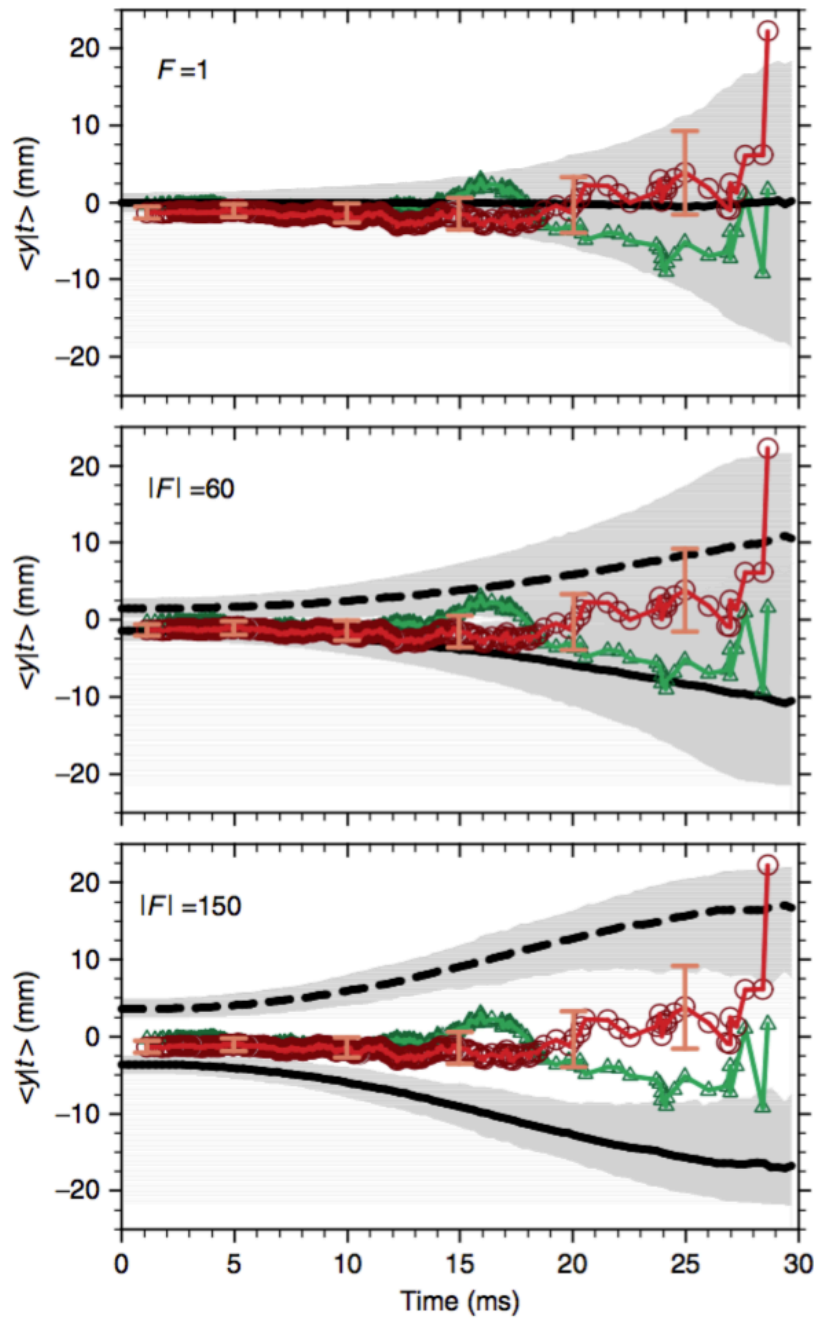


Figure 3.2: Reverse, cumulative averages of annihilation data as well as simulations for different values of F . Red circles are the vertical (y) positions of the annihilated antihydrogen atoms, green triangles are the horizontal (x) positions, kept for comparison. The solid black line is for a simulated gravitational force pointing the same way as regular gravity, $F = |F|$, while the dashed is the equivalent simulation for antigravity, $F = -|F|$. Reproduced from [33].

placed with respect to the magnetic trap. This would cause an overall shift in annihilation positions at all times. Mechanical constraints limit this error to at most ± 5 mm. Secondly, the axis of the octupole may be offset from the axis of the electrodes, which define the surface the atoms annihilate on. This would cause a shift in the average annihilation locations larger than the distance between the axes, since the misalignment would cause the magnetic well depth to be reduced on one side. By simulating such an offset, we find that the overall offset observed in the measured annihilation positions of $\langle y \rangle = -1.3 \pm 0.8$ mm could be caused by a shift in the octupole axis of just -0.06 mm. This happens to be almost exactly the largest shift of the octupole allowed by mechanical constraints.

Electric polarization effects could also be considered, and would be major source of error for excited antihydrogen atoms. Only by requiring that atoms be trapped long enough to have decayed to the ground state, are the potential energies from electric fields in the trap those listed in Table 3.1 on page 28 and safely neglected. A more comprehensive list of the systematic effects that have been considered is in [33].

In Figure 3.3 on the next page we plot the estimated P-value as a function of F , considering the extreme points of the systematic effects described above. If we initially ignore all systematics, our dataset excludes at the $P < 0.05$ level $F > 75$ and $F < -12$. A much more conservative approach is to assume the worst case systematic error for each sign of F , even if those systematics are not mutually consistent. In this case, we exclude at the same confidence level $F > 110$ and $F < -60$.

3.2 Future Improvements

The limited sensitivity of this measurement is easy to understand from Table 3.1 on page 28: The gravitational potential energy difference across the trap is small compared to the kinetic energies of the trapped atoms, which range all the way up to the 0s well depth of 540 mK. Adding to this the fast time constant for turning off the magnetic trap, there is little chance for gravity to affect the annihilation positions.

This ratio of energies can be improved by either cooling the trapped antihydrogen to lower temperatures or by increasing the physical height of the trapping volume and thereby the potential difference between top and bot-

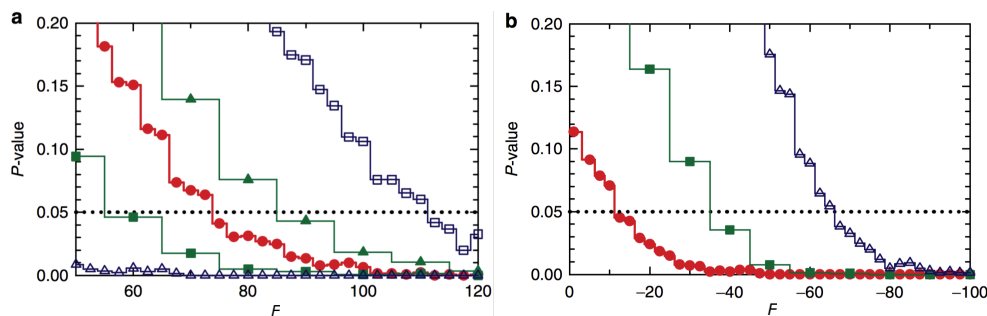


Figure 3.3: Estimated P-values as a function of F for (a) $F > 0$ and (b) $F < 0$. Red circles assume no systematic errors, blue hollow squares assume a detector displacement of -5mm , blue hollow triangles assume a detector displacement of $+5\text{mm}$, green solid triangles assume an octupole axis displacement of $+0.05\text{mm}$, and the green solid squares assume an octupole axis displacement of -0.05mm . In (b), no blue hollow squares or solid green triangles are shown as the P-values with these systematics are essentially zero. Reproduced from [33].

tom. There are of course limits to both of these approaches. A casual look at the relative energies in Table 3.1 might lead one to suggest simply increasing the height of the trap by a factor of 100, which is currently practically unfeasible at the AD facility, but not unthinkable.

Cooling of the trapped antihydrogen atoms can be achieved either through adiabatic cooling, i.e. manipulating the shape of the magnetic trap to slow down the atoms, or through laser cooling. Estimates from simulations using the ALPHA geometry and pulsed laser parameters indicate that significant laser cooling can be achieved in 200s, which is much shorter than demonstrated holding times for antihydrogen. Further, the final temperatures, reached after very long cooling times approach 20mK [46].

Obtaining a colder sample of antihydrogen is also of great interest for the spectroscopy efforts, since colder atoms can be contained in a smaller volume, the dominating broadening effects would be reduced, and the rate of excitations would be increased.

In Figure 3.4 on the next page are shown the results of simulating colder atoms through a slower shutdown of the magnetic trap and considering only the cases $F = 1, 0, -1$. Assuming similar statistics to the dataset analysed above, we plot the 90% confidence regions for a set of 500 annihilation

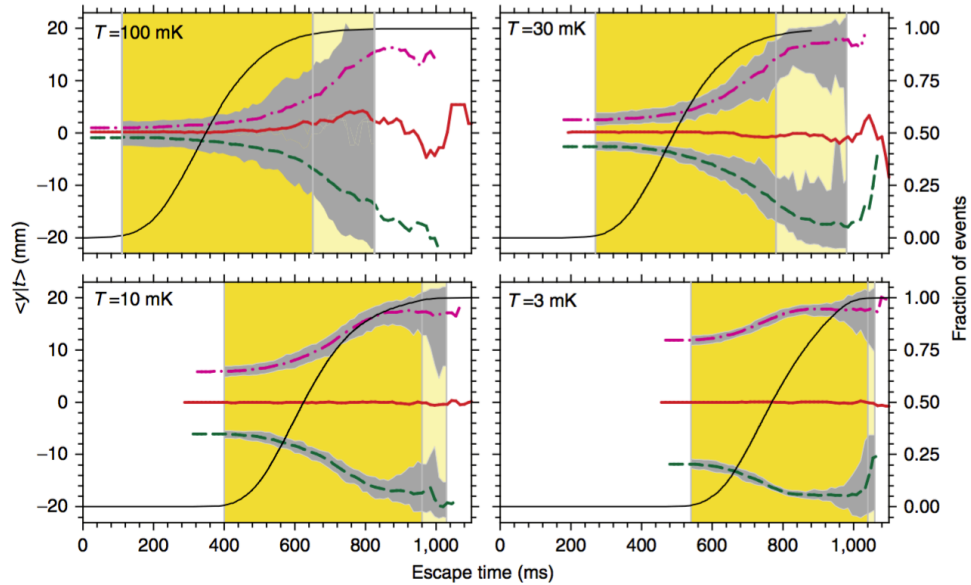


Figure 3.4: Reverse, cumulative averages of simulated antihydrogen atoms cooled to the temperature T . The magenta dash-dotted line uses $F = -1$, the green dashed line uses $F = 1$, and the solid red line uses $F = 0$. The gray bands are the 90% confidence regions for a sample of 500 annihilation events. The dark yellow region indicates a ratio of trapped antihydrogen signal to background cosmic events of better than 5, assuming an average trapping rate of 1 atom per trial, and the light yellow region indicates that same signal to noise ratio for a trapping rate of 10 per trial. The shut down of the magnetic trap has been slowed down by a factor 10 for these simulations. The thin black solid line shows the fraction of atoms that have annihilated. Reproduced from [33].

events around the $F = 1$ and the $F = -1$ reverse, cumulative averages. In the case of a 100mK sample, these regions still just about overlap, while for a temperature of 30mK and below, the confidence regions are clearly separated at all escape times. At a temperature of $T = 3$ mK a sample of 500 annihilations would clearly be able to distinguish between fractional values of F , i.e. provide more than one digit on the measurement of a gravitational interaction of size $|F| = 1$.

Chapter 4

Charge Neutrality of Antihydrogen

The charge of ordinary atomic and molecular matter is known to be no greater than $10^{-21} e$ for a number of different species, including H_2 , He and SF_6 [47]. While CPT symmetry would require the same to hold true for antimatter, the experimental bounds are much less strict. An indirect limit can be derived from the knowledge of the respective charges of antiprotons and positrons. The antiproton charge is bounded by spectroscopic measurements of antiprotonic helium to within 0.7 parts per billion (ppb) of the elementary charge [23]. The positron charge is less strictly bound: The limit on the fractional deviation from the elementary charge, known as the charge anomaly is about 25 ppb [48]. This is then also the limit inferred on the charge of antihydrogen, $|Q| < 25 \times 10^{-9} e$.

The first direct measurement on antihydrogen was the observation [49] that Lorentz forces were not sufficient to deflect a beam of high energy ($1.94 \text{ GeV}c^{-1}$) antihydrogen beam away from a detector. A more recent measurement [50], looking for a deflection due to electric fields in the ALPHA trap, sets a much tighter limit of $Q = (-13 \pm 11 \pm 4) \times 10^{-9} e$ (1σ confidence level).

In this chapter we describe an improved measurement [51] on the charge neutrality of antihydrogen, deriving from the (lack of) stochastic acceleration of trapped antihydrogen atoms in ALPHA-2 a limit of $|Q| < 7.1 \times 10^{-10} e$ at the 1σ confidence level) - a 20-fold improvement on our previous measurement. Assuming charge superposition and the best measured value for the antiproton charge, this measurement improves the experimental limit on the positron charge anomaly by a factor of 25.

4.1 Experimental Procedure

A trapped atom with a putative charge subjected to stochastic (i.e. randomly varying in time) electric fields will receive kicks in energy and perform an approximate random walk in energy. This random walk will on average eventually bring the atom's energy above the well depth of the confining trap, allowing it to escape.

For this measurement we stochastically switch the electric potential in the trap between the one shown panel c of Figure 4.1 on the following page and its inverse. The potential is switched 1698 times in a sequence of randomized time intervals averaging 1 ms. The potential is then turned off for 0.6 before the same sequence of switching potentials is applied again. We repeat this sequence 50 times to get a total of $N = 84\,900$ potential changes in a total time of 114.9s. See Figure 4.2 on page 38 for an outline of this sequence as well as measured responses of various electrodes in the trap. The magnetic trap is then turned off and we record how many antihydrogen atoms survived this treatment.

As well as trials that apply the stochastic acceleration scheme described above, we perform a null experiment, consisting simply of holding trapped antihydrogen for the same total time as in the stochastic trials, but applying no potentials. During the data taking, the stochastic and null trials were strictly alternated to cancel any effects of fluctuations in the rate at which we trap antihydrogen between the two sets. Any significant deficit in the rate at which atoms survive the stochastic trials compared to the null trials, would then indicate a charge of the antihydrogen atom. In order to avoid experimenter bias, data taking was stopped after a predetermined number of both stochastic and null trials, the results of which are given in Table 4.1 on page 40.

4.2 Data and Analysis

We need to estimate the charge that antihydrogen could have and still be consistent with the counts in Table 4.1 on page 40. As pointed out in Section 2.2 on page 14, the energy distribution of trapped antihydrogen in ALPHA is consistent with a 3D Maxwellian at high temperature, compared to the well depth of $\mathcal{E}_{\text{well}} = 0.54\text{K}$. The average energy along the z-axis is the 0.1 K.

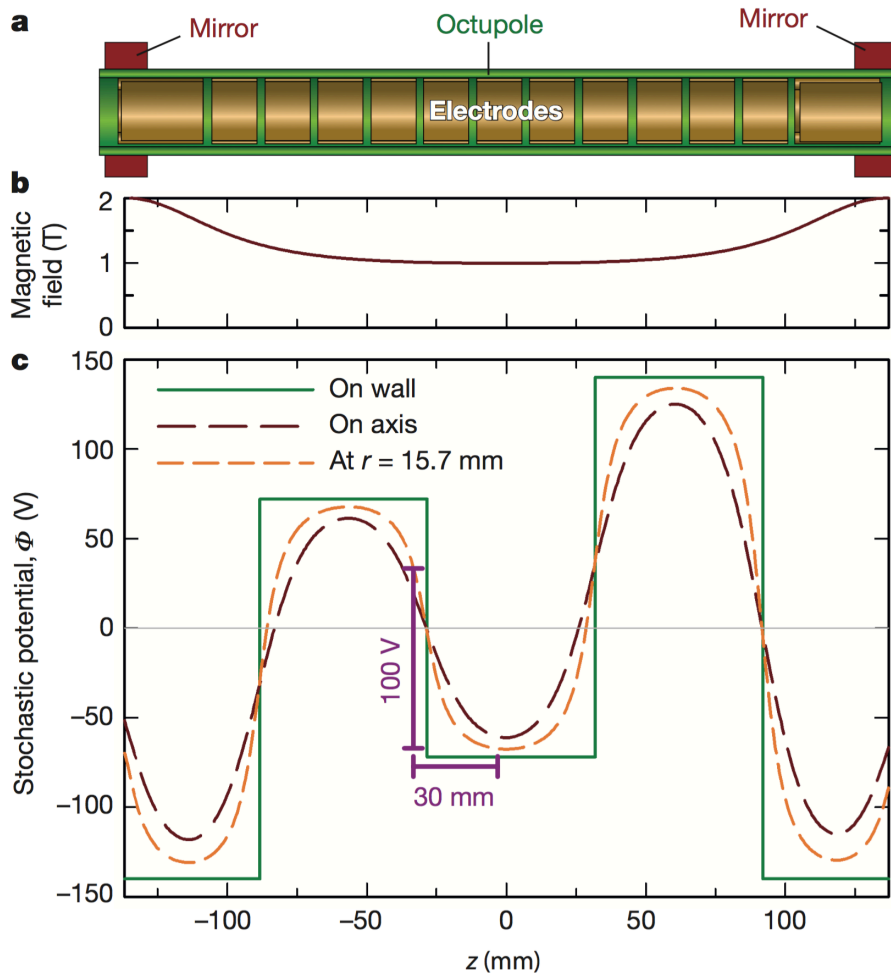


Figure 4.1: **a**: Electrode structure in ALPHA-2, with the positions of the outer mirror coils as well as the octupole windings indicated. The aspect ratio has been stretched vertically for clarity. **b**: On-axis magnetic field during the experiment, showing the axial potential well formed by the mirror coils. **c**: Snapshot of the applied stochastic electric potentials at several radii. The 'On wall' potential is on the inner surface of the electrodes, at $r = 22.3$ mm. The purple brackets indicate a typical distance covered and potential difference in 1 ms for an antihydrogen atom with 0.1 K of energy. Reproduced from [51].

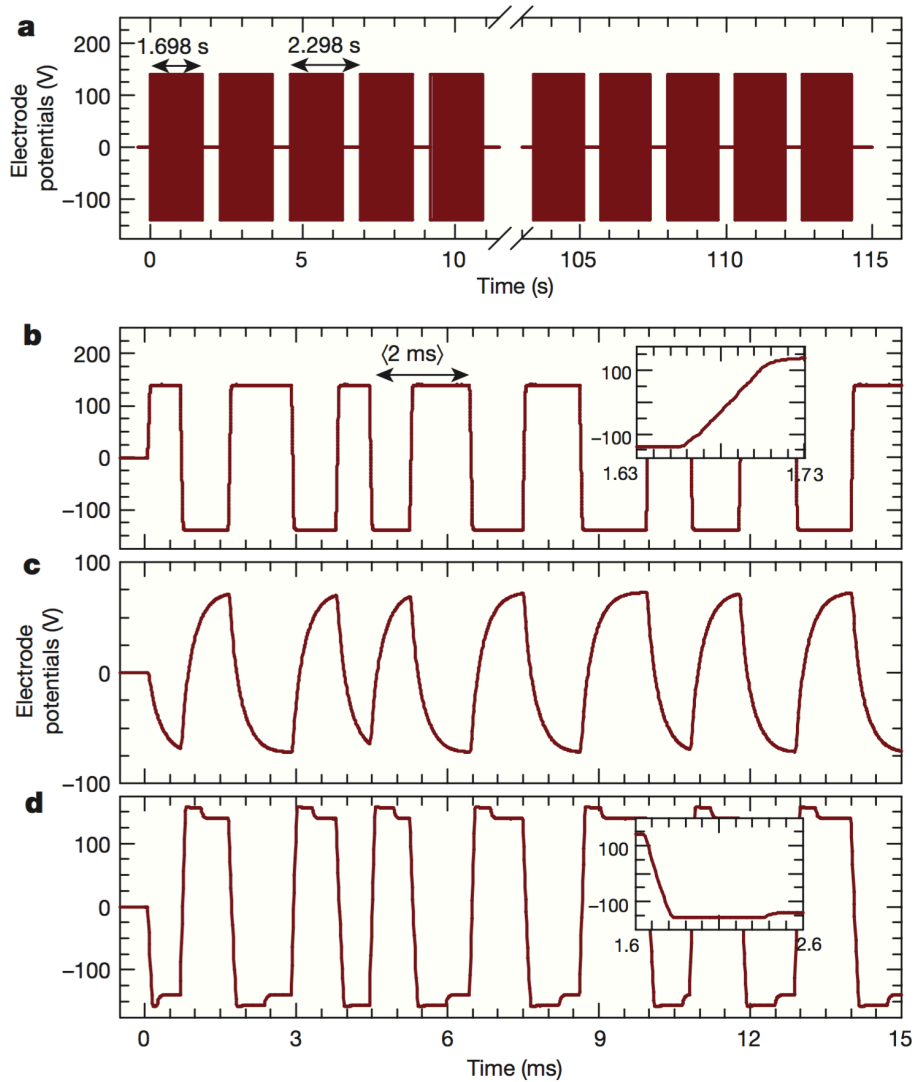


Figure 4.2: **a**: Time structure of the stochastic drive repetitions. The drive is active in the first 1.698 s of each of the 50 repetitions, which are spaced by 2.298 s. **b-d**: Time histories of the applied potentials as measured on various electrodes. Note that the time between changing the potential varies stochastically. The insets show on a finer time scale a single change of potential. Reproduced from [51].

The average time between switching the fields in our randomized sequence is 1 ms, which means a typical distance covered by the trapped atoms is about 30 mm. Figure 4.1 on page 37 then gives a typical potential change experienced by a trapped atom in a single switching of potentials of $\Delta\Phi \approx 100$ V. From a simple random walk model, the average energy of an atom carrying the charge Qe after N kicks is $|Q|e\Delta\Phi\sqrt{N}$. Thus, the atom is expected to escape if:

$$|Q| \gtrsim \frac{\mathcal{E}_{\text{well}}}{e\Delta\Phi\sqrt{N}} \quad (4.1)$$

Evaluating this for our experimental parameters gives a $|Q|$ of $1.6 \times 10^{-9} e$. Of course, this value depends on our somewhat rough estimate of the average energy kick, it assumes zero initial energy, and it does not take into account the different responses of the electrodes shown in Figure 4.2 on the preceding page. Thus, to refine our estimate, we simulate [52] trajectories of atoms with an assigned $|Q|$ and subject it to the stochastic fields described above. The null trials are also simulated by propagating atoms with no applied potentials.

In Figure 4.3 on page 41, we plot the survival rate in this simulations as a function of the charge assigned to the atoms. While it is clear that the limit set on $|Q|$ from these simulation data should be somewhere close to 1 ppm, it is not immediately clear which value of s to choose as the value ruled out from the data in Table 4.1. The obvious frequentist approach to estimating how incompatible our data is with a null hypothesis of some value of s , would assume Poissonian statistics and use a value for the underlying rate r , at which antihydrogen is trapped, determined by the 10 null trials. While this is a valid approach, it is quite sensitive to the value of r , which is not very well determined by just 12 events in 10 trials.

Instead, we employ a Bayesian analysis, described in detail in the methods section of [51], which is less sensitive to r . This analysis suggests $s > 0.79$, which, by the inversion of Figure 4.3, corresponds to $|Q| < 0.59 \times 10^{-9}$. This number includes no systematic effects and a wide range have been investigated using simulations to quantify their effect on s . Both the uncertainty in the applied electric potentials as well as the details of the shape of the magnetic minimum trap are largely inconsequential for the value of s . There is however some dependence on the initial energy distribution of the antihy-

Table 4.1: Recorded events in the stochastic and null trials.

	Number of trials	Observed antiatoms
Stochastic trials	10	12
Null trials	10	12

drogen atoms, and even though we have good cause to exclude both a uniform and a linear energy distribution (as presented in Figure 2.6 on page 16) we use these distributions to bound the possible uncertainties in the initial energy distributions. Finally, this degrades our limit on the antihydrogen charge to $|Q| < 0.71 \times 10^{-9}$.

One systematic effect which is negligible at the current precision, but will ultimately limit the precision of this type of measurement is the ground state polarizability of the antihydrogen atom. The present measurement can, by assuming that the charge is zero (and further that the static electric dipole moment is zero), be interpreted to set a limit on this polarizability. This results in a limit of $\alpha_{\bar{\text{H}}} < 3 \times 10^6 \alpha_{\text{H}}$, not including systematics, where α_{H} is the ground state polarizability of regular hydrogen.

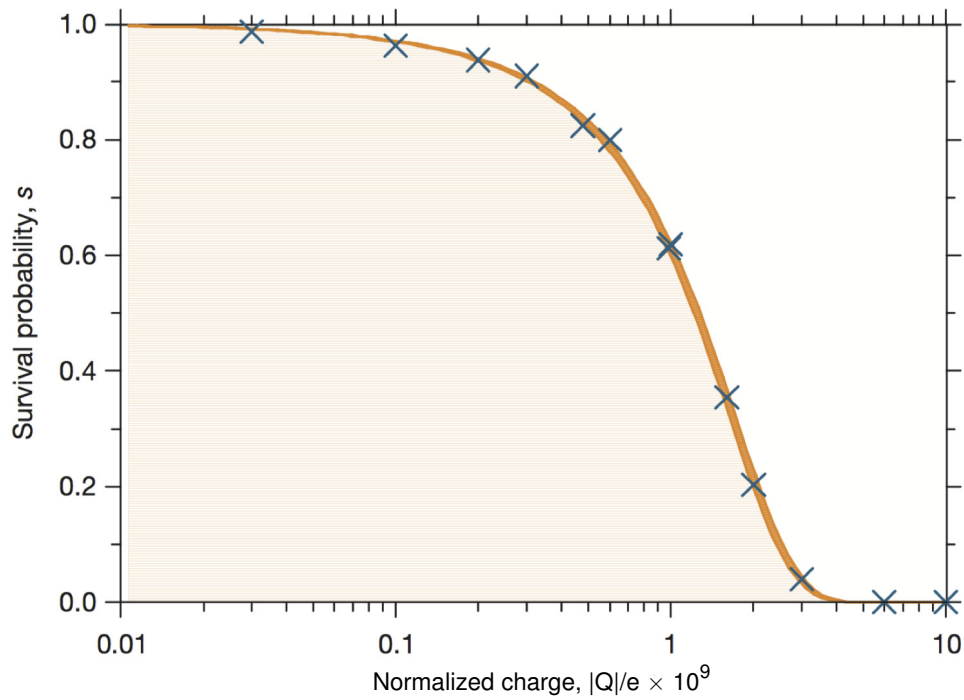


Figure 4.3: Simulated survival probability as a function of $|Q|$. The blue crosses are the number of surviving atoms at a given $|Q|$ divided by the number of surviving atoms in the simulation of null trials. The dark orange band is the 1σ confidence region resulting from a Bayesian fit to the simulated data. 1000 atoms have been simulated for each value of $|Q|$ plotted. Reproduced from [51].

Chapter 5

Atomic Theory of Antihydrogen

This chapter covers the results from atomic physics necessary to realistically evaluate methods for realising a measurement of the 1S-2S transition in antihydrogen in the ALPHA experiment. One might think that since a primary objective for this measurement is the comparison to the very precise measurements already obtained in hydrogen, the most direct approach would be to perform the exact same experiment on antihydrogen, with the same systematics and minimal theoretic modeling needed. While this is indeed attractive, the experimental reality of antihydrogen quite different from that of hydrogen, and the particular experimental conditions that result from this do need to be considered. Especially the low number of atoms available and the strong magnetic fields needed to confine them affect the treatment we will give here. Evaluating different spectroscopic methods in the light of current experimental parameters for antihydrogen is left for Chapter 6.

While some of the results obtained in this chapter are necessarily identical to those for hydrogen, the equations are generally cast in the form appropriate for antihydrogen, flipping the signs of all charges. We will in general use symbols ω , Ω with various subscripts to indicate angular frequencies, measured in rad/s, while f will denote frequencies in Hz, compatible with the international system of units (SI).

5.1 Energy Levels of Antihydrogen

We need to calculate the energies of states in the (anti)hydrogen atom for two purposes, and we require different levels of accuracy for the two: firstly,

we want to know the transition frequency of the 1S-2S transition that we will be driving. Since both the transition and the excitation laser have a narrow linewidth, we need to be quite accurate in this calculation and we will include effects of size down to about a kHz.

Secondly, we need to calculate the interactions between 2S and 2P states. For this purpose we can accept errors at the percent level, so for the energy differences which are of order 10 GHz, we can ignore effects smaller than a few MHz.

1S-2S Transition Frequency

To get the transition frequencies between the individual hyperfine states of the 1S and 2S levels, we will calculate the hyperfine state energies with respect to the level centroid as functions of the magnetic field. We can then add the experimentally determined centroid to centroid energy difference from [9] to obtain the total transition frequency in a magnetic field. Ignoring for the moment the diamagnetic term, the hyperfine Hamiltonian for the S states is:

$$H = ah(\vec{I} \cdot \vec{S}) + \left(-\frac{\mu_e(n)}{\hbar} \vec{S} + \frac{\mu_p}{\hbar} \vec{I} \right) \cdot \vec{B} \quad (5.1)$$

μ_e is the magnetic moment of the positron, and μ_p is that of the antiproton. \vec{S} and \vec{I} are the spins of the positron and the antiproton, respectively. The eigenvalues of (5.1) can be found analytically, resulting in the Breit-Rabi formula:

$$\mathcal{E}_{F=I \pm 1/2} = -\frac{\mathcal{E}_{HF}}{4} - \mu_p m_F B \pm \frac{\mathcal{E}_{HF}}{2} \sqrt{1 + 2m_F x + x^2} \quad (5.2)$$

$$x = \frac{B(\mu_e(n) + \mu_p)}{\mathcal{E}_{HF}} \quad (5.3)$$

, where \mathcal{E}_{HF} is the hyperfine splitting for the principal quantum number under consideration, and m_F is the total magnetic quantum number, $m_F = m_L + m_S + m_I$. In the case of $m_F = -1$, the square root contains a complete square and the $+(1-x)$ solution is taken.

We have let the positron magnetic moment carry a dependence of the primary quantum number, since it scales with the binding energy of the positron. For the S states, this dependence is [53]:

$$\mu_e(n) = \mu_e \left(1 - \frac{\alpha^2}{3n^2} \right) \quad (5.4)$$

, where μ_e is then the magnetic moment of an unbound positron, and α is the fine structure constant.

Now to add back in the diamagnetic term, $H' = \frac{\rho^2}{8m} B^2(x^2 + y^2)$, that was left out in (5.1), we get from first order perturbation theory the energy shifts:

$$\mathcal{E}_{dia,1S} = \langle 1S | H' | 1S \rangle = \frac{e^2 a_0^2}{4m} B^2 \approx 29.8 \text{ kHz } (B/1\text{T})^2$$

$$\mathcal{E}_{dia,2S} = \langle 2S | H' | 2S \rangle = \frac{7e^2 a_0^2}{2m} B^2 \approx 416.7 \text{ kHz } (B/1\text{T})^2$$

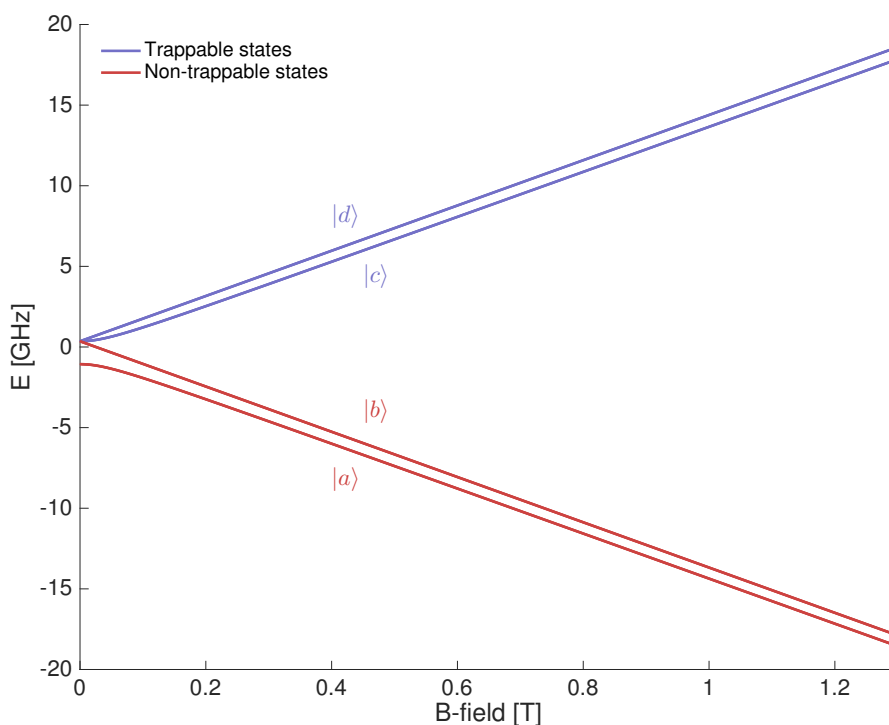


Figure 5.1: The Breit-Rabi diagram for the 1S states in (anti)hydrogen. Only the low-field seeking, diamagnetic states, $|c\rangle$ and $|d\rangle$, can be magnetically trapped. The hyperfine structure for the 2S states is qualitatively the same, but has a significantly smaller splitting a between the triplet and singlet at zero magnetic field.

In Figure 5.1, the energies of each of the hyperfine states are shown as a function of the magnetic field. We adopt the traditional naming of these states: from $|a\rangle$ to $|d\rangle$ in order of increasing energy. Only states $|c\rangle$ and $|d\rangle$ can be trapped in a magnetic minimum, so $1S_c - 2S_c$ and $1S_d - 2S_d$ are the

only transitions we need to consider. Writing these out explicitly, we have:

$$\mathcal{E}_{d-d} = \mathcal{E}_{1S2S} - \frac{\mathcal{E}_{HF}(1) - \mathcal{E}_{HF}(2)}{4} + \frac{\mu_e(2) - \mu_e(1)}{2} B + \frac{13e^2 a_0^2}{4m} B^2 \quad (5.5)$$

$$\begin{aligned} \mathcal{E}_{c-c} = & \mathcal{E}_{1S2S} + \frac{\mathcal{E}_{HF}(1) - \mathcal{E}_{HF}(2)}{4} + \frac{13e^2 a_0^2}{4m} B^2 \\ & - \frac{1}{2} \sqrt{\mathcal{E}_{HF}(1)^2 + (\mu_e(1) + \mu_p) B^2} + \frac{1}{2} \sqrt{\mathcal{E}_{HF}(2)^2 + (\mu_e(2) + \mu_p) B^2} \end{aligned} \quad (5.6)$$

2P States

To understand the behavior of the excited 2S atom, we need to include any states with energies close to that of the 2S state. The 2P states are the only candidates and we shall start by analysing their dependency on a strong magnetic field. The Hamiltonian we will consider is:

$$H = \mathcal{E}_{2P_{1/2}} + \frac{2}{3} \mathcal{E}_{FS} \left(\frac{\vec{L} \cdot \vec{S}}{\hbar^2} + 1 \right) - \frac{e\hbar}{2m} \frac{\vec{L} \cdot \vec{B}}{\hbar} - \mu_e \frac{\vec{S} \cdot \vec{B}}{\hbar} \quad (5.7)$$

, where \mathcal{E}_{FS} is the splitting between the $2P_{1/2}$ and $2P_{3/2}$ states at zero magnetic field. We have neglected the magnetic moment of the antiproton and we will also ignore a number of other effects that are much smaller than the fine structure splitting. In the $|m_l, m_s\rangle$ basis, the two maximally polarized states, $|a\rangle = |-1, -1/2\rangle$ and $|d\rangle = |1, 1/2\rangle$ are also eigenvectors of H , while the rest get mixed by the spin-orbit interaction, $\vec{L} \cdot \vec{S}$. The projection of the total angular momentum, $m_J = m_l + m_s$ is naturally conserved, so we need only simultaneously diagonalize states with the same value for m_J . The diagonal states are:

$$\begin{aligned} |2P_a\rangle &= |-1, -1/2\rangle \\ |2P_b\rangle &= |0, -1/2\rangle \cos \tau + |-1, 1/2\rangle \sin \tau \\ |2P_c\rangle &= |0, 1/2\rangle \cos \sigma + |1, -1/2\rangle \sin \sigma \\ |2P_d\rangle &= |1, 1/2\rangle \\ |2P_e\rangle &= |-1, 1/2\rangle \cos \tau - |0, -1/2\rangle \sin \tau \\ |2P_f\rangle &= |1, -1/2\rangle \cos \sigma - |0, 1/2\rangle \sin \sigma \end{aligned} \quad (5.8)$$

, where τ and σ are mixing angles. In the limit of very large B-fields, τ tends to 0, while σ tends to $\pi/2$.

Figure 5.2 on the following page shows the energies of these states as a function of the magnetic field with the corresponding states, as well as those of the 2S states:

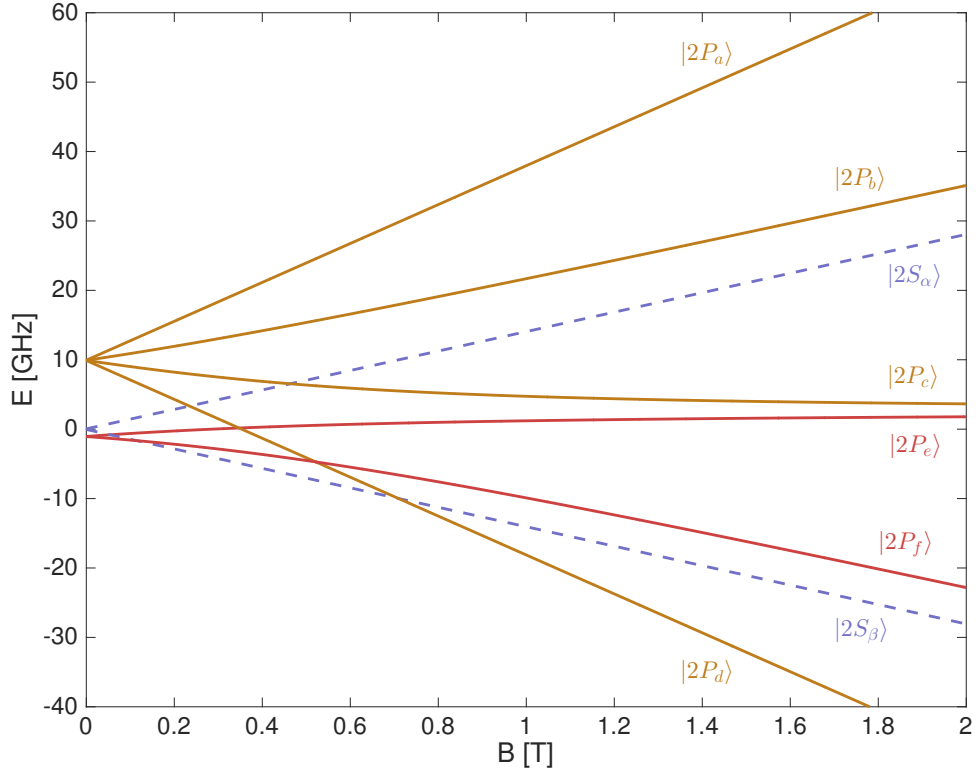


Figure 5.2: Fine structure splitting of the $n = 2$ manifold. The 2P states are named with subscripts a through f in order of *decreasing* energy at low magnetic fields. As the hyperfine structure splitting is ignored here, we label the 2S states with the subscripts α and β for low- and high-field seekers, respectively.

Mixing and Decay Rates

The 2S state of (anti)hydrogen is metastable with a natural lifetime of ~ 120 ms. In an external electric field however, the 2S state is mixed with the 2P states, allowing a single photon decay to the ground state. To see how the decay rate of the 2S state is modified in an electric field, consider first a system of a 2S state and a single 2P state and an electric interaction between them, $U = \langle 2P | -e\vec{r} \cdot \vec{E} | 2S \rangle$. With the 2S energy as zero point, we can write the Hamiltonian of the system with an electric field as:

$$H = \begin{bmatrix} 0 & U \\ U & -\mathcal{E}_p - i\hbar\gamma_p/2 \end{bmatrix} \quad (5.9)$$

Note that we have ignored the decay rate of the unmodified 2S state for now. The states modified by the electric field are the eigenstates of this matrix,

and we can find the decay rate of the modified $2S'$ state from the imaginary part of the corresponding eigenvalue. This eigenvalue is:

$$\begin{aligned}\mathcal{E}_{2S'} &= \frac{1}{2}(\mathcal{E}_P + i\hbar\gamma_P/2) \left(-1 + \sqrt{1 + \frac{4U^2}{(\mathcal{E}_P + i\hbar\gamma_P/2)^2}} \right) \\ &\approx \mathcal{E}_P \frac{U^2}{(\mathcal{E}_P^2 + \hbar^2\gamma_P^2/4)} - i\hbar\gamma_P/2 \frac{U^2}{(\mathcal{E}_P^2 + \hbar^2\gamma_P^2/4)}\end{aligned}\quad (5.10)$$

We expanded the square root for small values of the fraction inside. In particular, the electrical interaction, U remains much smaller than \mathcal{E}_P for any fields that we will consider. Note however in Figure 5.2 on the previous page, that around $B = 0.5$ T, the magnetic field introduces a degeneracy between the trappable $2S$ state and the $2P_c$ state. The decay rate at any other field is then given by the imaginary part of this energy:

$$\gamma_{2S'} = \gamma_{2P} \frac{U^2}{(\mathcal{E}_P^2 + \hbar^2\gamma_{2P}^2/4)} \quad (5.11)$$

To get the total decay rate, we naturally have to add the contributions from each of the $2P$ states. In the general case, there is the additional complication of an arbitrary angle between the electric and magnetic fields, so we choose coordinates such that $\vec{B} = (0, 0, B)$ and $\vec{E} = (E_\perp, 0, E_\parallel)$. The Hamiltonian for the electric field is therefore

$$H'_E = -e(xE_\perp + zE_\parallel) \quad (5.12)$$

with our new set of $U_i = \langle 2P_i | H'_E | 2S \rangle$, we can then write the single photon decay rate of our modified $2S'$ as:

$$\gamma_{2S'} = \gamma_{2P} \sum_i \left[\frac{U_i^2}{(\mathcal{E}_{P,i}^2 + \hbar^2\gamma_{2P}^2/4)} \right] \quad (5.13)$$

$$\approx 0.015 \text{ s}^{-1} \left(\frac{E_\parallel}{\text{V/m}} \right)^2 + 0.0055 \text{ s}^{-1} \left(\frac{E_\perp}{\text{V/m}} \right)^2 \quad (5.14)$$

, where the second line is evaluated at $B = 1$ T.

Decays with Spin-flip

Each of the $2P_i$ states can decay with a single photon to either a trappable hyperfine state ($|1S_c\rangle$ or $|1S_d\rangle$), or an untrappable one ($|1S_a\rangle$ or $|1S_b\rangle$). The probability for each is given by the amount of positron spin in the $2P_i$ state

that matches the ground state in question. For each of the $2P_i$ states, we can thus assign a probability $P_i(B)$ that this state will decay into an untrappable 1S state. It is a function of the magnetic field since the composition of pure spin states in the $2P_i$ states generally is, see equation (5.8). We can now write up the probability for a trappable 2S atom, which decays through a $2P$ state by mixing in an electric field, to result in an untrappable 1S state. This probability is simply the fraction of the spin-flipping decay rate to the total single photon decay rate:

$$\beta_{\text{spinflip}} = \frac{\gamma_{2P}}{\gamma_{2S'}} \sum_i \left[\frac{P_i U_i^2}{(\mathcal{E}_{P,i}^2 + \hbar^2 \gamma_{2P}^2 / 4)} \right] \quad (5.15)$$

In Figure 5.3 on the following page we plot this ratio for both a purely perpendicular electric field, $\vec{E} = (E_{\perp}, 0, 0)$ and a purely parallel one $\vec{E} = (0, 0, E_{\parallel})$. At low fields, it is possible to choose the direction of the electric field (parallel to \vec{B}) such that a quite high probability of decaying into untrappable states is achieved. However, as the magnetic field increases, the energy difference between spin directions increases, and these spin-flips become unlikely for any direction of the electric field.

$\vec{v} \times \vec{B}$ Decay

An atom moving in a magnetic field will experience an electric field, which will modify the lifetime of the 2S state according to (5.13). The fastest trapped atoms in ALPHA have a kinetic energy of approximately 0.5K, corresponding to a velocity of about 90m/s. Assuming this velocity is perpendicular to a 1 T magnetic field, the electric field in the frame of the atom is

$$|E| = \left| \vec{v} \times \vec{B} \right| = 90 \text{ V m}^{-1}$$

In this case, the decay rate from (5.13), using a purely perpendicular E-field, is $\gamma_{2S'} = 44 \text{ s}^{-1}$. This adds to the two-photon decay rate of 8.2 s^{-1} , which stays practically unaltered by the perturbing electric field. The value of 90 V m^{-1} chosen here is close to the maximum possible for an atom in the ALPHA trap. Simulating the trapped atom trajectories in more detail as described below, gives an average decay rate induced by the motional electric field of 11.5 s^{-1} .

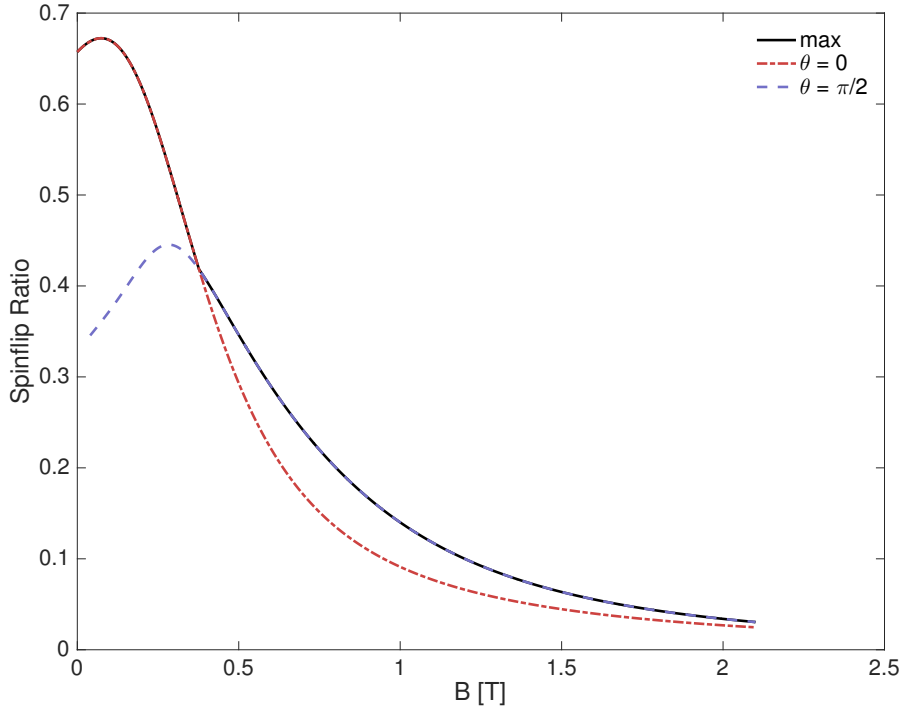


Figure 5.3: Ratio of spinflip-inducing single photon 2S as function of the magnetic field. Plotted for both $\vec{E} \perp \vec{B}$ ($\theta = \pi/2$) and $\vec{E} \parallel \vec{B}$ ($\theta = 0$). As the magnetic field increases, the states become increasingly spin-polarized, and the probability for changing the spin in a decay decreases for any relative direction of \vec{B} and \vec{E} .

5.2 1S-2S Excitation

We now turn to deriving the equations that govern the two photon excitation from the 1S to the 2S state. We will need to make some assumptions of experimental conditions, and will base all of these on the situation in ALPHA. Firstly, the designed beam waist of approximately $200 \mu\text{m}$ means the Rayleigh range, $z_R = \pi w_0^2 / \lambda$, is much larger than the region containing the trapped $\bar{\text{H}}$. Thus, we can ignore the Gouy phase as well as the change in the laser waist with position.

Secondly, we will assume a monochromatic laser beam. This assumption is good if the laser width is small compared to the inverse of the interaction time, which is the case for ALPHA. Thus, the standing wave electric field we consider is:

$$\vec{E} = \hat{x} E_0 e^{-r^2/w^2} \cos(kz + \delta) \cos(\omega_L t) \quad (5.16)$$

, where $r^2 = x^2 + y^2$, w is the beam waist, δ is a phase shift which has no effect on the calculation, E_0 is the maximum electric field, and $\omega_L/(2\pi)$ is the laser frequency. Thinking of the standing wave as a superposition of light moving in the $+z$ direction and in the $-z$ direction, the intensity of light in *one* of the beams is $I = c\epsilon_0 E_0^2/8$. For a Gaussian beam, $I = 2P_0/(\pi w^2)$ where P_0 is the total power in one beam.

The two photon excitation of the 2S state occurs by a virtual excitation through the nP states. Because the one photon absorption is far off resonance from any P state, the infinite number of P states can be adiabatically eliminated from the equations. We will write the wave function as

$$|\Psi(t)\rangle = |\psi_{1S}\rangle e^{-i\mathcal{E}_{1S}t/\hbar} C_{1S}(t) + \sum_n |\psi_{nP}\rangle e^{-i\mathcal{E}_{nP}t/\hbar} C_{nP}(t) \quad (5.17)$$

$$+ |\psi_{2S}\rangle e^{-i\mathcal{E}_{2S}t/\hbar} C_{2S}(t) \quad (5.18)$$

, where the C s are slowly varying coefficients and the sum over n is understood to also include the continuum states. Substituting into the Schrödinger equation gives:

$$i\hbar \frac{dC_{1S}}{dt} = eE_x(\vec{r}(t), t) \sum_n D_{1S,nP} e^{-i(\mathcal{E}_{nP} - \mathcal{E}_{1S})t/\hbar} C_{nP} \quad (5.19)$$

$$i\hbar \frac{dC_{nP}}{dt} = eE_x(\vec{r}(t), t) \left[D_{nP,1S} e^{-i(\mathcal{E}_{1S} - \mathcal{E}_{nP})t/\hbar} C_{1S} + D_{nP,2S} e^{-i(\mathcal{E}_{2S} - \mathcal{E}_{nP})t/\hbar} C_{2S} \right]$$

$$i\hbar \frac{dC_{2S}}{dt} = eE_x(\vec{r}(t), t) \sum_n D_{2S,nP} e^{-i(\mathcal{E}_{nP} - \mathcal{E}_{2S})t/\hbar} C_{nP}$$

where the electric field is from (5.16).

These are fairly complicated equations so we will perform some simplifications based on the situation we're modeling. First, we are interested in the two photon absorption from a laser beam that is weak on the scale of the atomic parameters. This means the counter-rotating terms in the electric field can be dropped. Second, the time dependence in the electric field due to the changing position of the \vec{H} can *not* be dropped; the time dependence of z gives the Doppler shift and the time dependence in x, y gives the rise and fall of the intensity. However, because the line width of the transition is so narrow, the $\exp[ikz(t)]$ in going from the 1S to the P states must be matched with the $\exp[-ikz(t)]$ when going from the P to the 2S state, otherwise the transition will be Doppler shifted out of resonance.

The middle equation can be approximately solved by integrating both sides with respect to t and using the fact that the C_{nS} are slowly varying:

$$C_{nP} \simeq -\frac{E_0}{2} e^{-r^2(t)/w^2} \cos(kz(t)) \left[\frac{D_{nP,1S}}{\mathcal{E}_{nP} - \mathcal{E}_{1S} - \hbar\omega_L} e^{i(\mathcal{E}_{nP} - \mathcal{E}_{1S} - \hbar\omega_L)t/\hbar} C_{1S} \right. \\ \left. + \frac{D_{nP,2S}}{\mathcal{E}_{nP} - \mathcal{E}_{2S} + \hbar\omega_L} e^{i(\mathcal{E}_{nP} - \mathcal{E}_{2S} + \hbar\omega_L)t/\hbar} C_{2S} \right] \quad (5.20)$$

As described in the previous paragraph, when this form is substituted into the equations for the C_{nS} , the terms that lead to $\exp[\pm 2ikz(t)]$ are dropped because the Doppler shift makes them non-resonant. The AC Stark shift is described separately in Section 5.3 on page 56, so here we will drop those terms. This means ignoring term with C_{1S} in the dC_{1S}/dt equation and similarly for the 2S state. This leads to the equations that couple the 1S and 2S states:

$$i\hbar \frac{dC_{1S}}{dt} = \xi E_0^2 e^{-2r^2(t)/w^2} e^{-i(\mathcal{E}_{2S} - \mathcal{E}_{1S} - 2\hbar\omega_L)t/\hbar} C_{2S} \quad (5.21)$$

$$i\hbar \frac{dC_{2S}}{dt} = \xi E_0^2 e^{-2r^2(t)/w^2} e^{i(\mathcal{E}_{2S} - \mathcal{E}_{1S} - 2\hbar\omega_L)t/\hbar} C_{1S} \quad (5.22)$$

The parameter ξ is defined as

$$\xi = -\frac{e^2}{8} \sum_n \frac{D_{2S,nP} D_{nP,1S}}{\mathcal{E}_{nP} - \mathcal{E}_{1S} - \hbar\omega_L} \simeq 12.3 \varepsilon_0 a_0^3 \quad (5.23)$$

, where a_0 is the Bohr radius and e is the electric charge. The numerical value was obtained by performing the sum using states confined within a sphere of radius $30 a_0$.

Perturbative Calculation

From (5.22), we can obtain a simple expression for the excitation probability in a single pass of the laser, by assuming that this probability is small and set $C_{1S} = 1$. This leaves us with a single, uncoupled equation for C_{2S} that we can integrate over the traversal of the laser beam. We choose to have the laser axis coincide with the z -axis, and define the detuning, $\Delta\omega = (\mathcal{E}_{2S} - \mathcal{E}_{1S} - 2\hbar\omega_L)/\hbar$, as well as the perpendicular velocity, $v_\perp^2 = v_x^2 + v_y^2$. We let the closest approach to the axis happen at $t = 0$ and call this distance b , so $r^2(t) = b^2 + v_\perp^2 t^2$. We can now write the coefficient of the 2S state as:

$$C_{2S} = \frac{\xi}{i\hbar} E_0^2 e^{-2b^2/w^2} \int_{-\infty}^{\infty} e^{-2v_\perp^2 t^2/w^2} e^{i\Delta\omega t} dt \quad (5.24)$$

$$= \frac{\xi}{i\hbar} E_0^2 e^{-2b^2/w^2} \frac{w}{v_\perp} \sqrt{\frac{\pi}{2}} e^{-\frac{\Delta\omega^2 w^2}{8v_\perp^2}} \quad (5.25)$$

For the excited population, we recast the laser parameters in terms of more directly measurable quantities: the laser frequency, f , the resonant frequency for the two-photon transition, $f_0 = (\mathcal{E}_{2S} - \mathcal{E}_{1S})/2h$, and the maximum intensity in the single direction laser beam, I .

$$|C_{2S}|^2 \simeq 32\pi I^2 \frac{12.3^2 a_0^6}{\hbar^2 c^2} \frac{w^2}{v_\perp^2} e^{-4b^2/w^2} e^{-(f-f_0)(2\pi w/v_\perp)^2} \quad (5.26)$$

Suppose now that the laser frequency is different for each crossing of the laser beam, emulating the case of some laser line width with a characteristic time scale longer than a single crossing. Taking the frequencies for each pass from a Gaussian distribution with a FWHM of δf_{las} around the central f_{las} , we get the average excitation:

$$\langle |C_{2S}|^2 \rangle = \frac{\sqrt{8\ln 2}}{\sqrt{\pi} \delta f_{\text{las}}} \int_{-\infty}^{\infty} |C_{2S}|^2(f) e^{-8\ln 2(f-f_{\text{las}})^2/\delta f_{\text{las}}^2} df \quad (5.27)$$

$$= \frac{16I^2}{\delta f} \frac{12.3^2 a_0^6}{\hbar^2 c^2} \frac{w}{v_\perp} e^{-4b^2/w^2} e^{-(f_0-f_{\text{las}})/\delta f^2} \quad (5.28)$$

, where we have now introduced $\delta f^2 = (\frac{v_\perp}{2\pi w})^2 + \frac{\delta f_{\text{las}}^2}{8\ln 2}$, which is simply the laser width and the transit time width added in quadrature.

Thus, in (5.28) we have arrived at the excitation probability in a single pass, incorporating both the dominating broadening mechanism and the laser linewidth, in a single perturbative expression.

Density Matrix Formalism

Above, we made the perturbative assumption that the population in the ground state does not change in a single pass of the laser beam. Although this is a reasonable assumption for realistic experimental parameters, we want to accurately capture the dynamics of the excitation, so we turn to the density matrix formulation, in which the time evolution of the density operator, ρ , is described by the von Neumann equation:

$$\dot{\rho} = -\frac{i}{\hbar} (H\rho - \rho H) \quad (5.29)$$

We consider the 4 states: $|1\rangle$ is the low field seeking 1S state, in which we initially place the entire population. $|2\rangle$ is the high field seeking 1S state, which can be produced in decays from 2S states, and is unconfined by the magnetic trap. $|3\rangle$ is the photo-ionised state with the positron dissociated from

the antiproton. We will neglect the possibility of direct 3-photon ionisation of the 1S state. Finally, $|4\rangle$ is the low field seeking 2S state, with the laser interaction coupling states $|1\rangle$ and $|4\rangle$.

We explicitly introduce decay rates for the relevant channels out of the 2S state. Γ_{41} includes both the two photon decays, which conserve the hyperfine state, as well as the fraction of single photon decays induced by mixing with 2P states which do not alter the spin direction of the positron. The single photon decays that flip the positron spin constitute Γ_{42} . We calculated the single photon decay rate as well as the spin-flip ratio in these decays in equations (5.13) and (5.15), including their dependence on the electric and magnetic fields. Γ_{43} is the rate of photo-ionisation by 243 nm photons, which depends on the local light intensity provided by those photons:

$$\Gamma_{43} = 7.57 \text{ s}^{-1} \frac{I}{\text{W/cm}^2} \quad (5.30)$$

Assembling this into the density matrix formalism, we can write out all the non-zero entries of $\dot{\rho}$

$$\begin{aligned} \dot{\rho}_{11} &= -\frac{i}{2}\Omega_{14}(t)(\rho_{41} - \rho_{14}) + \Gamma_{41}\rho_{44} \\ \dot{\rho}_{22} &= \Gamma_{42}\rho_{44} \\ \dot{\rho}_{33} &= \Gamma_{43}\rho_{44} \\ \dot{\rho}_{44} &= -\frac{i}{2}\Omega_{14}(t)(\rho_{14} - \rho_{41}) - \Gamma\rho_{44} \\ \dot{\rho}_{14} &= -\frac{i}{2}\Omega_{14}(t)(\rho_{44} - \rho_{11}) + \left(-i\Delta - \frac{1}{2}\Gamma\right)\rho_{14} \\ \dot{\rho}_{41} &= -\frac{i}{2}\Omega_{14}(t)(\rho_{11} - \rho_{44}) + \left(i\Delta - \frac{1}{2}\Gamma\right)\rho_{41} \end{aligned} \quad (5.31)$$

, where the equivalent of the Rabi frequency for the two-photon transition is once again derived from (5.22).

$$\Omega_{14}(t) = 12.3 a_0^3 \frac{16I}{\hbar c} e^{-2r(t)^2/w^2} \quad (5.32)$$

, and we defined $\Gamma \equiv \Gamma_{41} + \Gamma_{42} + \Gamma_{43}$. The detuning, Δ , here is defined as the amount that the 2 photons fall short of the transition energy, $\Delta = 2\omega_{\text{las}} - (\mathcal{E}_4 - \mathcal{E}_1)$.

In Figure 5.4 on the following page we compare the excitation rates of the

perturbative expression in (5.28) and that obtained by numerically integrating the equations (5.31) over a similar crossing of the laser beam. For small laser powers or for large impact parameters, the perturbative error as well as the ionisation probability, which the expression in (5.28) does not account for, are both negligible, which means that in numerical simulations like the ones described in Section 5.4 on page 59, computation time can be saved by only integrating the full set of equations when the maximum intensity seen in a crossing of the laser beam is high.

We are calculating the transition probabilities for laser powers that are

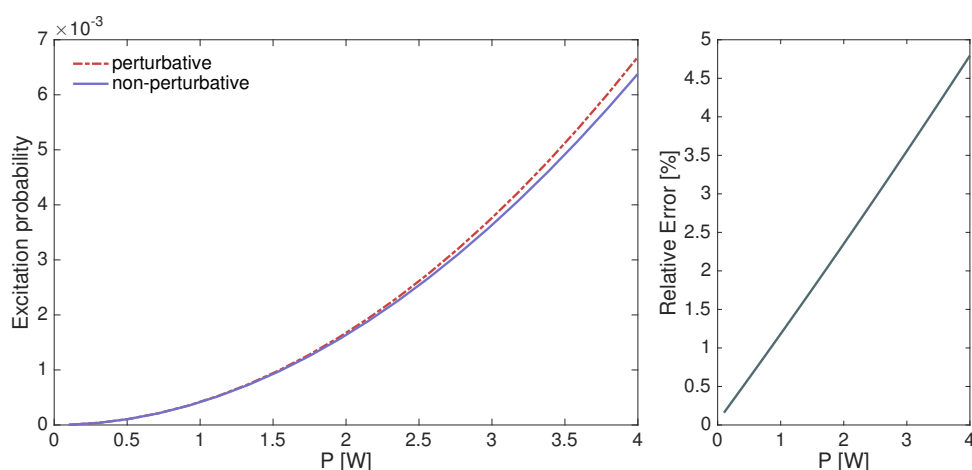


Figure 5.4: Left: Excitation probability in a single pass of the laser beam for both the perturbative (5.28) and the non-perturbative (5.31) methods. Assumed is a $200 \mu\text{m}$ beam waist and a perpendicular velocity of $v_{\perp} = 90 \text{ m/s}$. Right: The relative difference between the two methods.

higher than what have been used in notable 1S-2S spectroscopy experiments in hydrogen like those listed in Table 5.1 on the following page. The main difference between these regular hydrogen experiments and ALPHA, which drives the need for high laser power is the number of atoms addressed. While a strong signal can be achieved by exciting a very small fraction of 10^{10} atoms, a single trapped antihydrogen atom must become excited with a high probability for any experiment to be feasible.

It is worth pointing out this stage that a circulating power of 2W as frequently assumed in this chapter and the next is well within the capacity for build-up in the enhancement cavity as described in Section 2.4 on page 21. For the

most precise 1S-2S measurements achieved in hydrogen [9], there is little incentive to increase the laser intensity, as doing so would increase the size of the AC stark shift, which is a major systematic effect in those experiments.

Table 5.1: Laser parameters in a select few 1S-2S spectroscopic measurements in hydrogen. In [9] an enhancement cavity is used to build up laser power, while in [54] a single reflection of the 243nm beam provides the counter-propagating photons. The number of atoms, N_{H} , quoted for [54] is a trapped and cooled sample, while for [9], where a hydrogen beam is used, we list the flux of atomic hydrogen from the cryogenic nozzle [55]. The intensities listed here are representative for their respective experiments, but as discussed in Section 5.3, the laser intensity can be intentionally varied to compensate for the AC stark shift.

	w_0	P	I_0	N_{H}
Parthey et al. 2011 [9]	$292 \mu\text{m}$	300mW	$2.24 \times 10^6 \text{W/m}^2$	$\sim 10^{16} \text{s}^{-1}$
Cesar et al. 1996 [54]	$37 \mu\text{m}$	4mW	$4.65 \times 10^8 \text{W/m}^2$	$10^{10} - 10^{13}$

5.3 Shifts and Broadening Effects

In this section we review the broadening effects and shifts relevant for initially detecting a 1S-2S excitation signal in ALPHA and for determination of the transition frequency to within a few kHz. We leave out well known effects like the second order Doppler shift, which enters only below this level for foreseen experimental parameters. A summary of the effects treated and their inclusion in our simulations of the experiment at the current stage is given in Table 5.2 on page 60.

Transition Time Broadening

The dominating broadening effect for our current experimental parameters is due to the limited interaction time between the laser beam and an atom passing through it. The uncertainty in laser frequency as seen by the atom moving is inversely proportional to the time it takes to pass through the laser beam. The FWHM of this broadening is:

$$\Delta f_{\text{Transit}} = \sqrt{\ln(2)} \frac{v_{\perp}}{\pi w_0} \quad (5.33)$$

Since the transition of interest must be driven by two photons with this frequency width, the resulting width in terms of the full transition frequency is twice this expression. For our example parameters, $v_{\perp} = 90 \text{ m/s}$ and $w_0 = 196 \mu\text{m}$, the resulting broadening of the transition is $\sim 240 \text{ kHz}$.

Transit time broadening is also inherent in experiments on atomic beams, where the interaction time is necessarily limited. It can be reduced greatly in magnetically trapped samples as demonstrated in [54]. It is worth noting though, that this requires a much colder sample of antihydrogen and a tighter magnetic minimum trap than what has been achieved so far, such that the atoms can be contained almost entirely within the laser beam.

DC Stark Effect

An external electric field causes mixing between the S- and P- states in (anti)hydrogen which as we saw above modifies the decay rate of the 2S state. The same mixing leads to an energy shift of both the 1S and 2S states, which we will treat here. As the trapped atoms will experience a range of electric field strengths from the motional, $\vec{v} \times \vec{B}$ field, the transition is broadened as well as shifted.

The energy shift of the S states is calculated in second order perturbation theory, summing contributions from the P-states. For the 1S state, no P-states are near enough that a 1T magnetic field significantly alters any energy difference, so we can use the zero-field polarizability:

$$\alpha_{1S} = 4\pi\epsilon_0 \frac{9}{2} a_0^3 \quad (5.34)$$

, which leads to the energy shift:

$$\Delta\mathcal{E}_{1S} = -\frac{1}{2}\alpha_{1S}E^2 \approx -5.6 \times 10^{-8} \text{ Hz} \left(\frac{E}{\text{V/m}}\right)^2 h \quad (5.35)$$

For the 2S state, the shift is dominated by contributions from the nearby 2P states. It is clear from Figure 5.2 on page 47 that the magnetic perturbation is significant on this scale, and we must use the states (5.8). Very similarly to our calculation of the modified decay rate of the 2S state due to the electric field, the most general case features an arbitrary angle between the electric and magnetic fields. Thus, we use the same perturbing Hamiltonian as in (5.12), $H'_E = -e(xE_{\perp} + zE_{\parallel})$.

The second order perturbation is then:

$$\Delta\mathcal{E}_{2S} = \sum_k \frac{|\langle k|H'_E|2S\rangle|^2}{\mathcal{E}_{2S} - \mathcal{E}_k} \quad (5.36)$$

$$\approx -0.17\text{Hz} \left(\frac{E_{\parallel}}{\text{V/m}}\right)^2 h + 0.041\text{Hz} \left(\frac{E_{\perp}}{\text{V/m}}\right)^2 h \quad (5.37)$$

, where we summed over just the 2P states at $B = 1\text{ T}$ to get the approximate numbers in the second line. This is a good approximation due to the much larger energy difference to any other P states.

Assuming as previously a 90 m/s velocity perpendicular to the magnetic field the shift of the 1S-2S transition frequency induced by the DC Stark effect from the motional electric field is then $\sim 300\text{Hz}$. At the current level of accuracy, we can thus safely ignore this.

AC stark Effect

The oscillating electric field of the laser also introduces a shift of both the 1S- and the 2S- state. This was explicitly left out in Section 5.2 on page 50, and we re-introduce this shift at this stage. We arrive at a value for the shift of the total transition frequency (taking the real part of the 2S shift), which coincides with the thorough treatment in [56]:

$$\Delta f_{AC} = 1.67\text{Hz} \frac{I}{\text{W/cm}^2} \quad (5.38)$$

With the power P in each of the counter-propagating beams, the central intensity which takes into account the standing wave pattern, is

$$I_0 = \frac{4P}{\pi w_0^2} \quad (5.39)$$

Thus, for an expected laser power of $P = 2\text{W}$, the AC stark shift in the middle of the laser beam is $\Delta f_{AC} \approx 10\text{kHz}$. This is insignificant for detecting the first excitations in antihydrogen, but will be relevant for a more precise determination of the transition frequency.

The AC stark shift can be compensated for by measuring the line center at several laser intensities. The transition frequency at zero laser intensity can then be found through extrapolation. This is very likely to be necessary for

eventually making spectroscopic measurements of antihydrogen competitive with the precision of those in hydrogen, and this effort will clearly need a higher rate of data taking than what is currently achieved.

Residual Zeeman Effect

In (5.6) and (5.6), we calculated the 1S-2S transition energies for both the trappable hyperfine states as functions of magnetic field. The frequency shift with magnetic field is thus given quite trivially by these equations. Taking only a linear expansion around $B = 1$ T, we get:

$$\Delta f_{Z,d-d} \approx 96 \text{ Hz/Gauss} \quad (5.40)$$

$$\Delta f_{Z,c-c} \approx 1.9 \text{ kHz/Gauss} \quad (5.41)$$

We call this the residual Zeeman effect as the Zeeman shifts of the initial and excited states are nearly identical, leading to a near cancellation of the Zeeman effect in the transition energy. The exact lineshape resulting from these shifts depends on the details of the atomic orbits in the magnetic trap, and we will discuss this the residual Zeeman effect a bit further in the context of simulating the atomic orbits in the ALPHA trap.

Lifetime Broadening

The natural linewidth of an atomic transition is simply the inverse of the lifetime of the excited state, and reductions in this lifetime increase the linewidth similarly. We have already calculated the decay rate introduced by the motional electric field, which leads to a negligible broadening. The largest decrease of the 2S lifetime possible in the trap comes from the ionisation rate in the laser beam, given in Equation (5.30). This leads to a position dependent broadening of the linewidth with a FWHM in the center of the beam, assuming the same laser parameters as above of:

$$\Delta f_{ion} = \frac{\Gamma_{43}(P = 2\text{W})}{2\pi} \approx 8 \text{ kHz} \quad (5.42)$$

5.4 Numerical Simulation

The total rate of excitation at any given laser frequency depends on the dynamics of the magnetically trapped atoms. Furthermore, any precision mea-

Table 5.2: Broadening effects and shifts and their approximate size. Assuming 2W of circulating 243 nm light in a 200 μm waist, and atoms moving perpendicular to the laser beam at 90m/s. We list the size of effect on the total transition frequency rather than in terms of the the frequency of the 243 nm laser that drives it.

Effect	Approximate Size	Included in Simulation
1st order Doppler	cancels	no
2nd order Doppler	220Hz	no
Transition time	240kHz	yes
AC Stark	10kHz	no
DC Stark	0.3kHz	no
Residual Zeeman d-d (c-c)	96Hz/G (1.9kHz/G)	yes
Ionisation width	8kHz	yes

surement will rely on comparing the measured response to a detailed model of the line shape. A full simulation of the laser interaction including realistic atom trajectories is therefore needed, and we will here briefly describe how we have implemented this.

The ALPHA trap is much larger than the de Broglie wavelength of the trapped atoms, allowing us to model the atoms as classical particles moving in a potential defined by $U = -\vec{\mu} \cdot \vec{B}$, where $\vec{\mu}$ is the magnetic moment of the $\bar{\text{H}}$. Since the spin precession frequency of the positron is also much higher than any of the motional frequencies, this is further simplified and we have for a trapped atom: $U = \mu B$. Since we require a long simulation time compared to the motion of the atoms, we use a fourth order symplectic integrator [57, 58, 59], which has the advantage of maintaining the total mechanical energy for long simulation times. This part of the simulation code has also been used for other studies of trapped antihydrogen in ALPHA like [46], and has been described in that context. The simulations used in the measurements presented in Chapters 3 and 4 use a similar but independent code to propagate the atoms in the magnetic field, and the performance of these independently written codes have been checked against each other.

The initial conditions of the simulation mimic those of the $\bar{\text{H}}$ atoms in ALPHA: They are launched from within an ellipsoid the size of the positron plasma that antiprotons are injected into, and given random velocities taken from a high temperature thermal distribution, matching the energy distribution found consistent with the annihilation data in Figure 2.6 on page 16. The

atoms are initially in a high ($n = 25$) Rydberg state, which is roughly the highest n that stays bound in the electric fields present [60]. We then allow the atoms to decay to the ground state during the first couple of seconds of the simulation, updating their magnetic moment appropriately. The laser is then turned on and the atoms still confined at this time form our trapped ensemble.

Anytime an \bar{H} comes close to the laser beam, the code chooses to either evaluate the perturbative expression (5.28) in the case where the maximum intensity for the crossing is low, or solve the optical Bloch equations (5.31) along the path of the atom, in the high intensity case. While far from the laser, the 2S population is still allowed to decay to 1S, either with two photons, or through mixing with 2P states caused by the motional electric field as described in (5.13). The code stops if one of 3 conditions are met: 1) the \bar{H} hits the wall. This can happen either because the atom is in a high-field seeking state after going through a spin-flipping decay, or, in rare cases, atoms launched with slightly higher energy than the minimum well depth can take a while to find the shallowest point in the trap and escape. We refer to these latter atoms as ballistically lost. 2) If the atom is ionised by absorbing a photon while in the 2S state. 3) If the designated illumination time has passed. In all cases, the position and internal state of the atom is recorded at the time of stopping the simulation.

Detection Rates

Figure 5.5 on the following page shows the output of such a simulation, using feasible parameters for the current ALPHA experiment: $P = 2W$, $w_0 = 200\mu m$, and a flattened magnetic field. The laser frequency is chosen to be on resonance in the center of the magnetic trap. We plot the total response to illuminating both the c-c and the d-d transitions for the time T , assuming the initial trapped population is evenly distributed between $|1S_c\rangle$ and $|1S_d\rangle$. Thus after driving each transition for 250s, approximately 70% of the trapped atoms have been ionised.

As we will come back to in Chapter 6, the antiprotons resulting from the photo-ionisation of atoms in the 2S state can be directly detected to provide the signal that a 1S-2S transition has been driven. The detection can be made either by trapping the antiprotons and subsequently dumping them onto a sufficiently sensitive detector, or by reconstruction of the annihila-

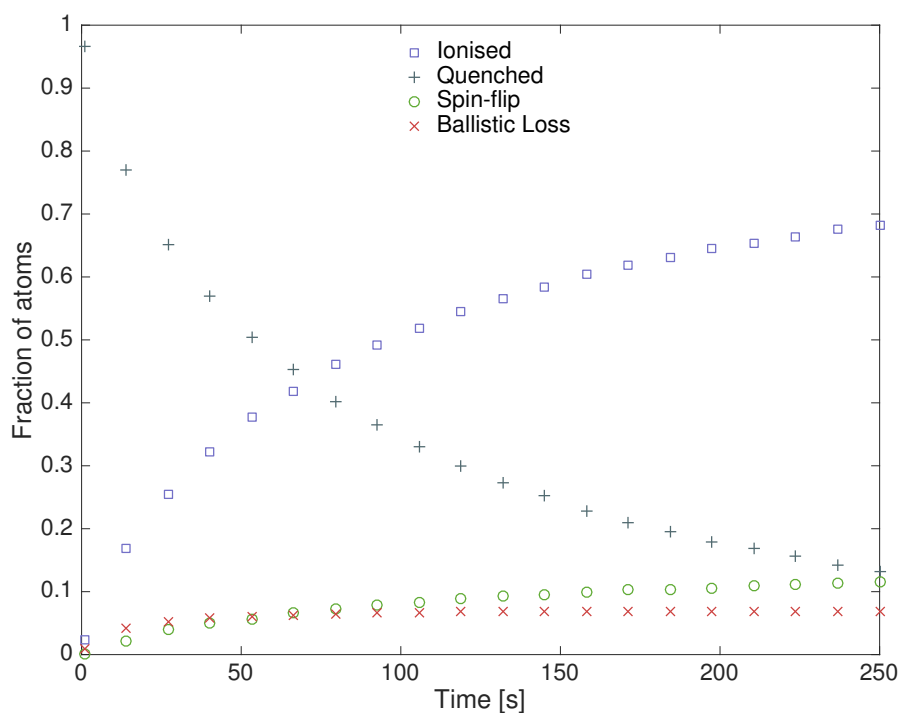


Figure 5.5: Fraction of atoms in various end states as a function of illumination time. Assumes 2W of resonant laser light in a flattened magnetic field configuration. The red triangles labeled "Ballistic Loss" denote atoms that hit the wall despite being in a low magnetic field seeking ground state. These are all so-called "quasi-trapped" atoms with higher energy than the well depth of the magnetic trap, and they escape as soon as their orbits probe a position in the trap where the confining potential is low enough.

tion products from an intentional annihilation of the antiprotons. In ALPHA, antiprotons can be made to annihilate within the Silicon Vertex Detector by using one of the five mirror coils to cancel the background 1T field, thus fanning out the field lines to go through the vacuum chamber walls. This can be done while simultaneously maintaining a magnetic minimum trap with the remaining four mirror coils.

Alternatively, the photo-ionisation of antihydrogen atoms and ejection of the produced antiprotons can provide a signal of excitation through the decrease in surviving atoms at the time of shutting down the magnetic trap. This kind of disappearance mode detection was used before in ALPHA for [19]. While this method benefits from needing no dedicated detectors for 2S

atoms, it does necessitate addressing both the c-c and the d-d transitions in order to bring down the signal to noise ratio in such a subtractive measurement. In Figure 5.8 on page 66 we compare the signals in such a disappearance measurement from simulations in two different magnetic fields. From this, the benefit of making the magnetic trap as uniform as possible is clear, and the effect can be understood as increasing the volume of the trap where the laser is on resonance with the transition.

Line Shape

In Figure 5.6 on the following page, we plot the outcome of many simulations with different laser detunings, resulting in the line shape for the chosen parameters. Here we have plotted separately the ionisation signal for a pure $|1S_d\rangle$ population and a pure $|1S_c\rangle$ one. The difference between the two stems from the stronger Zeeman detuning of the c-c transition, making it less likely to be on resonance for any given pass of the laser. This effect is minimized by the choice of magnetic field simulated here, as the central part of the trap has been made as uniform as possible. In Figure 5.7 on page 65, on the other hand, a less uniform magnetic field has been simulated and shows both a larger difference between the ionisation rates from the two different hyperfine states, but also an overall smaller response on resonance, owing to the relative decrease in the volume of the trap where the resonance condition is met.

Note that the lineshapes are asymmetric with a tail extending to higher frequencies. This is because we tune the laser to be on resonance in the center of the magnetic minimum trap, meaning that atoms can experience higher magnetic fields than where the resonance condition is met, but not lower fields. The fact that the residual Zeeman effect shifts both transitions to higher frequencies for higher magnetic fields then results in this tail being above the resonance frequency, rather than below.

Figure 5.8 illustrates from the point of view of a disappearance measurement scheme, the impact of magnetic field uniformity. Comparing the field configurations used for Figures 5.6 and 5.7, we plot the fraction of surviving atoms after 250s of illuminating each of the transitions, normalized to the surviving fraction at infinite detuning, thus obtaining the disappearance of survivors than one would measure in a disappearance mode measurement.

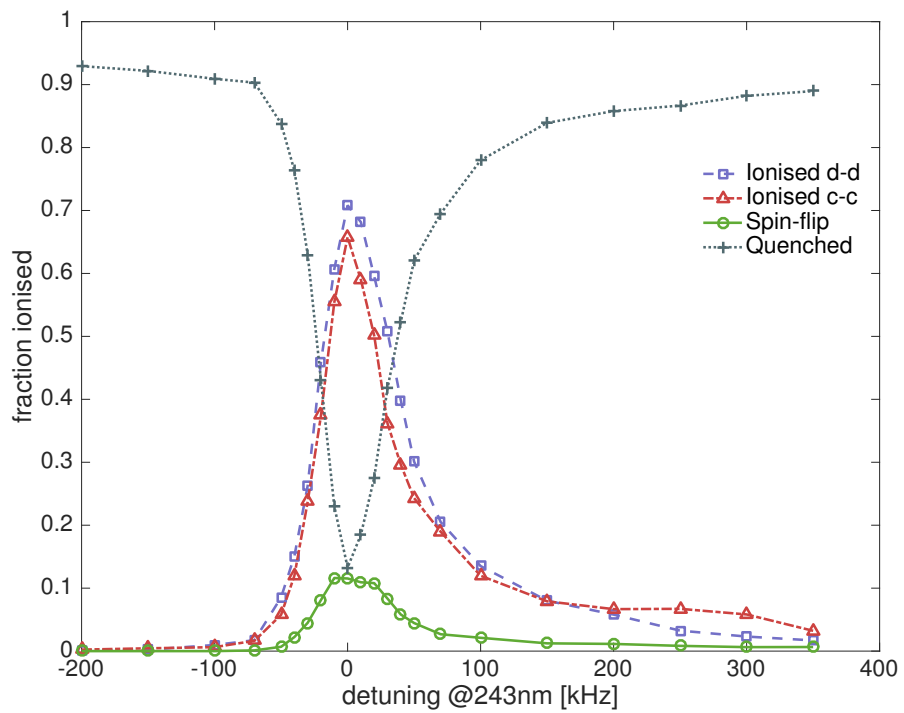


Figure 5.6: Fraction of simulated atoms respectively ionised, ejected through a spin-flip, and surviving the full illumination time as a function of the detuning of the 243 nm laser. Assuming a flattened B-field, 2W of laser power and 250s illumination of each transition.

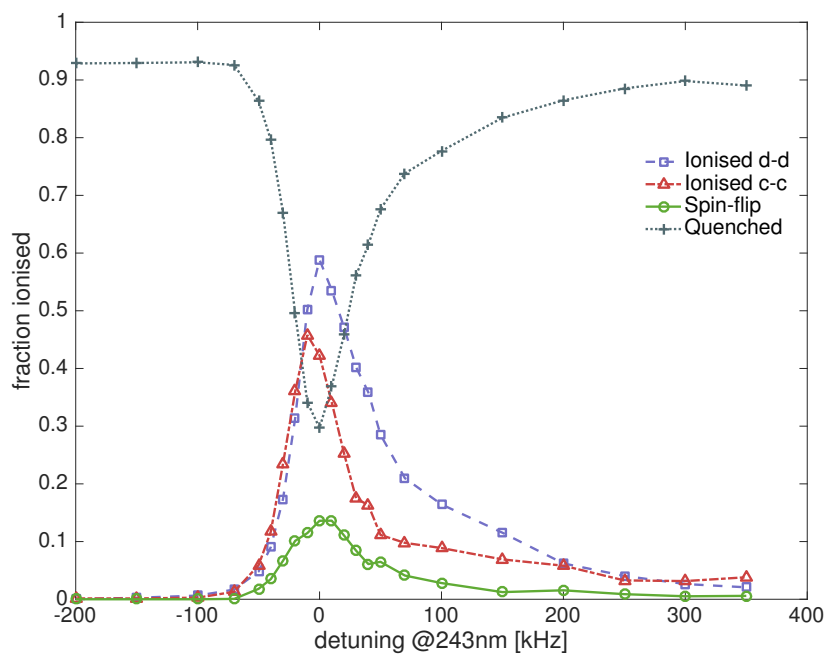


Figure 5.7: Fraction of simulated atoms respectively ionised, ejected through a spin-flip, and surviving the full illumination time as a function of the detuning of the 243nm laser. Assuming 2W of laser power and 250s illumination of each transition, as well as the "bucked" magnetic field shown in Figure 2.3 on page 12, in which one of the mirror coils is used to cancel the external solenoid field. This is the magnetic field used for the experiments described in Chapter 7.

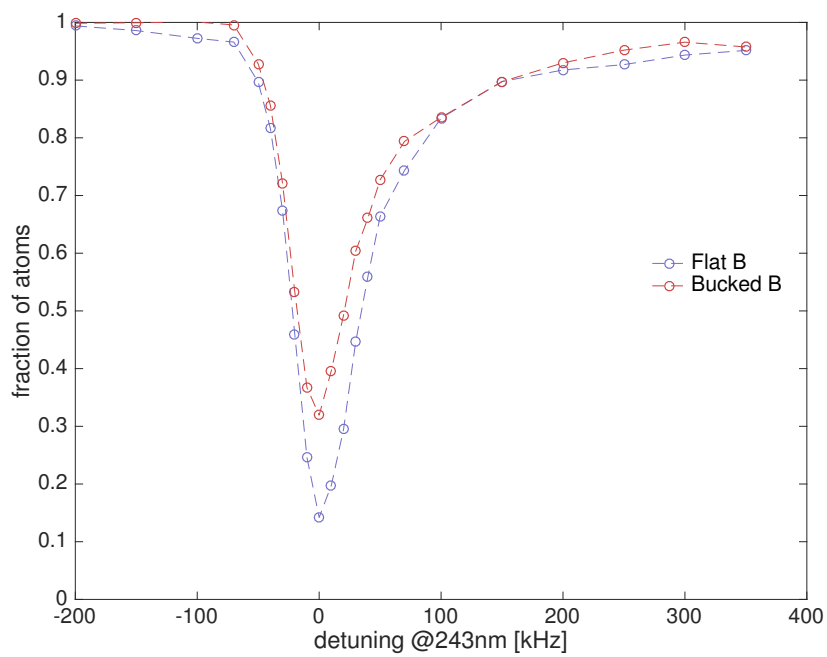


Figure 5.8: Fraction of atoms remaining in the Quench window after 250s of illumination as a function of detuning for two different field configurations. These are normalized to the number of surviving atoms at infinite detuning (chosen as -200 kHz here) to correctly emulate the signal obtained in a disappearance mode experiment.

Chapter 6

2S Detection Schemes

We have already hinted at a few ways in which excitations of 2S atoms in a 1S-2S spectroscopy experiment might be detected. In this chapter, we will more carefully go through 4 such schemes and review in the context of the current number of trapped antihydrogen atoms in ALPHA as well as practical experimental constraints, the merits of each.

6.1 Lyman- α Photons

As we have seen in Section 5.1 on page 43, the 2S state of (anti)hydrogen can be made to decay to the 1S state essentially instantly by applying an electric field. As this rapid decay happens through the 2P states, a single photon is emitted with the full 1S-2S energy difference. Detecting this Lyman- α photon is the basis of detecting 1S-2S excitations in typical experiments with ordinary hydrogen [9, 61]. When not limited by solid angle, Lyman- α photons can be detected with high efficiency, and the difference in wavelength from the light needed to excite the transition enables good discrimination of stray 243nm photons stemming from the excitation laser or indeed from two-photon decays of the 2S atoms.

In experiments where antihydrogen is excited in a beam, the long lifetime of the metastable 2S state allows for complete separation of excitation and detection regions, which means a very good solid angle coverage for the Lyman- α detection can be achieved.

As described in Chapter 2, the ALPHA magnetic minimum trap is superim-

posed on the Penning-Malmberg trap needed for producing cold antihydrogen. This severely limits the solid angle available for detecting photons from the trapped atoms. This exacerbates what is currently the primary constraint on antihydrogen experiments compared to ordinary hydrogen, which is the limited number of atoms available. Assuming realistic laser parameters for ALPHA and a single atom trapped at a time, the mean time between excitations and therefore possible Lyman- α photon emissions is of order ~ 100 s. Without a significant increase in this rate, it would be a tall order to achieve a signal higher than the background of dark counts in single photon detectors.

6.2 Spin-flip Ejection

In addition to the emission of a Lyman- α photon, making the 2S state decay through the mixing with 2P states allows for decays that change the hyperfine state. Some such decays will therefore result in a spin-flip, with the produced high field seeking atom being promptly ejected from the magnetic minimum trap and annihilating. These annihilations are detected in ALPHA with $\sim 60\%$ efficiency, much better than what is allowed from solid angle considerations of Lyman- α photon detection in any minor modification to the current experimental setup.

An important parameter for the efficiency of using these annihilations as the detection method for 2S atoms is the fraction of electric field induced decays that result in a spin-flip, which we calculated for Figure 5.3 on page 50 for both electric fields parallel to and perpendicular to the magnetic field.

While there is a maximum in this fraction of almost 70%, for an electric field parallel to a ~ 0.1 T magnetic field, the spin-flips are much more rare at high magnetic fields. In the $\sim 1 - 2$ T that trapped atoms can explore in ALPHA, many excitations to the 2S state would be required before a spin-flip would on average be induced. Thus, for the current rate of trapping, this is not a viable method for detecting the excitations, although with a significant increase in the number of trapped atoms, it could be.

6.3 Microwave Transition

The low efficiency in inducing spin-flips in simple electric field induced decays of the $2S$ state can be circumvented by resonantly driving the $2S$ population into a single $2P$ state, chosen to have a high probability to decay to an untrapped ground state. The ideal state to populate would have a very high probability of decaying to untrapped states, a non-zero electric dipole moment to $|2S_\alpha\rangle$, so the transition can be easily driven, and a transition frequency which does not overlap with any other transitions that would unintentionally depopulate either the $1S$ or the $2S$ states. Additionally, it would be convenient if the microwave radiation needed to drive the transition could be delivered without significant changes to the apparatus. Currently microwaves are delivered into the ALPHA electrode stack through a waveguide, which supports frequencies from 22 GHz up to approximately 30 GHz, so initially we'll search for a transition frequency in this band.

In Figure 5.2 on page 47, we plotted the energies of all the states in the $N = 2$ manifold. While $|2P_d\rangle$ has a 100% chance of decaying to an untrapped ground state, there is no dipole moment to $|2S_\alpha\rangle$. The chance of spin-flips from $|2P_f\rangle$ is quite high ($\sim 85\%$ at 1T), and there is an electric dipole transition from $|2S_\alpha\rangle$. Unfortunately, the transition to $|2P_a\rangle$ has nearly the same frequency. In fact the two transition frequencies cross at almost exactly $B = 1$ T, with $f(|2S_\alpha\rangle \rightarrow |2P_f\rangle)$ being larger for $B > 1$ T and both frequencies increasing with B . $|2P_a\rangle$ never decays to an untrappable ground state, so driving $|2S_\alpha\rangle \rightarrow |2P_a\rangle$ needs to be avoided. This can be done by lowering the bottom of the magnetic well below the crossing point of 1 T and tuning the microwave radiation to be resonant with the $|2S_\alpha\rangle \rightarrow |2P_f\rangle$ transition at this field. This way, no magnetic field explorable by the trapped atoms brings $|2S_\alpha\rangle \rightarrow |2P_a\rangle$ into resonance.

In Figure 6.1 on the next page we plot the transition rates of these to microwave transitions as functions of magnetic field for two potential driving frequencies. The two peaks overlap at ~ 1 T for a drive frequency of ~ 24 GHz. Notice that for both the plotted microwave frequencies, the $|2P_f\rangle$ peak is sitting on the tail of the $|2P_a\rangle$ peak, meaning some fraction of atoms will be driven to the $|2P_a\rangle$ state, lowering the efficiency of flipping the spins a bit. Even so, in the 22.5 GHz case, spin-flips are induced in up to $\sim 80\%$ of the atoms.

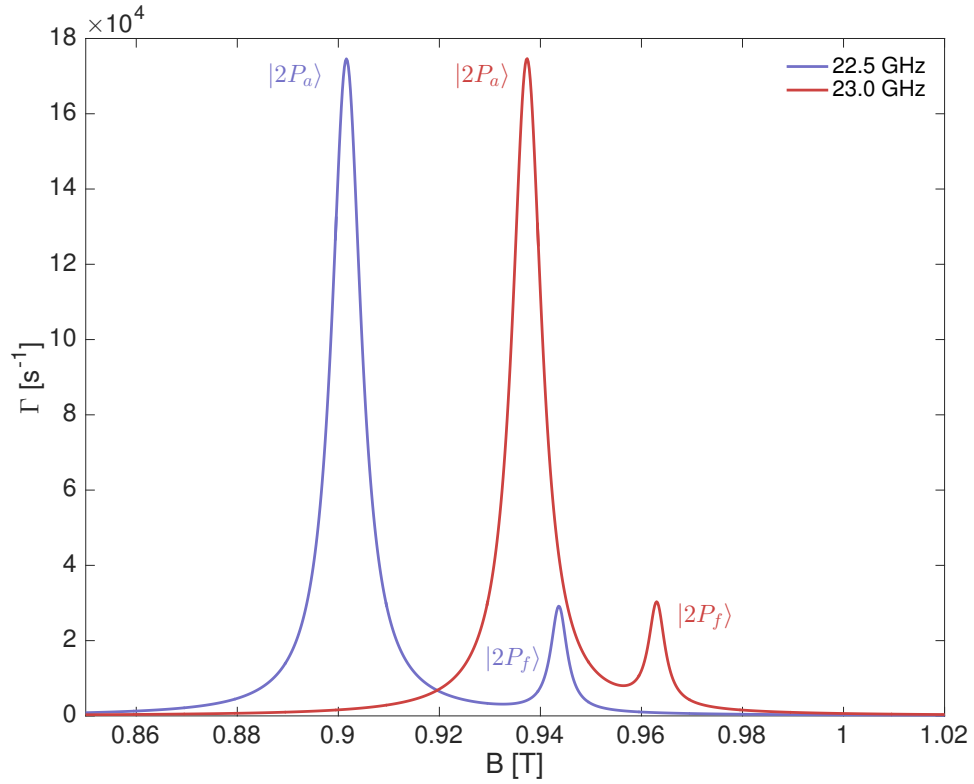


Figure 6.1: Microwave transition rates out of the low field seeking 2S states, calculated for two different frequencies as functions of magnetic field. Assumes 1 mW/cm^2 of microwave intensity. The peaks due to transitions to the $|2P_a\rangle$ and $|2P_f\rangle$ are labeled. The electric dipole moment to $|2P_a\rangle$ is much larger than to $|2P_f\rangle$ and in particular in the 23GHz case, the $|2P_f\rangle$ peak is sitting on the tail of the $|2P_a\rangle$ peak, making it difficult to drive only the one transition.

Pulsed Detection and SNR

Having established that a large fraction of atoms excited to the 2S state can be brought to annihilate to produce signal in the detector, we consider how to optimize the ratio of the expected signal to the background rate of cosmic events in the annihilation detector. By pulsing the microwave radiation and only looking for annihilation events during the pulse, the number of integrated background events can be reduced drastically. Of course, the signal is also reduced, as atoms can potentially decay out of the 2S state before a microwave pulse is turned on to drive them into a 2P state. Clearly, for this to be an efficient detection method, the time between microwave

pulses should not be longer than the mean lifetime of 2S atoms in the trap, which we estimated in Chapter 5 to be reduced from the natural lifetime of 122ms to around 50ms by the motional electric field. The other parameter that could potentially be tuned is the length of the microwave pulse applied. The shorter time needed to drive the microwave transition, the shorter the detection window can be. There is however a lower limit on the length of detection window, set by the trapped atom dynamics: Once the spin of an antihydrogen atom has been flipped, it still has to travel to the wall of the apparatus before it annihilates. A good estimate for how long this can take is the radial bounce time for the still trapped atoms, which is ~ 1 ms. With these restrictions, the SNR stays well below 1 for realistic experimental parameters, even when employing the Multivariate analysis to reduce the background rate.

These considerations also apply directly to detection through (DC) electric field induced decays with spin-flips, as well as for the detection of Lyman- α photons, although with a different background rate for whichever single photon detector is considered.

6.4 Photo-ionisation

Finally we turn our attention to potentially exploiting that a single 243nm photon can ionise the 2S state in (anti)hydrogen. Detecting the thus produced ions has been suggested for a range of two-photon spectroscopy experiments, where one additional photon from the exciting laser beam photo-ionises the excited state [56]. This is an effect that we have until now left out of the discussions of the detection methods above, but which affects them all, since photo-ionisation is a competing mechanism for leaving the 2S state. Especially at the high powers needed to excite the very small numbers of currently trapped antihydrogen atoms, photo-ionisation is quite significant. Figure 5.6 on page 64 shows an efficiency of almost 70% for ionising the trapped atoms in the absence of any intentionally introduced de-excitation mechanisms and using a realistic set of experimental parameters. A significant advantage of using photo-ionisation as the detection method is that the antiprotons produced by photo-ionisation can be stored for much longer than the lifetime of the 2S in the atom, which limits the achievable SNR in all of the above schemes. Since by design the entire volume acces-

sible to trapped atoms in ALPHA is surrounded by Penning trap electrodes, the antiprotons produced by photo-ionising antihydrogen can be easily contained. Furthermore, the energy of the antiprotons created will be similar to that of the trapped atoms, meaning small electric potentials are sufficient to confine them. This means that the perturbing effect on the nearby trapped antihydrogen can be kept negligible.

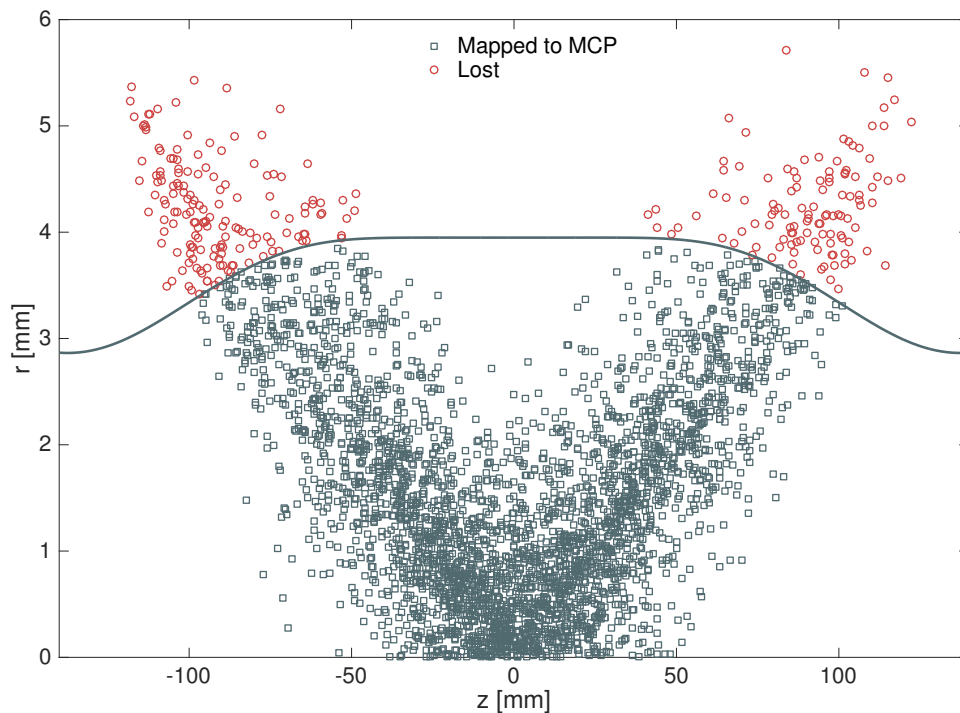


Figure 6.2: Positions in z and r of ionisation from simulations in a flattened magnetic field, indicating the regions of the trap where all field lines go through the MCP. 92% of the ~ 3500 ionisations plotted here occur in this region, enabling the detection of the produced ions by the MCP assembly. The remaining 8% would hit other structures when pushed out of the trap and would likely not produce any signal on the MCP. The recorded positions from these simulations are smeared around the laser beam, leading to a range of ionisation positions which is wider than the laser beam itself. This however does not significantly impact the fraction of ionisations within the gray line.

In order to detect the antiprotons created from photo-ionisation, they can be dumped onto a MicroChannel Plate (MCP). In ALPHA, an MCP and phosphorous plate assembly located on the axis of the Penning trap and about

2m away from the center of the magnetic minimum trap, is already used to measure the radial density profile of plasmas in the Penning-Malmberg trap. Since the plasmas are typically much smaller than the space available for trapped neutral atoms, we investigated whether the geometry of the magnetic fields and our current MCP assembly also allows for an efficient detection of antiprotons produced by photo-ionising antihydrogen atoms. In Figure 6.2 on the previous page, we plot the approximate (z, r) positions that the atoms are ionised at in our simulations. Assuming the antiprotons follow the magnetic field line they are created on, 92% of them are directed onto the MCP when pushed out of the trap.

Bucked Magnetic Field

Another option for detecting the photo-ionised atoms, which we have already briefly mentioned, relies on the antimatter nature of the produced antiprotons. If the antiprotons are brought to annihilate within the silicon vertex detector, they can be detected with the well known efficiency and cosmic background rejection of this detector. In our most traditional magnetic field configurations, the external solenoid ensures that all field lines which are close to the axis extend far beyond the Penning trap electrodes and the annihilation detector, preventing charged particles from moving radially and annihilating on the walls - this is indeed part of the operating principle of a Penning trap. However, by cancelling the field from the external solenoid with an equal and opposite field provided by one of our mirror coils, all field lines are forced into the walls in a small region around the field-cancelling or bucking coil, providing a path for the charged antiprotons to annihilate.

Naturally, using one of the mirror coils for cancelling the field in one region of the trap leaves both a smaller region in which to keep antihydrogen trapped and fewer coils with which to make the bottom of the trap as uniform as possible. The effect of this is seen in Figure 5.8 on page 66, where we plotted results of simulations which are identical apart from the choice of magnetic field. The decrease in excitation rate is clear, but not devastating, and the bucked magnetic field configuration was chosen for the experiments described in Chapter 7.

6.5 Disappearance Detection

All of the methods discussed above result in a depletion to some degree of the number of trapped atoms left in the trap, which upon the shutdown of the trap can itself be used to infer that 1S-2S transitions were driven. This kind of detection through the disappearance of trapped atoms is reminiscent of the analysis presented in Chapter 4, and has already been applied in spectroscopic measurements on antihydrogen [19].

Detecting only how many atoms are left in the trap after an experimental cycle eliminates the issue of needing to look for signal often, leading to a long integrated detection time and significant cosmic event (or other backgrounds for Lyman- α photon detectors) contamination of the data. Furthermore, looking for the depletion of trapped atoms can be done entirely in parallel with any of the above methods, looking for the direct appearance of signal from the 2S state.

The downside lies in having to detect with statistical significance changes in the rate at which antihydrogen is still trapped at the end of an experimental trial. This requires a good null experiment with no depletion of the trapped population, performed in strict alternation with the measurement trials to avoid systematic effects stemming from changes in the rate at which antihydrogen is initially trapped. Additionally, the depletion of trapped atoms must be large, lest the number of trials needed to detect a difference from the null trials be too large. Specifically for our case, it is therefore favorable to drive out both the $|1S_c\rangle$ and the $|1S_d\rangle$ atoms, assumed to be trapped in equal amounts, by driving both the $1S_c - 2S_c$ and the $1S_d - 2S_d$ transitions. This is indeed what was attempted in the experiments described in Chapter 7.

Chapter 7

1S-2S Spectroscopy Runs

As pointed out earlier, a measurement of the 1S-2S transition frequency in antihydrogen has been a primary goal in antihydrogen research since its conception.

This chapter reports on series of experimental trials, attempting to drive the 1S-2S transition, performed over a period of 10 days in November of 2015. These trials were performed with laser enhancement from the external cavity, described in Section 2.4 on page 24. Below we examine the data collected and do not find convincing evidence that this transition was successfully driven, for the clear reason that the average laser power circulating in the cavity was around 650mW - quite far from the 2W we assume in Chapter 5. This deficit in power was caused by UV damage to the vacuum window, resulting in a low transimission of this optic, but it was not identified until the end of the beam time, when optics could be removed from the vacuum chamber and diagnosed.

7.1 Experimental Procedure

The experiment is performed by alternating between "on resonance" trials, where the laser is tuned to be on resonance in the center of the magnetic trap, and "off resonance" trials, where the laser frequency is detuned by -200kHz for each of the respective transitions, which brings it several linewidths from the resonance anywhere in the trap. Note that the off resonance frequency is chosen lower than the resonance, so the tail of the lineshape, shown for example in Figure 5.7 on page 65 is avoided.

After antihydrogen is produced and trapped and any remaining charged particles have been cleared from the trap, the laser shutter is opened, automatically locking the enhancement cavity. The d-d transition is then illuminated for 250s, after which the shutters are closed, laser frequency changed and shutters re-opened to illuminate the c-c transition for 250s. During each of the illumination periods, any ions potentially created are prevented from escaping by small potentials applied to the Penning trap electrodes, and every 1 second, any stored ions are pushed towards the bucked mirror coil by a large and short-lived electric field to make them annihilate. At the end of this, the magnetic trap is ramped down and the number of remaining atoms counted.

Much like in [19], we also perform a version of the experiment identical to the on- and off- resonance trials but for the fact that no laser light is introduced to the trap. The antihydrogen is held for the same total time and we apply the same potentials to the electrodes to expel any ions formed. These "no laser" trials can be helpful to establish a consistent picture of everything that could happen to the antihydrogen atoms. For example, one might imagine spurious laser light could cause additional outgassing from the cryogenic surfaces inside the experiment and thus reduce the lifetime of antihydrogen. Such an effect would show up in a comparison between the off-resonance trials and those entirely without laser light.

These trials were not performed in as strict an alternation procedure as the on- and off- resonance trials, and having limited beam time left in the season, we prioritized more runs that could potentially show evidence of excitations over getting good statistics in trials with no laser. As we discuss below, this may have limited the usefulness of this set of trials.

Electron Cyclotron Resonance Magnetometry

Because of the residual Zeeman effect of the 1S-2S transition, listed in Table 5.2 on page 60, it is necessary to know the magnetic field in the center of the trap to a good precision. While commercially available magnetometers can easily achieve the precision required for at least an initial measurement of the 1S-2S transition, a practical realisation of a device which consistently measures the field in the correct location of the trap, which can be made

without significant change to the experimental setup, i.e. can be run in between trials with antihydrogen, and which respects the geometrical, cryogenic, and vacuum related requirements of the apparatus, is challenging. Instead, we employ a novel method, described in [62], and already used for magnetometry in [19], to measure the cyclotron resonance frequency of an electron plasma, located in the center of the magnetic trap. To within the required precision, the cyclotron frequency of this plasma is identical to the single particle cyclotron frequency:

$$f_c = \frac{qB}{2\pi m} \quad (7.1)$$

, and is thus an good probe of the magnetic field strength.

We drive the cyclotron motion of the electrons using pulsed microwave radiation, and the energy absorbed is redistributed through collisions, resulting in a temperature increase of the plasma. We detect this temperature increase by non-destructively monitoring the quadrupole mode frequency of the plasma [63], which increases nearly linearly with temperature for our parameters. The quadrupole mode frequency measurement is made by exciting the plasma with an RF pulse near this frequency, delivered to one of the electrodes confining the plasma, and then detecting on the electrode most centered on the plasma, the mirror charge induced by the quadrupole motion of the plasma.

The relative precision with which we can determine the central magnetic field in this way is roughly 3.4×10^{-4} , which, in a ~ 1 T field and using the values in table 5.2 on page 60, corresponds to shifts in the 1S-2S transition frequencies of ~ 170 Hz (~ 3.4 kHz) for the d-d (c-c) transition.

During the measurement period, we performed this measurement immediately before each beam period of 8 hours, and the laser frequency was adjusted accordingly. The maximum excursions of these daily measurements were all comfortably within a single linewidth of the atomic transition as produced by our simulations.

Fast Ramp-Down

For these experiments, we employed a different shutdown method for the magnetic minimum trap than in our previous results: In our traditional magnet shutdown, the magnet connection to the power supply is rapidly switched to a resistor network, in which the energy is dumped with the previously

quoted near exponential current decay with a time constant of 9 ms. Here, we instead let the power supply control and linearly ramp down the current as fast as is allowed by the safety system, which protects the magnets from quenches. We call this kind of magnet shutdown a FRD, for Fast Ramp-Down. The time it takes for essentially all of the antihydrogen atoms to have annihilated during a shutdown is increased from ~ 30 ms to ~ 1.5 s by using FRD, which increases the cosmic contamination of the annihilation data by an equal factor. The expected number of cosmic events, misidentified as annihilations in a single shutdown of the trap is then 0.07 rather than 0.0014 for the exponential shutdown. On the other hand, this mode of operation also increases our rate of taking data: A consequence of the very fast exponential shutdown of the magnets is a temperature increase of the Penning trap electrodes and the superconducting coils, mainly due to induced currents in the electrodes and other conductive material experiencing a rapidly changing magnetic field. Before an experiment can be repeated, all of these structures have to be allowed to reach equilibrium temperature again. The timescale of this re-cooling depends on how well any particular structure is thermally connected to the liquid helium reservoir. In ALPHA, the equilibrium temperature is typically re-established after ~ 8 minutes. By slowing down the shutdown of the magnetic trap, we have been able to eliminate the need to wait between experimental cycles for this re-cooling to happen, meaning more data taken per hour of beam time.

7.2 Data and Analysis

Reminiscent of [19], we look for evidence of 1S-2S transitions in two complementary analysis modes. In "Disappearance" mode we look for the lack of survival until the shutdown of the magnetic trap of the antihydrogen atoms when the laser is on resonance compared to off resonance. In "Appearance" mode, we look for the direct signal of photo-ionised antihydrogen atoms being made to annihilate on the wall of trap. In each case we can compare the data to simulations which carefully mimic the experimental trials. The lineshape in Figure 7.1 on the next page is the result of such simulation, where the detunings of 0 kHz and -200 kHz model the on-resonance and off-resonance trials, respectively.

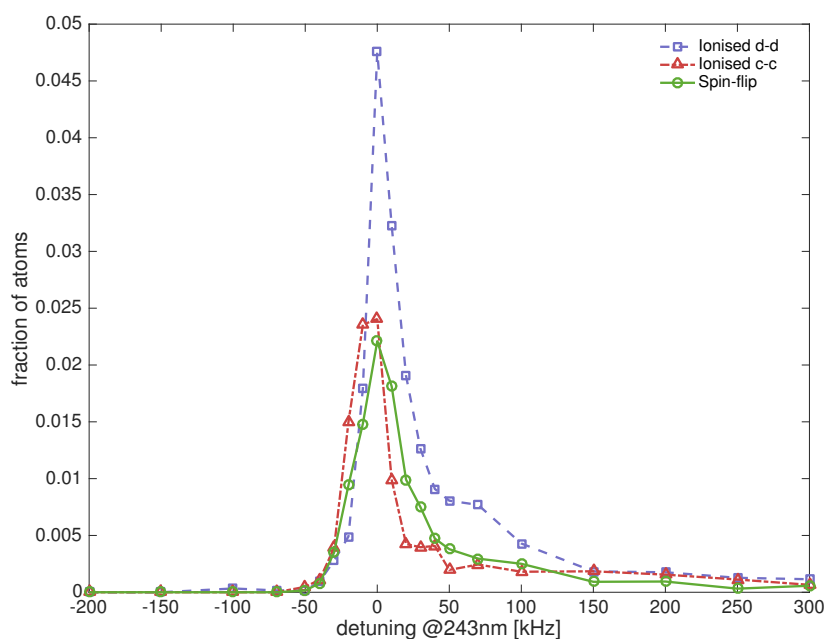


Figure 7.1: Simulated lineshapes in different detection channels for the parameters used in spectroscopy runs of 2015. The relatively small homogeneous region of the magnetic minimum in this configuration causes a significant difference between the responses in the c-c transition and the d-d transition. There is still some numerical noise present, although more than 10^4 atoms were simulated for each detuning. It is computationally slow to reduce this noise when the effect investigated is small.

Disappearance mode

In Table 7.1 on the following page we report the number of annihilation events recorded at the end of the performed trials. The survival rate in the on-resonance and off-resonance trials are equal within the counting statistics errors. Thus, a null-hypothesis that the two rates are equal cannot be rejected. Similarly, the hypothesis predicted by our simulations that the survival rate in on-resonance trials is reduced by 7% compared to the off-resonance trials can also not be excluded by this data.

The background rate of cosmic events misidentified as annihilations was measured immediately after the data taking period in the same bucked magnetic field as was used in the spectroscopy trials, and was found to be 48 ± 1.5 mHz. Accepting events in a 1.5s window at the end of each trial then leads to the expected background reported in the table.

Table 7.1: Expected and observed counts in the disappearance mode of detection. The simulations give a total reduction in survival rate in the on-resonance case of $\sim 7\%$.

	Trials	Det. time [s]	Exp. Backg.	Obs.	Rate
On-resonance	42	63	3	27	0.64 ± 0.12
Off-resonance	39	58.5	2.8	24	0.62 ± 0.13
No laser	12	18	0.9	4	0.33 ± 0.17

The difference in the number of on-resonance trials performed vs off-resonance stems from incomplete pairs of trials at the end of 8h beam periods. If every beam period is started with an on-resonance trial but randomly ends with either on- or off- resonance, the total number of trials can differ while the alternation is still kept strict within beam periods.

The trials with no laser light introduced to the trap not only suffer from low statistics, but also seem to fail to capture the antihydrogen trapping rate in the trials where laser light was introduced. In the absence of systematic effects from changing experimental conditions, antihydrogen should be at least as likely to survive the full experimental cycle with no laser light present as it is in off-resonance trials. This underlines the importance of the alternation of trials between which a comparison of the rate of events is wanted. Even though the trials with no laser light are performed on the same days as the alternating on-resonance and off-resonance trials, changes in experimental conditions can introduce systematic effects to which we have to attribute the apparent lack of events in the trials with no laser light.

Appearance mode

Looking at events in the annihilation detector in narrow time windows around when the ions produced are ejected from the trap, results in the data given in Table 7.2 on the next page. To arrive at the observed counts, we sum the number of annihilation-like events in each of the 250 such ion ejections per transition per trial.

The calculated expected signal is derived from the simulation of these trials, and uses the thusly found fraction of photo-ionised atoms. We then expect to see a number of counts from a given transition equal to the number of atoms of the relevant hyperfine state in the trap, $r/2$, times the fraction, ϵ_{Ion} that end up ionised, times the number of trials, N_t , times the efficiency of

Table 7.2: Expected and observed counts for appearance mode detection. The observation window covers 9ms around each of the stored ion ejections, of which there are 250 per transition per trial.

	Illum. time [s]	Det. time [s]	Exp. sig.	Exp. backg.	Observed
d-d ON	10500	94.5	0.7	4.5	3
c-c ON	10500	94.5	0.4	4.5	4
d-d OFF	9750	87.75	0	4.2	1
c-c OFF	9750	87.75	0	4.2	4
No laser	-	54	0	2.6	5

making an ion annihilate within the time window we are looking in, ϵ_{Dump} , times the detector efficiency, ϵ_{det} :

$$\begin{aligned}
 S &= \frac{r}{2} \times \epsilon_{lon} \times N_t \times \epsilon_{Dump} \times \epsilon_{det} \\
 &= \frac{r_{det}}{2} \times \epsilon_{lon} \times N_t \times \epsilon_{Dump}
 \end{aligned} \tag{7.2}$$

, where $r_{det} = r \times \epsilon_{det}$ is the detected rate at which antihydrogen is trapped. For this analysis we assume $\epsilon_{Dump} = 1$.

The expected background for this total integration time of the detector is significantly bigger than the expected signal at this laser power, and the observed number of counts are consistent with both background alone and with background plus expected signal. In counting these events, we include reconstructed annihilation vertices from anywhere in the trap. A good way of reducing the background contamination in this sample would be to only consider vertices close to the bucked mirror coil, where we expect the ejected ions to annihilate. If such a cut is introduced on this data, the expected number of background events can be reduced to just below 1, while the observed counts go to 0.

7.3 Conclusion

In summary, the recorded data does not allow the conclusion that 1S-2S transitions were driven in the trapped antihydrogen atoms in these trials. Considering the simulation of the experiment with the average laser power that we now know was in the cavity, presented in Figure 7.1 on page 79 it would indeed be quite difficult to make a definitive detection with these pa-

rameters.

The data is however consistent with our simulation of the experiment across all of our measurements, and with a laser intensity closer to the design value, there is a good chance for a first detection of 1S-2S transitions in the near future. At the time of writing, the ALPHA experiment is heading into another beam season after an intervention which, besides replacing the damaged laser windows with ones much more resistant to UV damage, has restored the internal cavity to full functionality and furthermore made any potential interventions to service the internal cavity mirrors much simpler, ensuring the efficient use of the beam time provided by CERN. With these modifications in place, we are looking forward to taking more data.

Chapter 8

Conclusions and Outlook

The field of antihydrogen research is not an old one, but it is rapidly progressing and expanding, with several new experiments getting approved and starting data taking in the last few years. The construction of ELENA [64] is well under way and promises a drastic increase in the availability of antiprotons for experiments.

Since antihydrogen was first trapped in 2010, a number of new measurements have been made, including both the first resonantly driven quantum transitions [19] and the first precision measurement of a property of the antihydrogen atom [50].

In this work we have reported on a new technique for measuring the gravitational free-fall of antihydrogen and its application to the recorded annihilation data from trapped antihydrogen in the original ALPHA machine. We have presented an improved limit on the charge neutrality of antihydrogen, derived from measurements in ALPHA-2, and reaching a sensitivity that allows for a new limit on the positron charge anomaly to be set.

The equations relevant to the 1S-2S excitation and detection under the experimental conditions in ALPHA were derived and on the basis of simulations incorporating these, various schemes for detecting the excited 2S atoms were discussed. Under the current experimental conditions in ALPHA, one of these schemes was found to be feasible, namely the storage and subsequent detection of the antiprotons resulting from the photo-ionisation of the 2S state. A set of unprecedented experimental trials to excite the 1S-2S transition in antihydrogen were performed.

At the time of writing this thesis, work is ongoing in the ALPHA-2 machine to get everything ready for detecting a 1S-2S spectroscopic signal. This will already with the initial detection enable a comparison with hydrogen of the first ~ 10 digits of the transition frequency. The next big leap in precision from then on will be tracing out the lineshape, allowing for at least an order of magnitude improvement in the determination of the line center. This will of course also require a larger data sample, which can be achieved either through substantially more experimental cycles, or, preferably, by increasing the signal obtained per cycle.

To date, only about 1 000 antihydrogen atoms have ever been trapped and detected - a remarkably small number considering the measurements that have been made. With the increasing number of experiments at the AD, and the addition of the ELENA ring, chances are good that antihydrogen will continue to be a fast moving and exciting field of research.

Appendix A

Table of Acronyms

AOM	Acousto-Optic Modulator
BS	Beam Splitter
DL	Diode Laser
EOM	Electro-Optic Modulator
FHG	Fourth Harmonic Generation
FRD	Fast Ramp-Down
FSR	Free Spectral Range
MCP	MicroChannel Plate
MVA	MultiVariate Analysis
OVC	Outer Vaccum Chamber
PDH	Pound-Drever-Hall
ppb	part(s) per billion
ROC	Radius Of Curvature
SHG	Second Harmonic Generation
SNR	Signal to Noise Ratio
SVD	Silicon Vertex Detector
UHV	Ultra-High Vacuum
ULE	Ultra-Low Expansion
QED	Quantum ElectroDynamics

Bibliography

- [1] P. A. M. Dirac. Quantised singularities in the electromagnetic field. *Proceedings of the Royal Society of London A: Mathematical, Physical and Engineering Sciences*, 133(821):60–72, 1931.
- [2] C. D. Anderson. The positive electron. *Phys. Rev.*, 43:491–494, Mar 1933.
- [3] C. S. Wu, E. Ambler, R. W. Hayward, D. D. Hoppes, and R. P. Hudson. Experimental test of parity conservation in beta decay. *Phys. Rev.*, 105:1413–1415, Feb 1957.
- [4] J. H. Christenson, J. W. Cronin, V. L. Fitch, and R. Turlay. Evidence for the 2π decay of the k_2^0 meson. *Phys. Rev. Lett.*, 13:138–140, Jul 1964.
- [5] Y. Chao. Direct CP violation in charmless B decays. *eConf*, C060409:040, 2006.
- [6] G. Lüders. Proof of the TCP theorem. *Annals of Physics*, 2(1):1 – 15, 1957.
- [7] G. Y. Drobychev, et al. Proposal for the AEGIS experiment at the CERN antiproton decelerator (Antimatter Experiment: Gravity, Interferometry, Spectroscopy). Technical Report SPSC-P-334. CERN-SPSC-2007-017, CERN, Geneva, Jun 2007.
- [8] G. Chardin, et al. Proposal to measure the Gravitational Behaviour of Antihydrogen at Rest. Technical Report CERN-SPSC-2011-029. SPSC-P-342, CERN, Geneva, Sep 2011.
- [9] C. G. Parthey, et al. Improved measurement of the hydrogen 1S-2S transition frequency. *Phys. Rev. Lett.*, 107:203001, Nov 2011.
- [10] V. A. Kostelecky and A. J. Vargas. Lorentz and CPT tests with hydrogen, antihydrogen, and related systems. *Phys. Rev.*, D92(5):056002, 2015.

- [11] T. W. Hänsch and C. Zimmermann. Laser spectroscopy of hydrogen and antihydrogen. *Hyperfine Interactions*, 76(1):47–57, 1993.
- [12] G. Baur, et al. Production of antihydrogen. *Physics Letters B*, 368(3):251 – 258, 1996.
- [13] G. Gabrielse, et al. First capture of antiprotons in a penning trap: A kiloelectronvolt source. *Phys. Rev. Lett.*, 57:2504–2507, Nov 1986.
- [14] S. Maury. The Antiproton Decelerator: AD. *Hyperfine Interactions*, 109:43–52, August 1997.
- [15] M. Amoretti, et al. Production and detection of cold antihydrogen atoms. *Nature*, 419(6906):456–459, 10 2002.
- [16] G. Gabrielse, et al. Background-free observation of cold antihydrogen with field-ionization analysis of its states. *Phys. Rev. Lett.*, 89:213401, Oct 2002.
- [17] G. B. Andresen, et al. Trapped antihydrogen. *Nature*, 468(7324):673–676, 2010.
- [18] G. Gabrielse, et al. Trapped antihydrogen in its ground state. *Phys. Rev. Lett.*, 108:113002, Mar 2012.
- [19] C. Amole, et al. Resonant quantum transitions in trapped antihydrogen atoms. *Nature*, 483(7390):439–443, 2012.
- [20] N. Kuroda, et al. A source of antihydrogen for in-flight hyperfine spectroscopy. *Nat Commun*, 5, 01 2014.
- [21] L. Essen, R. W. Donaldson, M. J. Bangham, and E. G. Hope. Frequency of the hydrogen maser. *Nature*, 229(5280):110–111, 01 1971.
- [22] P. Crivelli, D. Cooke, and M. W. Heiss. The anti-proton charge radius. 2016.
- [23] M. Hori and others. Two-photon laser spectroscopy of antiprotonic helium and the antiproton-to-electron mass ratio. *Nature*, 475:484–488, 2011.
- [24] S. Ulmer, et al. High-precision comparison of the antiproton-to-proton charge-to-mass ratio. *Nature*, 524(7564):196–199, 08 2015.

- [25] M. Hori and J. Walz. Physics at CERN's Antiproton Decelerator. *Prog. Part. Nucl. Phys.*, 72:206–253, 2013.
- [26] C. Amole, et al. The alpha antihydrogen trapping apparatus. *Nuclear Instruments and Methods in Physics Research Section A: Accelerators, Spectrometers, Detectors and Associated Equipment*, 735:319 – 340, 2014.
- [27] W. Bertsche, et al. A magnetic trap for antihydrogen confinement. *Nuclear Instruments and Methods in Physics Research Section A: Accelerators, Spectrometers, Detectors and Associated Equipment*, 566(2):746 – 756, 2006.
- [28] G.B. Andresen, et al. Antihydrogen annihilation reconstruction with the ALPHA silicon detector. *Nuclear Instruments and Methods in Physics Research Section A: Accelerators, Spectrometers, Detectors and Associated Equipment*, 684(0):73 – 81, 2012.
- [29] W A Bertsche, E Butler, M Charlton, and N Madsen. Physics with antihydrogen. *Journal of Physics B: Atomic, Molecular and Optical Physics*, 48(23):232001, 2015.
- [30] G. B. Andresen, et al. Confinement of antihydrogen for 1,000 seconds. *Nat Phys*, 7:558–564, 2011. 10.1038/nphys2025.
- [31] G. B. Andresen, et al. Search for trapped antihydrogen. *Physics Letters B*, 695:95–104, January 2011.
- [32] G. B. Andresen, et al. Autoresonant excitation of antiproton plasmas. *Phys. Rev. Lett.*, 106:025002, Jan 2011.
- [33] C. Amole, et al. Description and first application of a new technique to measure the gravitational mass of antihydrogen. *Nat Commun*, 4:1785, Apr 2013. Article.
- [34] C. Amole, et al. Discriminating between antihydrogen and mirror-trapped antiprotons in a minimum-b trap. *New Journal of Physics*, 14(1):015010, 2012.
- [35] T. Udem, R. Holzwarth, and T. W. Hänsch. Optical frequency metrology. *nature*, 416:233–237, March 2002.

- [36] Ye, J. and Cundiff, S. T. *Femtosecond Optical Frequency Comb Technology*. Springer, 1 edition, 2005.
- [37] D. W. Allan, N. Ashby, and C. C. Hodge. The science of timekeeping. Technical report, Hewlett Packard, 1997. Application note 1289.
- [38] D. Vukobratovich, K. A. Fetterhoff, J. R. Myers, P. D. Wheelwright, and G. R. Cunnington. Bonded mounts for small cryogenic optics, 2000.
- [39] M. Fischler, J. Lykken, and T. Roberts. Direct observation limits on anti-matter gravitation. 2008.
- [40] E. G. Adelberger, B. R. Heckel, C. W. Stubbs, and Y. Su. Does antimatter fall with the same acceleration as ordinary matter? *Phys. Rev. Lett.*, 66:850–853, Feb 1991.
- [41] A. Apostolakis et al. Tests of the equivalence principle with neutral kaons. *Phys. Lett.*, B452:425–433, 1999.
- [42] R. J. Hughes and M. H. Holzschneider. Constraints on the gravitational properties of antiprotons and positrons from cyclotron-frequency measurements. *Phys. Rev. Lett.*, 66:854–857, Feb 1991.
- [43] J. M. LoSecco. The case for neutrinos from sn 1987a. *Phys. Rev. D*, 39:1013–1019, Feb 1989.
- [44] M. M. Nieto, J. T. Goldman, J. D. Anderson, E. L. Lau, and J. Perez-Mercader. Theoretical motivation for gravitation experiments on ultralow-energy anti-protons and anti-hydrogen. In *Low-energy anti-proton physics. Proceedings, 3rd Biennial Conference, Bled, Slovenia, September 12-17, 1994*, 1994.
- [45] M. M. Nieto and T. Goldman. The arguments against “antigravity” and the gravitational acceleration of antimatter. *Physics Reports*, 205(5):221–281, 1991.
- [46] P. H. Donnan, M. C. Fujiwara, and F. Robicheaux. A proposal for laser cooling antihydrogen atoms. *J. Phys.*, B46:025302, 2013.
- [47] G. Bressi, et al. Testing the neutrality of matter by acoustic means in a spherical resonator. *Phys. Rev. A*, 83:052101, May 2011.

- [48] K. A. Olive et al. Review of Particle Physics. *Chin. Phys.*, C38:090001, 2014.
- [49] P. T. Greenland. Antimatter. *Contemporary Physics*, 38(3):181–203, 1997.
- [50] C. Amole, et al. An experimental limit on the charge of antihydrogen. *Nat Commun*, 5, 06 2014.
- [51] M. Ahmadi, et al. An improved limit on the charge of antihydrogen from stochastic acceleration. *Nature*, 529(7586):373–376, 01 2016.
- [52] M. Baquero-Ruiz, et al. Using stochastic acceleration to place experimental limits on the charge of antihydrogen. *New Journal of Physics*, 16(8):083013, 2014.
- [53] H. A. Bethe and E. E. Salpeter. *Quantum Mechanics of One- and Two-Electron Atoms*. Springer, 1 edition, 1957.
- [54] C. L. Cesar, et al. Two-photon spectroscopy of trapped atomic hydrogen. *Phys. Rev. Lett.*, 77:255–258, Jul 1996.
- [55] J. T. M. Walraven and I. F. Silvera. Helium temperature beam source of atomic hydrogen. *Review of Scientific Instruments*, 53(8):1167–1181, 1982.
- [56] M. Haas, et al. Two-photon excitation dynamics in bound two-body coulomb systems including ac stark shift and ionization. *Phys. Rev. A*, 73:052501, May 2006.
- [57] E. Forest and R. D. Ruth. Fourth-order symplectic integration. *Phys. D*, 43(1):105–117, April 1990.
- [58] H Yoshida. Construction of higher order symplectic integrators. *Physics Letters A*, 150(5):262 – 268, 1990.
- [59] J Candy and W Rozmus. A symplectic integration algorithm for separable hamiltonian functions. *Journal of Computational Physics*, 92(1):230 – 256, 1991.

- [60] P. H. Donnan, K. Niffenegger, T. Topcu, and F. Robicheaux. Calculation of state selective field ionization of hydrogen atoms in a strong magnetic field. *Journal of Physics B: Atomic, Molecular and Optical Physics*, 44(18):184003, 2011.
- [61] C. L. Cesar. Trapping and spectroscopy of hydrogen. *Hyperfine Interactions*, 109(1):293–304, 1997.
- [62] C. Amole, et al. In situ electromagnetic field diagnostics with an electron plasma in a penning-malmberg trap. *New Journal of Physics*, 16(1):013037, 2014.
- [63] D. H. E. Dubin. Theory of electrostatic fluid modes in a cold spheroidal non-neutral plasma. *Phys. Rev. Lett.*, 66:2076–2079, Apr 1991.
- [64] S. Maury, et al. ELENA: the extra low energy anti-proton facility at CERN. *Hyperfine Interactions*, 229(1):105–115, 2014.